UNIVERSITÀ DEGLI STUDI DI PALERMO
Dottorato in ingegneria dell'innovazione tecnologica.
Dipartimento dell'innovazione industriale e digitale-DIID
Ingegneria Chimica, Gestionale, Informatica, Meccanica

Ionizing radiation synthesis of multifunctional nanogels for biomedical applications

IL DOTTORE
LORENA ANNA DITTA

IL COORDINATORE
Prof. ANTONIO CHELLA

IL TUTOR
Prof. CLELIA DISPENZA

CICLO XXX
2018

ABSTRACT

Nanogels (NGs) are nanosized three-dimensional networks of crosslinked hydrophilic polymers. Their tunable chemical structure, physico-chemical properties and potential biocompatibility make them interesting substrates for the synthesis of "nanodevices" with therapeutic and/or diagnostic functions. In this PhD project, NGs were synthesized through pulsed e-beam irradiation of Poly-N-(Vinyl-Pyrrolidone) (PVP) aqueous solutions. The manufacturing process is fast and straightforward; it does not require the employment of organic solvents, surfactants, initiators or catalyst and guarantees high yields of the desired product.

In dilute aqueous polymer solutions, ionizing radiation is mainly absorbed by water that undergoes radiolysis. The radiolytically produced hydroxyl radicals ($^{\bullet}OH$) react with the polymer forming macroradicals, that will further evolve through different competing reactions (combination, disproportionation, chain scission, etc.). Despite of the apparent simplicity of the manufacturing process, the mechanism of nanogel formation is quite complex and not yet fully understood, due to the large variety of system and process parameters and the intermittent nature of initiation reactions. Various particle size and structures can be obtained by changing the irradiation conditions. The most common synthetic approaches and the main outcomes from mechanistic studies are briefly reviewed in Chapter 1.

Chapter 2 concerns an experimental study, carried out on dilute PVP aqueous solutions irradiated by pulsed electron beams from an industrial-type irradiator, of the polymer molecular structure modification with the aim of elucidating some of the aspects of the reaction mechanism at the basis of nanogels formation and functionalization. The irradiated polymers were characterized in terms of molecular weight (by gel filtration chromatography), hydrodynamic size (by dynamic light scattering) and chemical structure (by FTIR analysis and colorimetric titrations). Furthermore, the production of H_2O_2, that can be considered an indicator of the $^{\bullet}OH$ scavenging efficiency of the polymeric solute, was quantitatively measured (by the

Ghormley triiodide method). These results were discussed also in the light of numerical simulations of radiation chemistry of water, taking into account the actual irradiation conditions (dose per pulse, frequency, pulse length and total dose) as in the experiments, and also in the presence of various amounts of a molecular hydroxyl radical scavenger. It is interesting to note that substantial amounts of molecular oxygen is produced in N_2O-saturated systems. Finally, the application of the Ghormley triiodide method allowed for the quantification of the double bonds formed in the polymer upon irradiation. The double bond concentration build up with dose provides some hints about the type of follow-up reactions of the formed macroradicals, occurring in the various phases of the process.

In Chapter 3, nanogels made of crosslinked PVP with a small amount of grafted acrylic acid (PVP-co-AA), produced with one of the two irradiation set-ups illustrated in Chapter 2, are described. These nanogels were synthetized to be used as substrate for the development of biomedical nanodevices to target two different pathologies: Alzheimer's disease (AD) and ColoRectal cancer (CRC). The PVP-co-AA NGs were characterized in terms of hydrodynamic size, net surface charge, hydrodynamic volume distribution and chemical functionalities, that are useful for the covalent attachment of (bio)molecules of interest. PVP-co-AA NGs were evaluated in terms of *in vitro* and *in vivo* biocompatibility, biodistribution and clearance in mice model. The engineered nanogel system shows encouraging physico-chemical properties and biological response. In fact, NGs show suitable hydrodynamic size, negative surface charge density, biocompatibility (absence of toxicity, proliferative, immunogenic, and thrombogenic responses) and clearance from the bloodstream and urines.

In Chapter 4, the synthesis and characterization of an insulin-nanogel conjugate as potential neuroprotective nanodevice in the treatment of AD is presented. Conjugation protocols were developed in order to obtain the desired conjugation degrees and controlled physico-chemical properties. The insulin-nanogel conjugate was also subjected to colloidal stability tests (upon storage, after freeze-drying) and

various biological evaluations (*in vitro* and *in vivo* insulin biological activity, *in vivo* biodistribution upon intraperitoneal and intranasal administration) that support the potential of this nanodevice for AD treatment.

Concerning the development of nanodevices for the treatment and/or diagnosis of colorectal cancer, PVP-co-AA NGs were evaluated as carriers of the inhibitor of miR-31, a small RNA molecule with an important role in colorectal cancer (CRC) progression, and with Bombesin-DOTA. The latter is a difunctional ligand comprising an active targeting agent (Bombesin) and a chelating agent (DOTA) that – in combination with proper radioisotopes – could be used for either diagnosis or internal radiotherapy. This work is reported in Chapters 5 and 6. Conjugation protocols were developed in order to obtain the desired conjugation degrees and controlled physico-chemical properties. The nanogel-conjugated systems were also subjected to colloidal stability tests (upon storage, after freeze-drying and at high temperature) and to biological evaluations, that encourage to proceed with further evaluation of these nanogel-conjugated systems for the diagnosis and/or treatment of CRC.

The studies carried out during this PhD project offer new insights on the mechanism of formation and functionalization of radiation-engineered PVP NGs and show how versatile these nanomaterials are. Only by varying the type of "decoration", the same substrate can be transformed into different nanodevices that can potentially address the specific diagnostic/therapeutic challenges of a pathologic condition. These promising results encourage (1) to continue to investigate the NGs formation and functionalization mechanisms, by combining experimental and simulation approaches, with the aim of understanding how a specific set of physico-chemical properties and structural modifications can be attained by a selection of a proper set of irradiation conditions and, (2) to proceed further with the biological evaluation of the already developed NG conjugates on relevant *in vivo* disease models in order to evaluate their efficacy in the prospect of requesting approval for clinical trials.

Acknowledgments

These last three years have been very rich in events and experiences that have contributed to my professional and personal growth. My acknowledgements go to several people.

First and foremost, I want to express my gratitude to my supervisor Prof. Clelia Dispenza. I am grateful for her support, advice, encouragements and for having been an inspiration throughout these years. She has provided an excellent example of a successful woman, and passionate researcher and professor.

I am thankful to Dr. Maria Antonietta Sabatino, Dipartimento dell'Innovazione Industriale e Digitale, Università degli Studi di Palermo, for her precious technical advice, her stimulating discussions and support. She played an important role in my research project and I learnt a lot from her.

I also would like to thank Prof. Giuseppe Spadaro, Dipartimento dell'Innovazione Industriale e Digitale, Università degli Studi di Palermo, for thoughtful suggestions and encouragements.

I would like to express my gratitude to Prof. Mats Jonsson of the School of Chemical Science and Engineering, Applied Physical Chemistry Royal Institute of Technology (KTH) (Stockholm, Sweden), for accepting me in his research group and for the access to the e-beam facility. I am also thankful for his support to my research project with the numerical simulations and with very useful suggestions.

I also acknowledge Dr. Grazyna Przybytniak for the access to the e-beam facility at the Institute of Nuclear Chemistry and Technology of Warsaw, Poland and also for her kindness.

I extend my gratitude to Dr. Daniela Giacomazza, Dr. Donatella Bulone, Dr. Pier Luigi San Biagio (Istituto di Biofisica- National Research Council – Palermo), Dr. Marta Di Carlo, Dr. Pasquale Picone (Istituto di Biomedicina e Immunologia Molecolare - National Research Council – Palermo), Prof. Riccardo Alessandro (Dipartimento di Biopatologia e Biotecnologie Mediche, Sezione di Biologia e

Genetica, Università degli Studi di Palermo – Palermo) and his research group for their valuable collaborations on my research project.
I also want to acknowledge Prof. Piotr Ulanski of the Istitute of Applied Radiation Chemistry, Lodz University of Technology, Lodz, Poland and Dr. Samy Remita, Université Paris-Sud Orsay Cedex, Paris, France for helping me to improve the quality my Thesis with their suggestions and recommendations.

I want to thank all my colleagues and friends at Università degli Studi di Palermo and at Royal Institute of Technology (KTH): Maria, Simona, Alessia, Sonia, Fabrizio V., Maurizio, Fabrizio G. and Annika for their friendship, humour and support. We have shared a lot of funny (and tough) moments.

I deeply acknowledge my beloved family for their support and patience.

Finally, I want to dedicate my Thesis to my grandmother. She has been and she will always be my mentor.

List of Papers

Some of the results of this Thesis are included in the following papers:

I. P. Picone*, L.A. Ditta*, M.A. Sabatino, V. Militello, P.L. San Biagio, M.L. Di Giacinto, L. Cristaldi, D. Nuzzo, C. Dispenza, D. Giacomazza, M. Di Carlo, Ionizing radiation-engineered nanogels as insulin nanocarriers for the development of a new strategy for the treatment of Alzheimer's disease. Biomaterials 80, (2016) 179–194.

II. C. Dispenza, M.A. Sabatino, A. Ajovalasit, L.A. Ditta, M. Ragusa, M. Purrello, V. Costa, A. Conigliaro, A., R. Alessandro, Nanogel-antimiR-31 conjugates affect colon cancer cells behaviour. RSC Adv. 7(82), (2017), 52039-52047.

III. P. Picone, M.A. Sabatino, L.A. Ditta, A. Amato, P.L. San Biagio, F. Mulè, D. Giacomazza, C. Dispenza, M. Di Carlo, M., Nose-to-brain delivery of insulin enhanced by a nanogel carrier. J Control Release 270, (2018), 23-36.

*The two Authors contributed equally to this work

My contributions to the papers:

Paper I and III: (i) Contributes to the design of the conjugation protocols. (ii) Conjugation reactions and part of the physico-chemical characterizations of conjugated systems. (iii) Contributes to manuscript's write up.

Paper II: Contributes to synthesis and characterization of "bare" and conjugated NGs.

Table of Contents

I. Background

This PhD project concerns the development of nanosized materials as carriers of therapeutic and/or diagnostic active molecules. This research field is driven by the need to improve the current diagnostic and treatment strategies of many diseases. Nanomaterial-based devices are expected to accomplish one or several of the following roles: (i) *protect* the (bio)active component from premature degradation or elimination; (ii) *recognize* the pathological site and concentrate the payload to the target site; (iii) *modulate* the time of action of the payload; and (iv) carry out a *tracking* function of the administered nanodevice in the organism. They are also expected to be fully biocompatible, degradable and/or eliminated once completed their action. For that, the nanomaterial must fulfil very stringent physico-chemical and biological requirements.

It is a big challenge for a nanomaterial to become attractive for its therapeutic/diagnostic value in the clinic. In fact, for a successful development of the nanomaterial-based device several criterions must be fulfilled: (i) a robust and an easy to scale-up synthetic process; (ii) well-understood reaction mechanisms in order to have a full control on the product features; (iii) successful *in vitro* and *in vivo* biological response.

Nanogels, nanoscalar networks of hydrophilic polymers, thanks to their tuneable physico-chemical properties, colloidal stability in aqueous media, large and flexible surface for multivalent (bio)-conjugation and internal dynamic 3D aqueous environment for incorporation and protection of (bio)molecular drugs, are a very promising nanomaterial-based delivery device platform.

Ionizing radiation of aqueous polymer solutions with high energy pulsed electron beams offers the possibility to produce nanogels as aqueous dispersions, without the employment of initiators, surfactants, organic solvents and catalysts. Water is not only a medium but, upon irradiation, generates also the reactive species responsible for the formation of radical sites along the polymer chains that combine forming crosslinks. As it will be shown in the first Chapter of this Thesis, some important

aspects of nanogel formation have been already elucidated and some key process parameters have been identified. In fact, it has been highlighted that polymer concentration and dose per pulse are two important parameters for controlling particle size, while the absorbed dose plays a key role in nanogel functionalisation.
Even though radiation engineered nanogels have been successful synthesized by several research groups, only a few of them have been tested in biological systems and often only *in vitro* cell cultures.

II. Problem formulation

Nanogels can be synthetized by irradiating dilute (or semi-dilute) aqueous solutions of a "crosslinking-type" polymer with pulsed electron beams. In order to have complete control of their chemical structure, physico-chemical and aging properties and fully exploit their potential in the biomedical field as delivery nanodevices, a clear understanding of the reaction mechanisms is essential. Predictive models that can assist in the definition of system composition and irradiation conditions for the production of nanogels with given size and functionality are not available.
The design of a biomedical nanocarrier is essentially made taking into account (i) the pathology; (ii) the hypothetical therapeutic agent; and (iii) the administration route (intravenous, nasal, etc). Then, it must be subjected to proper biological evaluations. It is also useful to understand if the same nanomaterial may be adapted to serve the therapeutic and/or diagnostic needs of different pathologies. In fact, the versatility of the nanomaterial, together with the ease of its manufacturing and precise control of its features, increase the chances of its industrial development.

III. Strategy

In this PhD project, the possibility to employ a radiation-engineered nanogel (NGs) as material platform for the synthesis of therapeutic and diagnostic nanodevices was investigated. In particular, NGs were synthesized through pulsed e-beam irradiation of Poly-N-(Vinyl-Pyrrolidone) (PVP) aqueous solutions.

The main goals/objectives of this PhD project were two:

1. Nanogels and other key byproducts analysis for the elucidation of some aspects related to the *mechanism* of formation and the route to their simultaneous functionalization.
2. Synthesis, characterization and modification of selected NGs for their "transformation" into nanodevices for specific biomedical applications.

Concerning the first goal, the influence of irradiation conditions and system composition (polymer concentration, gaseous atmosphere) on the chemical structure and physico-chemical properties of the synthesized nanogels, as well as on the concentration of hydrogen peroxide formed were studied. Furthermore, thanks to the collaboration with colleagues from KTH (Sweden), numerical simulations of the water radiation chemistry, under the specific irradiation and systems conditions used in this work, were performed. The concentration of H_2O_2 estimated by the simulation was compared to the values that were experimentally measured for irradiated water or polymer solutions. Other important products of water radiolysis for their impact on the reactions involving the polymer were identified.

Concerning the second goal, the development of biomedical nanodevices starting from the same platform (carboxyl-functionalized PVP NG), was pursued by modifying the nanogels with several kind of biomolecules relevant for the treatment of Alzheimer's disease (AD) and colorectal cancer (CRC).

Whit this purpose in mind, the conjugation protocols were developed, in order to obtain the desired conjugation degree, physico-chemical properties and colloidal stability under the conditions that are relevant for their storage, further processing (e.g. radiolabelling) and administration (e.g. in isotonic PBS buffer or in serum). In particular, the following systems have been synthesized:

- Nanogels modified with fluorescent probes (TRITC, Atto633) for *in vitro* and *in vivo* tracking purposes;
- Nanogels conjugated to insulin for the potential treatment of AD;
- Nanogels conjugated to AntimiR-31 for the potential treatment of CRC;

- Nanogels conjugated with bombesin-DOTA for the potential diagnosis or the treatment of CRC.

"Bare" and selected modified-NG variants were also subjected to *in vitro* and *in vivo* biological evaluations owing to the collaboration with several teams of biologists.

IV. Structure of the Thesis

In Chapter 1, the most common synthetic approaches and the main outcomes from mechanistic studies are briefly reviewed.

In Chapter 2, the experimental and numerical simulations study, carried out on dilute PVP aqueous solutions irradiated by pulsed electron beams, with the aim of elucidating some of other aspects of the reaction mechanism is presented.

In Chapter 3, the nanogels made of crosslinked PVP with a small amount of grafted acrylic acid (PVP-co-AA), that will be used as substrate for the development of biomedical nanodevices to target two different pathologies - Alzheimer's disease and ColoRectal cancer - are described.

In Chapter 4, the synthesis and characterization of an insulin-nanogel conjugate as potential neuroprotective nanodevice in the treatment of Alzheimer's disease is described.

In Chapter 5, the synthesis and characterization of an AntimiR-31-nanogel conjugate for the potential treatment of colorectal cancer is presented.

Chapter 6 concerns the synthesis and characterization of a Bombesin-DOTA-nanogel conjugate for the potential diagnosis and treatment of colorectal cancer.

List of Abbreviations

AA	Acrylic Acid
Aβ	β Amiloyd Peptide
AD	Alzheimer's Disease
AMT	Ammonium Molybdate Tetrahydrate
BBB	Blood Brain Barrier
BBN	Bombesin
BBN-DOTA	Bombesin-DOTA
BEnd3	Mouse Brain Endothelial Cells
BSA	Bovine Serum Albumin
CD	Conjugation Degree
CNS	Central Nervous System
CRC	Colorectal Cancer
D_H	Hydrodynamic Diameter
DLS	Dynamic Light Scattering
DMSO	Dimethyl Sulfoxide
DOTA	1,4,7,10-Tetraazacyclododecane-1,4,7,10-Tetraacetic Acid
EDC	1-Ethyl-3-[3-Dimethylaminopropyl]Carbodiimide Hydrochloride
EDTA	Ethylenediaminetetraacetic Acid
EPR	Enhanced Permeability And Retention Effect
FAM	Fluorescein Amidite
FBS	Fetal Bovine Serum
FDA	U.S. Food and Drug Administration
FITC	Fluorescein Isothiocyanate
FTIR	Fourier Transform Infrared Spectroscopy
GFC	Gel Filtration Chromatography

GI	Gastrointestinal System
G-value	Radiation Chemical Yield
HD	“High Dose” Conditions
In	Human Insulin
I.n.	Intranasal
In^{FITC}	Human Insulin Labeled With Fluorescein Isothiocyanate
I.p.	Intraperitoneal
IRs	Insulin Receptors
LAN5	Neuroblastoma Cells
LD	“Low Dose” Conditions
LPS	Lipopolysaccharides
MES	2-(N-Morpholino) Ethane Sulfonic Acid
M_W	Weight Average Molecular Weight
Cad-BOC	N-Cadaverine-BOC
NGs	Pvp-Based Nanogel
PAA	Poly(Acrylic Acid)
PAAm	Polyacrylamide
PBMCs	Peripheral Blood Mononuclear Cells
PBS	Phosphate Buffered Saline
PEG	Polyethylene Glycol
PEO	Poly(Ethylene Oxide)
PNIPAM	Poly(N-Isopropyl Acrylamide)
PV	Pyrocatechol Violet
PVA	Poly(Vinyl Alcohol)
PVME	Poly(Vinyl Methyl Ether)
PVP	Poly(N-Vinyl Pyrrolidone)
RES	Reticulendothelial System
SEM	Scanning Electron Microscopy

SLS	Static Light Scattering
Sulfo-NHS	N-Hydroxysulfosuccinimide Sodium Salt
SW620	Colon Cancer Cell Line
TEM	Transmission Electron Microscopy
TJ	Tight-Junctions
TRITC	Tetramethylrhodamine Isothiocyanate Mixed Isomers
VP	1-Vinyl-2-Pyrrolidone

1. Introduction

In this PhD project, radiation-engineered nanogels (NGs) from dilute and semi-dilute polymer aqueous solution are the material systems of choice for the development of biomedical delivery nanodevices.

NG are essentially made by two components: polymer and water. When the nanogels are synthetized by ionizing radiation of aqueous polymer solutions, water is not only a medium in which the process takes place, but it has a key role in the synthetic process. In fact, water radiolysis produces the reactive species responsible of the formation of radical sites along the polymer chains that recombine, mainly intra-molecularly, yielding to the formation of NGs. Hereafter, the main features of the interaction of ionizing radiation with matter, and more in particular with water and polymer solutes in water will be briefly reviewed.

1.1 Ionizing radiation interactions with matter

According the IUPAC definition, ionizing radiation is any radiation consisting of directly or indirectly ionizing particles or a mixture of both, or photons with energy higher than the energy of photons of ultraviolet light, or a mixture of both such particles and photons. [1] In other words, this kind of radiation must have the energy required to eject an electron out of a neutral atom or molecule in its ground state, thus minimum ca. 10 eV, up to several millions of eV. When ionizing radiation interacts with matter several phenomena may occur, including initiation of chemical reactions; excitation of electrons and molecules; ionization of matter; and nuclear reactions, depending on the target material and the energy imparted.

Several types of radiation sources can be employed, such as radioactive nuclei (α-, β- and γ-rays) and high-energy charged particles (electrons, protons, etc) and they can work in continuous or pulsed set-up. They can also be classified taking into account the rate of energy loss by an ionizing particle in the irradiated matter per unit path length, also known as linear energy transfer (LET) and reported in Eq. 1.1.

Eq 1.1 $$LET = -\frac{dE}{dx}$$

Among the Low-LET radiations γ radiations and accelerated e^- can be counted, while heavy ions and α particles are examples of High-LET radiations.

Based on the LET values, the amount of energy deposited during the passage through the matter will be different. In fact, for example an α particles with the same energy of an accelerated e^-, has a higher probability to interact with the medium and it deposits energy along cylindrical "tracks" characterized by high concentrations of ions and excited molecules, while the e^- deposits its energy in small and isolated area or "spurs" in which a small number of ions and excited molecules are located. This different distribution of deposited energy does not have an effect on the types of produced ions and excited molecules, but it has an effect on the proportion of the products.

In order to quantify the radiation-induced chemical effects of the ionising radiation on the irradiated matter, a radiation chemical yield, G(X), known also as G-value, was introduced in 1952 by Milton Burton. [2] G(X) is defined as the quotient of the amount n(X) of a substance X, produced, transformed or destroyed by radiation and the mean energy imparted, E, absorbed in the medium, as shown in the Eq. 1.2.

Eq. 1.2 $$G(X) = \frac{n(X)}{E}$$

In the literature up to 90's, the G-value was expressed as the number of molecules/entities produced, transformed or destroyed per 100 eV of absorbed energy. This unit was then replaced by SI unit, expressed as mol * J^{-1}.

Since only a fraction of the incident radiation is absorbed, another important parameter is the absorbed dose, defined as the mean energy, dE, deposited in an incremental quantity of matter, divided by the mass of the matter, as shown in Eq. 1.3.

Eq. 1.3 $$D = \frac{dE}{dm}$$

According the SI unit, the absorbed dose is expressed in gray (Gy), that is absorbed energy (J) per unit mass (kg), thus 1 Gy = 1 J* kg^{-1}.

1.2 Water Radiolysis

Water has been the most intensive investigated system in radiation chemistry since it plays a key role as a solvent both in chemical and biological systems, but also because it is an example of a simple highly polar liquid.

It was more than one hundred years ago that for the first time the chemical changes induced by ionising radiation on water were observed. In fact, in 1902 Giesel observed the production of molecular hydrogen and oxygen from an aqueous solution of radium bromide. [2]

Since then, the radiolysis of water was deeper investigated and today is experimentally and theoretically well understood [3,4].

When water is subjected to ionizing radiation it undergoes to radiolysis and within 10^{-7} s several species are produced, as shown in Eq. 1.4.

Eq. 1.4 $$H_2O \text{ -^^^^^--> } e^-_{aq},\ \cdot OH,\ \cdot H,\ HO_2^{\cdot},\ H_3O^+,\ OH^-,\ H_2,\ H_2O_2$$

The radiolytic events, that allow the production of these species, can be schematically represented in three stages and their related time scales: physical, physico-chemical and chemical stage.

In the physical stage ($10^{-18} \div 10^{-15}$ s), the initial dissipation of energy takes place and thus the primary radiation interacts with matter producing both excited (Eq. 1.5) and ionized water molecules (Eq. 1.6).

Eq. 1.5 $$H_2O \rightarrow H_2O^*$$

Eq. 1.6 $$H_2O \rightarrow H_2O^+, e^-$$

During the physico-chemical stage ($10^{-15} \div 10^{-12}$ s), several reactions occur in order to establish the thermal equilibrium, like for example ion-molecule reaction (10^{-14} s), homolytic dissociation (10^{-13} s) and solvation of electrons (10^{-12} s), reported in Eq. 1.7-1.9, respectively.

Eq. 1.7 $$H_2O^+ + H_2O \rightarrow H_3O^+ + \cdot OH$$

Eq. 1.8 $$H_2O^* \rightarrow H^\bullet + HO^\bullet$$

Eq. 1.9 $$e^- \rightarrow e^-_{aq}$$

The chemical stage ($10^{-12} \div 10^{-6}$ s) is the stage in which the establishment of the chemical equilibrium occurs through radical-radical reactions in spur and track areas and the consequently diffusion of the radicals and molecular products into the bulk of the medium. While the first two stages are characterized by a heterogeneous distribution of species, once the chemical stage is completed a homogeneous distribution of water radiolysis products is obtained.

In Tab 1.1 an overview of the reactions that can take place and related rate constant are shown.

Table 1.1. Some of the reactions and related rate constants occurred in water radiolysis [4]. Eq.1.24-1.29 take place in the presence of molecular oxygen.

Eq.	Reaction	k ($dm^3\ mol^{-1}\ s^{-1}$)
1.10	$e_{aq}^- + H_2O \rightarrow H^\bullet + OH^-$	19
1.11	$2e_{aq}^- \rightarrow H_2 + 2OH^-$	$5.5 * 10^9$
1.12	$e_{aq}^- + H^\bullet \rightarrow H_2 + OH^-$	$2.5 * 10^{10}$
1.13	$e_{aq}^- + HO^\bullet \rightarrow OH^-$	$3.0 * 10^{10}$
1.14	$e_{aq}^- + H_3O^+ \rightarrow H^\bullet + H_2O$	$2.3 * 10^{10}$
1.15	$H^\bullet + H^\bullet \rightarrow H_2$	$7.8 * 10^9$
1.16	$H^\bullet + HO^\bullet \rightarrow H_2O$	$7.0 * 10^9$
1.17	$HO^\bullet + HO^\bullet \rightarrow H_2O_2$	$5.5 * 10^9$
1.18	$HO^\bullet + H_2O_2 \rightarrow H_2O + HO_2^\bullet$	$2.7 * 10^7$
1.19	$2HO_2^\bullet \rightarrow H_2O_2 + O_2$	$8.3 * 10^5$
1.20	$H_3O^+ + OH^- \rightarrow 2H_2O$	$1.43 * 10^{11}$
1.21	$HO^\bullet + H_2 \rightarrow H_2O + H^\bullet$	$4.2 * 10^7$
1.22	$H^\bullet + H_2O_2 \rightarrow H_2O + HO^\bullet$	$9.0 * 10^7$
1.23	$e_{aq}^- + H_2O_2 \rightarrow OH^- + HO^\bullet$	$1.1 * 10^{10}$
1.24	$e_{aq}^- + O_2 \rightarrow O_2^{\bullet-}$	$1.9 * 10^{10}$
1.25	$H^\bullet + O_2 \rightarrow HO_2^\bullet$	$2.1 * 10^{10}$
1.26	$O_2^{\bullet-} + HO_2^\bullet \rightarrow H_2O_2 + O_2 + OH^-$	$9.7 * 10^7$
1.27	$2HO_2^\bullet \rightarrow H_2O_2 + O_2$	$8.3 * 10^5$
1.28	$O_2^{\bullet-} + HO^\bullet \rightarrow O_2 + OH^-$	$8.0 * 10^9$
1.29	$HO_2^\bullet + HO^\bullet \rightarrow H_2O + O_2$	$6.0 * 10^9$

Some of the reactions listed in Tab 1.1 occur or are favoured only under particular conditions. For example, the reaction shown by Eq. 1.18 is favoured in the case of high-LET radiations. In fact, in this case, hydrogen peroxide reacts with the hydroxyl radical when they are still concentrated in the track, before they diffuse out and a homogeneous distribution of radicals and molecular products is attained.

In the case of air-saturated or oxygen-saturated water, additional reactions take place because of the presence of molecular oxygen and they are shown in Tab 1.1 (Eq.1.24-1.29).

After about 10^{-7} seconds both radicals (e^-_{aq}, ·OH, ·H, HO_2·) and molecular products (H_2, H_2O_2) are homogenously distributed in the system. In order to estimate their radical yields or G-values, both competition kinetics studies with radical scavengers and pulse radiolysis approaches have been employed. The G-values depend on several parameters, such as pH, LET and the dose rate of the radiation, temperature and so on. In Tab 1.2 radical and molecular yields obtained for a moderate dose rate, room temperature and concentration of scavengers less of about $1*10^3$ M, on varying pH and LET value of the radiation are reported.

Table 1.2 Radical and molecular products yields (µmol J^{-1}) as a function of pH and type of radiation. [2]

Radiation	**LET, keV µm^{-1}**	**p H**	**e^-_{aq}**	**·OH**	**·H**	**H_2**	**H_2O_2**	**HO_2·**
γ & e^- (0.1-10 MeV)	0.2-0.3	3-11	0.28	0.28	0.062	0.047	0.073	0.0027
γ & e^- (0.1-10 MeV)	0.2-0.3	0.5	0	0.301	0.378	0.041	0.081	0.0008
^{210}Po α particles (5.3 MeV)	140	0.5	0	0.052	0.062	0.163	0.150	0.011

At low pH (e.g. 0.5) , e^-_{aq} are quickly converted within the spurs in hydrogen atoms once scavenged by the hydrogen ions (Eq. 1.14) and for this reason the G(e^-_{aq}) is equal to zero.

As already said, radiations with high-LET value are characterized by an energy deposition area densely populated by radicals and thus a high probability of radical-

radical reactions to occur. For this reason, as shown in Tab 1.2, the G-values for H_2 and H_2O_2 are higher when α particles are employed.
Nitrous oxide (N_2O) is used to scavenge the e^-_{aq}, according the Eq. 1.30

Eq. 1.30 $$e^-_{aq} + N_2O + H_2O \rightarrow HO^\bullet + HO^- + N_2$$

This reaction will convert all e^-_{aq} into ·OH (untill N_2O consumption) and, in the case of pure and neutral water, the ·OH's G-value will be doubled as a result.
The radiolytic products can be also classified on reducing (e^-_{aq}, $H^\bullet$, H_2) and oxidizing species ($\bullet OH/(O\bullet^-)$, $HO_2^\bullet/(O_2^{\bullet-})$, H_2O_2). Among the reducing species, hydrated electron is the strongest, with a standard potential $E°(H2O/\ e^-_{aq}) = -2.9\ V_{NHE}$, while hydrogen atom has a standard potential equals to $E°(H+/H^\bullet) = -2.3\ V_{NHE}$. Molecular hydrogen, because of its low solubility in water, rarely exploit its reducing ability. Concerning the oxidizing species, hydroxyl radical is a very strong oxidizing specie with a standard potential $E°(HO^\bullet/H_2O) = +2.7\ V_{NHE}$. It is also a weak acid with a $pK_a = 11.9$, and thus a pH ≥ 12 it is present as O^-.

1.3 Radiation engineered nanogels

Nanogels (NGs) are water-swollen nanosized tree-dimensional networks of hydrophilic polymers. According the IUPAC definition, they can be crosslinked networks of any shape with an equivalent diameter of 1–100 nm [1]. They are characterized by tuneable chemical structure, hydrodynamic size and surface properties and, for this reason, they are attractive for numerous application, above all in biomedical field.
The first reports on "strongly branched, 3-dimensional molecules" date back to the 1930s, when formation of styrene–divinylbenzene insoluble particles was described by Staudinger and co-authors. [5,6] Since then, NGs have been synthesized

according several approaches: (i) micro-/nanofabrication methodologies (photolithography, microfluidic, micromoulding); (ii) synthesis from monomers with di- or multifunctional comonomers (crosslinkers) in homogeneous or heterogeneous phase; (iii) self-assembly processes that exploit ionic, hydrophobic or covalent interactions of pre-synthesised polymers; (iv) ionizing radiation-mediated chemical crosslinking of pre-synthesised polymers.

The last synthetic approach is characterized by several distinctive advantages: (i) high energy efficiency [7-9]; (ii) minimal use of potentially harmful chemicals (solvents, catalysts, surfactants); and (iii) simple production schemes.

Typical polymers that mainly undergo crosslinking upon irradiation are poly(N-vinylpyrrolidone) (PVP), poly(ethylene oxide) (PEO), poly(vinyl alcohol) (PVA), poly(vinyl methyl ether) (PVME), poly(N-isopropyl acrylamide) (PNIPAM) polyacrylamide (PAAm) and poly(acrylic acid) (PAA).

In the 1960s for the first time, PVA and PEO micro-/nanogels were synthesized *via* gamma irradiation of dilute aqueous solution of polymers by Sakurada and Ikada [10] and Schnabel and Borwardt [11], respectively. Yet, the first report on nanogels was presented a few years earlier by Charlesby and Alexander [12].

In the late 1990s, Rosiak and Ulanski proposed the use of a pulsed electron beam source. In particular, they developed a closed-loop system, in which the polymer aqueous solutions were continuously pumped to a quartz irradiation cell and subjected to intense (about 1 kGy) pulses of 6 MeV electrons. [13]

Nanogels have also been successfully synthesised using industrial accelerators and the typical set-ups and doses applied for sterilisation (20–40 kGy). Advantages of this approach are (i) an easy scale up of the process; (ii) the possibility to produce already sterile nanogels, which may be an interesting feature for their biomedical applications; (iii) the chemical structure modification of starting polymer with the introduction of useful functional groups. [14-18]

Most of the crosslinking type polymers, including PVP [14,19], PVA [20], PAA [21,22], PVME [23-25], PAAm [26] and polyNIPAM copolymers [27] have been

used to produce nanogels. More recently nanogels have been synthetized also starting from proteins [28,29] and natural polymers, as chitosan [30] using gamma rays.

The formation of NGs upon high-energy irradiation of dilute polymer aqueous solutions can be schematically described as consisting of three phases:
(i) Water radiolysis and formation of the related products;
(ii) Formation of polymer radicals (P•);
(iii) Macroradicals follow-up reactions.

Dilute polymer aqueous solutions are made mainly by water, and thus, ionizing radiations is absorbed essentially by water, that undergoes to radiolysis. For this reason, the radiation chemical yields (G-values) of water radiolysis products can be considered as the ones of pure water (irradiated with the same type of radiation).
In general, among the radiolitically-produced species, only hydroxyl radicals (·OH) and hydrogen atoms (·H) are involved in macroradical formation, essentially via hydrogen abstraction. Both of them are strong electrophilic species, and the rates of hydrogen abstraction from aliphatic and aromatic carbons are characterized by very high values ($k > 10^9$ dm^3 mol^{-1} s^{-1}). [4, 31] If from one hand, high ·OH/·H reactivity favours macroradical formation, on the other hand, being a non-selective process, several kinds of macroradicals can be formed, that in turn may have an effect on the final product. In Fig 1.1, some macroradicals that can be formed by H-abstraction in PAA and PVP are shown.

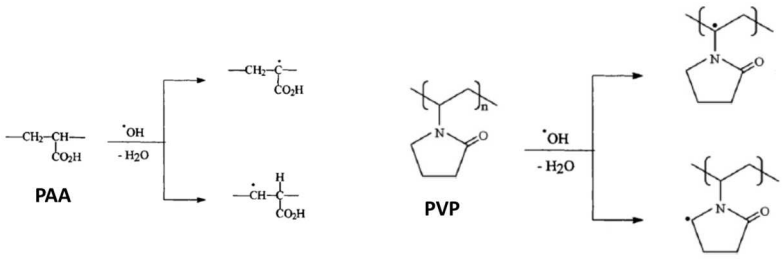

Figure 1.1 Examples of radicals formed via •OH-mediated hydrogen abstraction from PAA and PVP. Adapted from ref [14,21]

As reported in Tab 1.2, the G(·H) is equal about 20% of G(·OH) and when N_2O-saturation is employed prior to irradiation, this value decreases to 10%. For this reason, often macroradical formation is described as the result of the reaction between polymer and hydroxyl radicals (Eq. 1.31).

Eq. 1.31 $$P + {}^{\bullet}OH \rightarrow P^{\bullet}$$

Once the macroradicals are formed, they can evolve according several follow-up reactions:

(1) intra-molecular crosslinking;

(2) inter-molecular crosslinking;

(3) intra-molecular disproportionation;

(4) inter-molecular disproportionation;

(5) hydrogen transfer;

(6) chain scission.

In Fig 1.2 a schematic overview of the follow-up reactions is reported. Furthermore, it is worth mentioning that macroradicals may also react with other solutes present in the solution from before irradiation (for example, with O_2 in O_2- and air-saturated

systems) or produced upon irradiation (H_2O_2 from Eq. 1.17, O_2 from Eq. 1.19), as it will be discussed later.

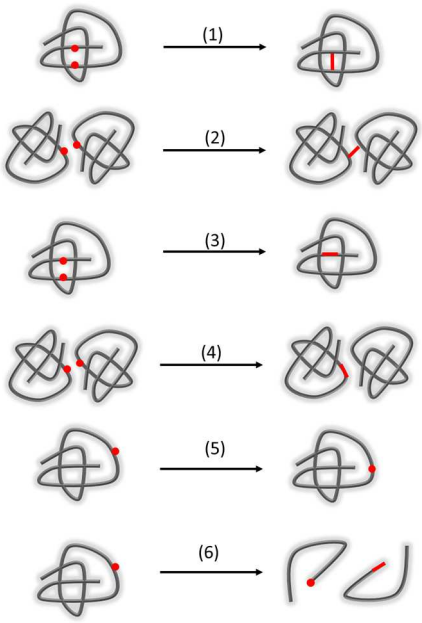

Figure 1.2 Macroradicals follow-up reactions. Red dots represent the radicals; red segments represent new bonds formed upon radiation.

Mechanism of nanogel formation

Despite the simplicity of the synthetic process, the mechanism of nanogel formation is quite complex especially when irradiation is not continuous. In fact, when electron accelerators are employed, energy is imparted in short pulses spaced out by relatively long time intervals without irradiation. Depending on the nature of polymer and the irradiation conditions, the follow-up reactions initiated within one pulse may not be completed before the next electron pulse (for example, at pH 10 the half-life of PAA macroradicals is longer than one hour. [32, 33]

In addition to total absorbed dose, also pulse frequency, pulse length and dose per pulse (or the dose rate within the pulse) have a key role on the reactions kinetics. Since many parameters are involved and many competitive reactions can simultaneously occur, the kinetic analysis is complex.

Often, in order to simplify the kinetic analysis of the macroradical formation step, the assumption of total conversion of water-radiolysis hydroxyl radicals into macroradicals is made. Thus, the radiation chemical yield of macroradicals is assumed equal to the hydroxyl radicals one: $G(P^{\bullet}) \equiv \mathrm{G}(\cdot\mathrm{OH})$. [34] In other words, all the hydroxyl radicals are assumed scavenged by the polymer. This simplification it is not always possible.[35,36] In fact, it can be acceptable when relatively high polymer concentrations are used, since the probability for the polymer to be "caught" by ·OH is high. When the polymer concentration is not high enough, the hydroxyl radicals may be involved in other reactions, such as their recombination to form hydrogen peroxide (H_2O_2). Even though the molar concentration of the polymeric solute in terms of polymer repeating units is relatively high, the fact that the repeating units are not homogeneously distributed in the solution but organised in chains implies that the system is "heterogeneous" in terms of scavenging capacity.

Actually, both polymer concentration and dose per pulse play a crucial role in the non-quantitative conversion of ·OH into macroradicals. Indeed, this effect was shown by pulse radiolysis experiments with spectrophotometric detection carried out with PEO solutions [35,36] and by the experimental determination of H_2O_2 in irradiated PVP solutions at low doses. [18] As a consequence, the same polymer irradiated at different concentrations with the same e-beam irradiation parameters will be subjected to different chemical environments. In fact, at a lower concentration there will be a lower conversion of •OH into P•, and a higher production of H_2O_2. Being hydrogen peroxide a precursor of O_2 under irradiation, the chemistry of C-centred macroradicals will be strongly influenced.

The competition of the two concurrent reactions in which •OH is involved (Eq. 1.17 vs Eq. 1.31) has been also illustrated with the concept of the "active scavenging volume" [37] The active scavenging volume is defined as the volume within which the probability that hydroxyl radical will be scavenged by the polymer is very high. The distance, that corresponds to the average diffusion distance that the hydroxyl radical is able to cover before combination occurs, depends on its lifetime. At high dose rate •OH lifetime is short (high probability of •OH recombination), on the contrary at low dose rate it is high. In Fig 1.3 three different situations of polymer concentration/dose rate are illustrated. In the case of low polymer concentration and low dose rate (Fig 1.3 a-a'), the number of radical sites along the polymer chain is due to the number of hydroxyl radical within the active scavenging volume. This number is function of the polymer concentration. In fact, when with increasing the polymer concentration an overlap of active scavenging volumes occurs (Fig 1.3 b-b'). In this case, the same •OH can reach more than one polymer chain and thus the number of radical sites per polymer chain decreases. In the case of low polymer concentration and higher dose rate (Fig 1.3 c-c'), even though the •OH concentration is higher, its lifetime becomes shorter (higher probability of •OH recombination) and as a consequence the active scavenging volume is reduced, requiring a higher polymer concentration to achieve the full hydroxyl scavenging capacity.

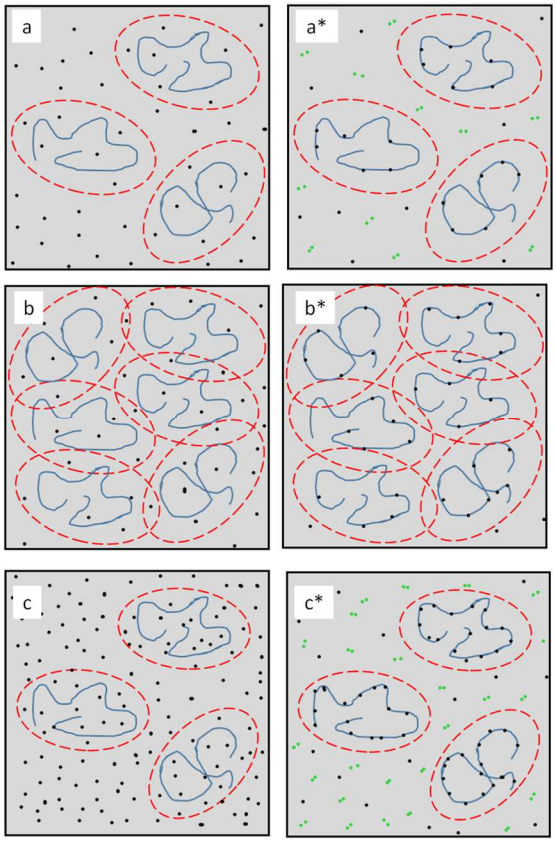

Figure 1.3 Schematic representation of radiolytic radical formation. Solid blue line: polymer chain; dashed red line contours of the ‘‘active scavenging volume’’; black dots hydroxyl radicals formed in water (left panels) and transferred to the polymer (right panels), completely or only partially; pairs of green dots hydrogen peroxide formed from combination of hydroxyl radicals. Three possible situations are represented: a–a* low polymer concentration, relatively low dose rate; b–b* higher polymer concentration, relatively low dose rate; c–c* low polymer concentration, higher dose rate. Adapted from [37]

Among the P• follow-up reactions, crosslinking and disproportionation are termination reactions in which two radicals are involved, chain scission and hydrogen transfer are one-radical propagation reactions. Only intermolecular crosslinking and chain scission cause changes in the polymer molecular weight, while disproportionation and chain scission lead to the formation of double bonds. The double bonds can also react upon irradiation, leading to branching (addition of macroradicals) and/or changes in polymer functionality (addition of hydroxyl radicals, reaction with other solutes, etc.).
The formation of the 3D network is essentially related to inter/intra molecular crosslinking reactions, while radical-radical disproportionation or macroradicals reaction with molecular products formed upon water radiolysis are mainly responsible for the modification of the polymer chemical structure.

In order to synthesize NGs from linear polymers, intramolecular combination should be prevailing over intermolecular combination. Disproportionation always accompanies combination. The ratio between combination and disproportionation is generally constant for a given radical. For example, from studies on product analysis (Mw) on irradiated PAA and PVA the yield of crosslinking was limited to 20-35 and 10%, respectively, and thus in these cases, disproportionation is the main bimolecular termination reaction. [38]

Kinetics study of the follow-up reactions of polymer radicals have been often performed by pulse radiolysis. This approach is generally based on monitoring the disappearance of a radical functionality by time-resolved UV-vis spectroscopic measurements. Under conditions that allow the formation of more than one radical per chain, but also more than one radical-type per repeating unit the kinetics analysis from pulse radiolysis can be difficult. While, in general, only a single type of radical formation and decay has been described, the presence of many radicals per chain

and their different reactivity has been modelled by the so-called dispersive kinetics approach, proposed by Plonka. [39,40]

In general, intermolecular crosslinking is described using classical second order kinetics. Intramolecular crosslinking has been considered a deviation from it. In particular, the rate constant has been assumed to be a function of reaction time, as shown in Eq. 1.32.

Eq. 1.32 $$k(t) = Bt^{\alpha-1}$$

where k(t) is the time-dependent rate constant, t the reaction time, and B and α are two numerical parameters. The parameter α takes in account the deviation from a classical II order decay (a decrease in α corresponds to an increase of deviation for the classical second order) and when α is equal to 1 classical second order kinetics are observed. In particular, through pulse radiolysis, the kinetics of decay of macroradicals formed on PVP, PAA, PVA and PVME, irradiated as deoxygenated aqueous solutions have been followed. [20] The diluted polymer systems were irradiated at high dose rate in order to ensure that a high number of macroradicals per polymer chain was formed and, thus, that intramolecular crosslinking was dominating among all other possible follow-up reactions. In Tab 1.3 the obtained results for α are shown; values between 0.4 and 0.7 were determined.

Table 1.3 Values of the parameter α related to the macroradical decay of PVP, PAA, PVA and PVME diluted aqueous solution subjected to pulse radiolysis and analysed by the dispersive kinetics model in the form of Eq. 1.32.[20]

Polymer	**α**
PVP	0.51 - 0.69
PAA (protonated form)	0.46 - 0.59
PVA	0.40 - 0.53
PVME	0.40 - 0.49

In Jeszka et al. [36], the influence of several parameters on the kinetics of macroradicals recombination *via* intramolecular crosslinking has been discussed. In particular, this study combines pulse radiolysis of PEO in oxygen-free aqueous solutions to Monte Carlo simulations of intramolecular recombination reactions. The simulations have been carried out on simple model cases, such as fixed distance between radicals, formation of loops, radical transfer reactions. It has been demonstrated that the decay half-time depends on the average distance between the radicals (the reaction with the nearest-neighbour radical being always favoured), but, unfortunately, the time dependence of the second-order rate constant is affected by the number of radicals per chain and by the chain length in a complex fashion. Typically, the predicted first half-life of the radical is in the range of 10^{-5} to 10^{-3} s. For multiple radical-bearing polymer chains, the half-life following the first intramolecular combination can be significantly longer.

The influence of polymer concentration and "average" dose rate (obtained from different values of pulse frequency and dose per pulse in the unit time) on the size and molecular weight of the final product has been investigated by two studies conducted on e-beam-irradiated deoxygenated PVP aqueous solutions. [14,15] In particular, four polymer solutions at different concentration have been irradiated with 40 kGy using two different average dose rates of ca. 27.8 and $3.9*10^3$ Gy/s. It has been shown that irradiation at the higher dose rate (for a given polymer concentration) yields smaller particles with lower average molecular weight (Mw) if compared to the ones synthesized at a lower dose rate. Increasing the polymer concentration the particle size increases for both the dose rates, but the concentration dependence of size and molecular weight is more pronounced at the lower dose rate.

So far the polymer radicals follow-up reactions responsible for the formation of the three-dimensional crosslinked network have been discussed but chain scission reactions should also be taken into account.

In oxygen-free solutions, when the chain scission-precursors are C-centred radicals located either on the main chain or close to it, chain scission reactions are very slow and characterized by yields that are close to zero, as it has been shown for PAAm, PVP and PVA (under standard irradiation conditions). [38] Contrariwise, in the case of an ionic polymer, as for example PAA, and in the presence of molecular oxygen as solute, the yield of chain scission is no longer negligible. [38]

Several studies have been conducted on irradiated oxygenated aqueous solution of PVP [41], PEO and PAA [33]. In general, carbon-centred macroradicals reacts with O_2 through a fast and diffusion-controlled reaction leading to the formation of the peroxyl radical ($PO_2^{\bullet}$), as shown in Eq. 1.34.

$$P^{\bullet} + O_2 \rightarrow POO^{\bullet} \qquad \text{Eq 1.34}$$

The rate constant of this reaction is in the order of 10^9 $dm^3mol^{-1}s^{-1}$. In Tab 1.4 the rate constants related to several polymers are reported. [33]

Table 1.4 Rate constant related to O_2 addition to macroradicals of different polymers [33]

Polymer	***k* ($P^{\bullet}+O_2$) [10^8 dm^3 $mol^{-1}s^{-1}$]**
PVP	8.7
PEO	15 (Mw= 200 kDa); 22 (Mw= 20 kDa)
PVA	5.2
PAA, pH 3.5	3.1
PAA, pH 10	1.0

The chemistry of $PO_2^{\bullet}$ is not simple but, in general, the main reaction in which peroxyl radical is involved is chain scission. In Fig 1.4 the main reaction pathways related to the chain scission of a vinyl-type polymer are reported.

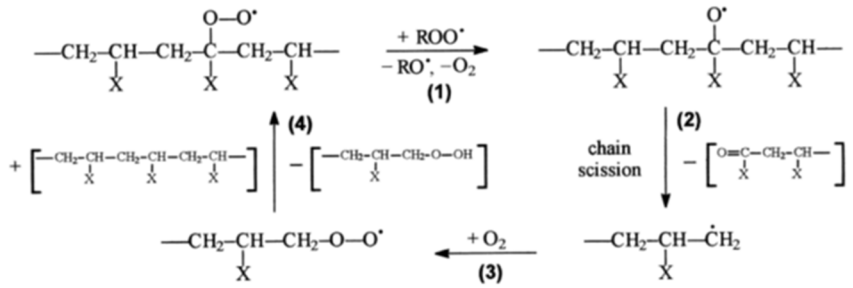

Figure 1.4 Main reaction pathways related to the chain scission of a vinyl-type polymer.[38]

Even though molecular oxygen plays a key role in polymer degradation, crosslinking may still occur. In a study conducted by Rosiak et al [41] on aqueous solution of PVP, it has been shown that crosslinking reactions became dominant increasing the polymer concentration in the system.

Radiation-engineered nanogel functionalization

As already said, disproportions and chain scission reactions lead to the introduction of a double bond but this is not the only chemical modification induced in the polymer upon irradiation. Indeed, in recent studies, it has been pointed out that ionizing irradiation of diluted aqueous polymer solutions not only is able to transform a linear polymer in three-dimensional nanostructure but, is also able to modify its chemical composition. In particular, the introduction of new functionalities, like succinimide, carboxyl groups, primary amino groups, ether-links and hydroxyl groups on PVP-based irradiated systems has been demonstrated [14,18]. It has been also evidenced that these functionalities were produced with a dose-dependence.

For example, in the case of PVP, even though the mechanism behind their formation has not been elucidated yet, the carboxyl groups can only be formed as consequence of the oxidative scission of the polymer backbone or the pyrrolidone ring, while primary amino groups can be formed from the double amino-carbon bond of the

pyrrolidone ring. In both cases, it would seem that these chemical modifications are governed by an oxidative condition-driven mechanism.

In general, the polymer solutions are saturated with N_2O prior to irradiation and thus, the expected oxidative specie would be the hydroxyl radical. As already said, for low polymer concentration the occurrence of $^{\bullet}OH$ recombination in H_2O_2 (precursor of O_2, Eq. 1.17-1.18) may not be neglected and these solutes could be involved in the modification of the chemical composition of the polymer. When macroradicals react with O_2 a peroxyl radical is formed (Eq 1.34) and it can undergo further reactions also producing ketones and carboxyl groups. Furthermore, if the macroradical is reducing, it can react also with H_2O_2 and O_2 according Eq. 1.35 and Eq. 1.36.

$$P^{\bullet} + H_2O_2 \rightarrow P^{+} + OH^{-} + {}^{\bullet}OH \qquad \text{Eq. 1.35}$$

$$P^{\bullet} + O_2 \rightarrow P^{+} + OH^{-} + O_2^{\bullet -} \qquad \text{Eq. 1.36}$$

Examples of reducing agents are carbon-centered radicals with –OR and $–NR_2$ substrituents in the α-position. [37]

Grafting of monomers on radiation-engineered nanogels

The introduction of desired functionalities can be pursued performing the irradiation of polymer-based aqueous solution in the presence of proper solutes. Ionizing irradiation can promote simultaneously crosslinking of linear polymer chains and grafting of useful functionalised monomers on the formed networks. [16,42,43]

Useful chemical functionalities in nanogels to be employed as biomedical nanocarriers are carboxyl groups and/or primary amino groups as they can be employed for the covalent attachment of various (bio)molecules with biological activity. It can be useful also to have the functional group at the end of a loose chain grafted to the network in order to increase its accessibility and hence reactivity

In particular, two different acrylic monomers have been used as grafting agents of PVP nanogels, acrylic acid and 3-aminopropylmethacrilamide, carrying a carboxyl and primary amino group, respectively.[16,42,43] Upon irradiation, monomer radicals may form mainly by •OH (or •H) addition to the monomer (indirect effect). Grafting can occur in different ways: (i) by addition of the polymer radical to the double bond of monomer; (ii) by addition of the monomer radical (•MOH or •MH) to the double bond formed in the polymer chain by disproportionation (iii) by combination between monomer and polymer radicals (P•).

Obviously, the presence of such solutes makes the reactions pathways even more complex. In fact, •OH can be scavenged by both the monomer and the polymer and a decrease of formed macroradicals occurs. Monomer homopolymerization can also be a concurrent reaction. This latter reaction is favoured at higher monomer concentrations, when both the formation of initiating monomer radicals and their propagation by addition of new monomer units can be favoured. In the presence of ionizable groups in the monomer molecular structure, the pH of the irradiated solution has also an effect on monomer homopolymerization. In particular, it is not favoured when the functional groups are in the ionized form since mutual repulsion between the charged monomer molecules occurs.

1.4 From nanogels to nanodevices

Nanogels have been designed and synthesised for several fields of application: (i) in medicine, mainly as drug nanocarriers [44-48], in vivo imaging tracers and biological sensors [49,50], (ii) for separation and water treatment [51,52], (iii) in catalysis [53], and as nano-biomachines [54,56].

In this PhD project, the possibility to employ radiation-engineered PVP-based nanogels as material platform for the development of delivery nanodevices for

biomedical applications is explored.

In these years, the development of pharmaceutical preparations with nanoscalar dimensions has been pursued with the aim to overcome the limits related to the "conventional" drugs. In fact, despite of the many progresses, medicine is afflicted by numerous limitations in diagnosis and treatment of many diseases. Non-specific biodistribution profile, short plasma circulation time and fast systemic elimination characterize most of current therapeutic agents. Furthermore, rare pathologies or pathologies afflicting mainly the undeveloped countries are often neglected. An arduous challenge has been thrown down towards a less invasive medicine and more and more efficacious treatments, that can reduce days of hospitalisation and improve patient compliance.

Polymeric nanomaterials are considered as an opportunity in this field, since they are characterized by an interesting size range, a large surface-to-volume ratio and can be engineered to be stimuli responsive and/or to be decorated with various different (bio)molecules at their surface. Thanks to these properties, they can become nanocarriers able to carry out several functions in parallel, possibly combining diagnosis and therapy. In order to both maximize therapeutic efficacy and minimize unfavourable side effects, the ideal nanocarrier should be able to (i) *protect* the drug minimizing its degradation and inactivation; (ii) *recognize* the pathological site where the drug release is required, avoiding healthy tissues or cells; (iii) *modulate* the release upon an internal or external stimulus; (iv) enable in vivo *diagnosis* or carry out a *tracking* function; (v) be degradable and/or eliminated, once completed its action on the organism. Furthermore, they need to be stable colloids upon storage and administration, and fully biocompatible.

Even when these requirements are satisfied, it is also necessary to investigate their behaviour in a living organism in consideration the various obstacles or biological barriers that they need to cross during the "journey" in the body upon administration. A deep investigation on the factors governing the *Absorption, Distribution, Metabolism and Elimination* (ADME concept) of these materials is

required. [56]

A comprehensive knowledge of the biological system and of how nanomaterials interact with it is a critical issue. In fact, on the basis of the route of administration (parenteral, oral, nasal, etc) and on the basis of target site, nanomaterials will interact with different biological barriers, tissues, organs, cells, receptors, proteins, etc. Furthermore, there is an intricate relationship between all these biological components and the physico-chemical properties of nanomaterials, that will determine the fate of the nanomaterials in terms of clearance from circulation, biodistribution and blood circulation half-life.

The physico-chemical properties of the nanomaterials that mainly influence their interaction with biological components are chemical composition, particle size, surface electric charge, density, surface composition and morphology. They influence to a different extent colloidal stability, biodistribution, clearance from the circulation, accumulation in the various organs and tissues, and degradation or elimination (clearance from the body).

In particular, nanoparticles smaller than 5-6 nm are excreted or rapidly renal-cleared from bloodstream, while larger nanoparticles may be cleared by the immune system involving reticulendothelial system (RES) and opsonisation process. [57] This process consists in the recognition of foreign agents and related binding of opsonins (proteins circulating in the bloodstream) to their surface. Our immune system is able to detect such as “labeled” foreign agents and remove them through the phagocytes action that are accumulated in liver, spleen and lungs.

Nanomaterials surface charge has a strong influence on the colloidal stability, blood circulation time and cellular uptake. A positive charge on the nanomaterials surface improves the interactions with the negatively charged cell membrane, thus facilitating intracellular trafficking, non-specific cellular uptake, but limits the circulation time because of the interaction with extracellular matrix proteins and adsorption of proteins in blood plasma (protein corona). [58,59]

Negatively charged nanocarriers are less affected by the adsorption of proteins in

blood plasma. Furthermore, the repulsive interaction of nanoparticles with negatively charged cells membrane accounts for a low rate of nonspecific cellular uptake. The anionic charge facilitates also renal elimination [60]

The shape and surface composition of the nanomaterial play a key role on the circulation time, extravasation, biodistribution and residence time of nanoparticles inside the cells.

Non-spherical and/or adaptive/flexible particle combined with hydrophilic polymer brushes grafted on the particle surface show a greater colloidal stability, longer blood circulation and a higher cellular uptake. As reported by Agarwal et al., the elongated nanoparticles show greater adhesion to the cells rather than the spherical nanoparticles, since the curve shape limits the number of binding sites on the target cells. [61]

The employment of hydrophilic polymer brushes on the particle surface can reduce the particle opsonization by suppressing the adsorption of biological components in vivo through hydrophilic and steric repulsion effects. Polyethylene glycol (PEG) is the most common hydrophilic polymer employed to form a brushed-nanocarriers. [62]

All these physico-chemical properties have an impact on the fate of the nanomaterials but, in order to allow the recognition and the accumulation at the pathological, passive and/or active targeting strategies need to be devised.

Passive targeting takes advantages from the structural modification of the vascular endothelium, observed in some pathological areas and diseases, such as tumours, inflammations, diabetes, rheumatoid arthritis, and more. This effect, known as Enhanced Permeability and Retention (EPR) effect, discovered by Matsumura and Maeda, [63-65], exploits the leaky and disorganized vasculature with a discontinuous endothelium that, combined to an ineffective lymphatic drainage, allows crossing and accumulation in the surrounding tissue of nanomaterials with a cut-off of ca. 400 nm. [63,66,67]

In the case of tumours, endothelial pores can be characterized by size in the range of

10-1000 nm and the lymphatic vessels, when present, are non-functional causing an ineffective drainage from the tumour tissue. Thus, this particular pathological condition leads to an augmentation of the accumulation and of the residence time of nanoparticles at the diseased area. In the design of cancer-fighting nanodevices, EPR effect is very often used as guiding principle, since it occurs for almost all human cancers with the exception of prostate or pancreatic tumours because of their hypovascularisation. Relying completely on passive targeting may not be not enough, because it has some limitations. In fact, it is not highly selective, it depends on the tumour types, on the sites anatomy and on the degree of tumour vascularisation. For this reason, often an active targeting strategy is joined to the passive one.

Active targeting exploits the over-expression or exclusive expression of molecules/moieties (i.e. membrane receptors) in the pathological area and, through a receptor-ligand mechanism, allows a more selective and enhanced accumulation of the nanomaterials at the desired site. Therefore, based on the specific target, the nanomaterial will be decorated with the proper ligand that can be an antibody, a protein, a peptide, etc., which recognizes and selectively binds to its receptor.

A wide variety of moieties to target both tumoural cells and the tumoural endothelium have been identified. The first kind of targeting agents has the aim to carry the therapeutic agents directly inside the tumour cell to kill them, while the second kind indirectly induces the death of tumour cell by damaging the tumoural endothelium with a related lack in supply of oxygen and nutrients. Among the first group, anti-CD33 monoclonal antibody can be counted to target leukemic cells that, differently from healthy cells, overexpress this monoclonal antibody. Transferrin and folate receptors, that expressed 100-fold more by tumour cells owing to their enhanced methablism, may be used to target tumours and many more. [68,69] Lectin, as carbohydrate-binding proteins, is able to recognize a specific kind of carbohydrate bound to glycoproteins expressed only by cancer cells. This last targeting moiety was proposed for example to target colon cancer, as reported in

[70]. Bombesin and bombesin-like peptides can be employed to bind the bombesin receptor that is overexpressed by prostate, breast, lung and colorectal cancer cells. [71] Among the main targets of the tumoral endothelium can be counted: (i) the vascular endothelial growth factors (VEGF) and their receptors, VEGFR-1 and VEGFR-2, that play a key role in vital functions in tumor angiogenesis and neovascularization [72]; (ii) the αvβ3 integrin that is an endothelial cell receptor involved in the interaction with extracellular matrix proteins (*i.e.* vibronectin, thrombospondin and more) is highly expressed on neovascular endothelial cells in comparison with healthy ones [73]; (iii) the (VCAM-1), a kind of vascular cell adhesion molecule, that plays a key role in the induction of cell to-cell adhesion of tumoral cells. It is expressed on the surface of several cancers, like for example lung and breast cancer, melanoma, renal cell carcinoma, gastric cancer and nephroblastoma. [74]

1.5 Conclusions

Nanogels are an interesting material platform for the development of biomedical nanodevices. Indeed, they offer tuneable physico-chemical properties; colloidal stability; large and flexible surface for multivalent (bio)-conjugation; an internal dynamic 3D aqueous environment for incorporation and protection of (bio)molecular drugs; the possibility to be stimuli responsive (pH, temperature, ionic strength) and biocompatible. The possibility of manufacturing nanogels as aqueous dispersions through high-energy radiation processing with a simple process and at relatively low cost is a key criterion for their continued development and successful application. Despite the apparent simplicity of the synthetic process, the mechanism behind the nanogel formation is quite complex. So far, it has been demonstrated that polymer concentration, dose and dose rate have a key role as tuneable parameters for the simultaneous nanogels formation and functionalization, but still some aspects

need to be clarified. A better understanding of the various irradiation parameters and their possible combined effects offers the possibility to design and synthesized a nanoscalar material with the desired physico-chemical properties and chemical functionalities. These aspects are of fundamental importance for the envisaged application, since they play a key role on the fate and the efficacy of the nanodevice once administrated.

References

[1] Iupac IUPAC (1997) Compendium of Chemical Terminology, 2nd ed. (the ‘‘Gold Book’’). Compiled by A. D. McNaught and A. Wilkinson. Blackwell Scientific Publications, Oxford. XML on-line corrected version: http://goldbook.iupac.org (2006) created by M. Nic, J. Jirat, B. Kosata; updates compiled by A. Jenkins.

[2] S. Le Caër, Water Radiolysis: Influence of Oxide Surfaces on H2 Production under Ionizing Radiation, Water 2011, 3, 235-253.

[3] G.V. Buxton, Radiation Chemistry. Principles and Applications; Farhataziz, Rodgers, M.A.J., Eds.; Verlag Chemie Publishers: Weinheim, Germany, 1987.

[4] J.W.T. Spinks, R.J. Woods, An Introduction to Radiation Chemistry, 3rd ed. Wiley-Interscience publication: New York, NY, USA, 1990.

[5] H. Staudinger, W. Heuer, Über hochpolymere Verbindungen, 94. Mitteil.: Übereinunlösliches Poly-styrol. Chem. Ber., 1934, 67, 1164-1172.

[6] H. Staudinger, E. Husemann, Über hochpolymere Verbindungen, 116. Mitteil: Über das begrenztquellbare Poly-styrol. Chem. Ber.,1935, 68, 1618-1634.

[7] A. J. Berejka, Irradiation processing in the 90’s: energy savings and environmental benefits. Radiat, Phys. Chem., 1995, 46, 429.

[8] S. Machi, Radiat. Radiation technology for sustainable development. Phys. Chem., 1995, 46, 399 .

[9] A. G. Chmielewski, M. Al-Sheikhly, A. J. Berejka, M. R. Cleland, M. Antoniak, Recent development in the application of electron accelerators for polymer processing. Radiat. Phys. Chem., 2014, 94, 147.

[10] I. Sakurada, Y. Ikada, Effects of Gamma Radiation on Polymer in Solution (IX): a turbidimetric study on solution of poly(vinyl alcohol) irradiated below critical concentration for gelformation (Special Issue on Physical, Chemical and Biological Effects of Gamma Radiation, VII). Bull Inst Chem Res Kyoto Univ, 1996, 44(1),66–73.

[11] W. Schnabel, U. Borgwardt, Über die vernetzung von polyäthylenoxid in lösung unter der einwirkung von 60CO-c-strahlen. Makromol Chem, 1969 ,123, 73–79.

[12] A. Charlesby, P. Alexander, Reticulation of polymers in aqueous solution by c-rays. J Chim Phys PCB, 1955, 52, 699–709.

[13] P. Ulanski, J.M. Rosiak, The use of radiation technique in the synthesis of polymeric nanogels. Nucl Instrum Methods Phys Res B, 1999, 151(1–4), 356–360.

[14] M. A. Sabatino, D. Bulone, M. Veres, A. Spinella, G. Spadaro, C. Dispenza, Structure of e-beam sculptured poly(N-vinylpyrrolidone) networks across different length-scales, from macro to nano. Polymer, 2013, 54(1), 54–64.

[15] C. Dispenza, M. A. Sabatino, N. Grimaldi, G. Spadaro, D. Bulone, M.L. Bondı`, G. Adamo, S. Rigogliuso, Large-scale radiation manufacturing of hierarchically assembled nanogels. Chem Eng Trans, 2012, 27, 229C–234C.

[16] C. Dispenza, M.A. Sabatino, N. Grimaldi, D. Bulone, M.L. Bondi, M.P. Casaletto, S. Rigogliuso, G. Adamo, G. Ghersi, Minimalism in radiation

synthesis of biomedical functional nanogels. Biomacromolecules, 201213, 1805–1817.

[17] G. Adamo, N. Grimaldi, M.A. Sabatino, M. Walo, C. Dispenza, G. Ghersi, E-beam crosslinked nanogels conjugated with monoclonal antibodies in targeting strategies. Biol Chem., 2016

[18] C. Dispenza, M. A. Sabatino, N. Grimaldi, M. R. Mangione, M. Walo, E. Murugand, M. Jonsson, On the origin of functionalization in one-pot radiation synthesis of nanogels from aqueous polymer solutions. RSC Adv., 2016, 6, 2582–2591.

[19] S. Kadlubowski, Radiation-induced synthesis of nanogels based on poly(N-vinyl-2-pyrrolidone)— a review. Radiat Phys Chem, 2014, 102, 29–39.

[20] P. Ulanski, I. Janik, J.M. Rosiak, Radiation formation of polymeric nanogels. Radiat Phys Chem., 1998, 52, 289–294.

[21] P. Ulanski, S. Kadlubowski, J.M. Rosiak, Synthesis of poly(acrylic acid) nanogels by preparative pulse radiolysis. Radiat Phys Chem., 2002, 63(3–6), 533–537.

[22] S. Kadlubowski, J. Grobelny, W. Olejniczak, M. Cichomski, P. Ulanski, Pulses of fast electrons as a tool to synthesize poly (acrylic acid) nanogels. Intramolecular cross-linking of linear polymer chains in additive-free aqueous solution. Macromolecules, 2003, 36(7), 2484–2492.

[23] K.F. Arndt, T. Schmidt, R. Reichelt, Thermo-sensitive poly(methyl vinyl ether) micro-gel formed by high energy radiation. Polymer, 2001, 42, 6785–6791.

[24] C. Querner, T. Schmidt, K.F. Arndt, Characterization of structural changes of poly(vinylmethyl ether) gamma-irradiated in diluted aqueous solutions. Langmuir, 2004), 20(7),2883–2889.

[25] T. Schmidt, I. Janik, S. Kadlubowski, P. Ulanski, J. M. Rosiak, R. Reichelt, K.F. Arndt, Pulsed electron beam irradiation of dilute aqueous poly (vinyl methyl ether) solutions. Polymer, 2005, 46(23), 9908–9918.

[26] H. A. A. El-Rehim, Swelling of radiation crosslinked acrylamide-based microgels and their potential applications. Radiat Phys Chem., 2005, 74(2), 111–117.

[27] L. A. Picos-Corrales, A. Licea-Claverie, K. F. Arndt, Stimuli-responsive nanogels by e-beam irradiation of dilute aqueous micellar solutions: Nanogels with pH controlled LCST. Chapter 7: Polymer Nanotechnology. In: Nanotechnology 2012: advanced materials, CNTs, particles, films and composites, vol 1. NSTI publication, 2012.

[28] S. L. Soto Espinoza, M. L. Sanchez, V. Risso, E. E. Smolko, M. Grasselli, Radiation synthesis of seroalbumin nanoparticles. Radiat Phys Chem., 2012, 81, 1417-1421.

[29] Gustavo H.C. Varca, Gabriela G. Perossi, Mariano Grasselli, Ademar B. Lugão, Radiation synthesized protein-based nanoparticles: A technique overview, Radiat Phys Chem., 2014, 105, 48–8201052.

[30] W. Pasanphan, P. Rimdusit, S. Choofong, T. Piroonpan, S. Nilsuwankosit, Systematic fabrication of chitosan nanoparticle by gamma irradiation. Radiat. Phys. Chem., 2010, 79, 1095-1102.

[31] G. V. Buxton, C. L. Greenstock, W.P. Helman, A.B. Ross, Critical review of rate constants for reactions of hydratatedelectrons, hydrogen atoms and hydroxyl radicals (•OH/•O-) in aqueous solutions. J.Phys. Chem. Ref Data, 1988, 17, 513-886.

[32] P. Ulanski, E. Bothe, K. Hildenbrand, J. M. Rosiak, C. Von Sonntag, Hydroxyl-radical-induced reactions of poly(acrylic acid); a pulse radiolysis, e.p.r. and product study. Part I. Deoxygenated aqueous solutions. J. Chem.Soc., Perkin Trans. II 1996, 13.

[33] P. Ulanski, E. Bothe, K. Hildenbrand, J. M. Rosiak, C. Von Sonntag, Hydroxyl-radical-induced reactions of poly(acrylic acid); a pulse radiolysis, e.p.r. and product study. Part II. Oxygenated aqueous solutions. J. Chem. Soc., Perkin Trans. II 1996, 23.

[34] J. C. An, A. Weaver, B. Kim, A. Barkatt, D. Poster, W. N. Vreeland, J. Silverman, M. Al-Sheikhly, Radiation-induced synthesis of poly(vinylpyrrolidone) nanogel. Polymer, 2011, 52, 5746–5755.

[35] P. Ulanski, Zainuddin, J.M. Rosiak, Pulse radiolysis of poly(ethylene oxide) in aqueous solution. ii. decay of macroradicals. Radiat. Phys. Chem., 1995, Vol. 46, No. 4-6, pp. 917-920.

[36] J. K. Jeszka, S. Kadlubowski, P.Ulanski, Monte Carlo simulations of nanogels formation by intramolecular recombination of radicals on polymer chain. Dispersive kinetics controlled by chain dynamics. Macromolecules, 2006, 39, 857–870.

[37] C. Dispenza, G. Spadaro, M. Jonsson, Radiation Engineering of Multifunctional Nanogels, Top. Curr. Chem., 2016, 374, 69.

[38] J. M. Rosiak, P. Ulanski, Synthesis of hydrogels by irradiation of polymers in aqueous solution. Radiation Physics and Chemistry 55 (1999) 139-151.

[39] A. Plonka, Developments in dispersive kinetics. Prog. Reaction Kinetics, 1991,16, 157.

[40] A. Plonka, Dispersive kinetics. Annu. Rep. Prog. Chem., Sect. C. Phys. Chem., 1994, 91, 107.

[41] Rosiak, J., Olejniczak, J., Pekala, W., 1990. Fast reactions of irradiated polymers. I. Crosslinking and degradation of polyvinylpyrrolidone. Radiat. Phys. Chem. 36, 747.

[42] N. Grimaldi, M.A. Sabatino, G. Przybytniak, I. Kaluska, M.L. Bondì, D. Bulone, S. Alessi, G. Spadaro, C. Dispenza, High-energy radiation processing, a smart approach to obtain PVP graft-AA nanogels, Radiat. Phys. Chem., 2014, 9, 76–79.

[43] G. Adamo, N. Grimaldi, S. Campora, D. Bulone, M.L. Bondì, M. Al-Sheikhly, M.A. Sabatino, C. Dispenza, G. Ghersi, Multi-functional nanogels for tumor targeting and redox-sensitive drug and siRNA delivery. Molecules, 2016, 21 art. # 1594.

[44] M. Motornov, Y. Roiter, I. Tokarev, S. Minko, Stimuli-responsive nanoparticles, nanogels and capsules for integrated multifunctional intelligent systems. Prog Polym Sci, 2010, 35, 174–211.

[45] K. Akiyoshi, S. Kobayashi, S. Shichibe, D. Mix, M. Baudys, S. W. Kim, J. Sunamoto, Self assembled hydrogel nanoparticle of cholesterol-bearing pullulan as a carrier of protein drugs: complexation and stabilization of insulin. J Control Release, 1998, 54(3),313–320.

[46] S. Maya, B. Sarmento, A. Nair, N. S. Rejinold, S. V. Nair, R. Jayakumar, Smart stimuli sensitive nanogels in cancer drug delivery and imaging: a review. Curr Pharm Des, 2013, 19(41), 7203–7218.

[47] J. Z. Du, T. M. Sun, W. J. Song, J. Wu, J. A. Wang, Tumor-acidity-activated charge-conversional nanogel as an intelligent vehicle for promoted tumoral-cell uptake and drug delivery. Angew Chem Int Ed, 2010, 49, 3621–3626.

[48] L. Zha, B. Banik, F. Alexis, Stimulus responsive nanogels for drug delivery. Soft Matter, 2011, 7, 5908–5916.

[49] C. K. Lim, A. Singh, J. Heo, D. Kim, K. E. Lee, H. Jeon, J. Koh, I. C. Kwon, S. Kim, Gadolinium coordinated elastic nanogels for in vivo tumor targeting and imaging. Biomaterials, 2013, 34,6846–6852.

[50] W. Wu, S. Zhou, Hybrid micro-/nanogels for optical sensing and intracellular imaging. Nano Rev, 2010, 1, 5730.

[51] K. Kondo, N. Kaji, S. Toita, Y. Okamoto, M. Tokeshi, K. Akiyoshi, Y. Baba, DNA separation by cholesterol-bearing pullulan nanogels. Biomicrofluidics, 2010, 4(3), 32210–32218.

[52] M. A. Akl, A. A. Sarhan, K. R. Shoueir, A. M. Atta, Application of crosslinked ionic poly(vinylalcohol)nanogel as adsorbents for water treatment. J Dispers Sci Technol, 2013, 34(10), 1399–1408.

[53] M. Resmini, K. Flavin, D. Carboni, Microgels and nanogels with catalytic activity. Top Curr Chem, 2012, 325, 307–342.

[54] I. Varga, I. Szalai, R. Me´szaros, T. Gila´nyi, Pulsating pH-responsive nanogels. J Phys Chem B, 2006, 110(41), 20297–20301.

[55] T. Sakai, R. Yoshida, Self-oscillating nanogel particles. Langmuir, 2004, 20(4), 1036–1038.

[56] E. Markovsky, H. Baabur-Cohen, A. Eldar-Boock, L. Omer, G. Tiram, S. Ferber, P. Ofek, D. Polyak, A. Scomparin, R. Satchi-Fainaro. Administration, distribution, metabolism and elimination of polymer therapeutics. Journal of Controlled Release, 2012, 161, 446–460.

[57] M. A. Phillips, M. L. Gran, N. A. Peppas. Targeted Nanodelivery of Drugs and Diagnostics. Nano Today. 2010 April 1; 5(2): 143–159. doi:10.1016/j.nantod.2010.03.003.

[58] H. Zou, Z. Wang, M. Feng, Nanocarriers with tunable surface properties to unblock bottlenecks in systemic drug and gene delivery. Journal of Controlled Release, 2015, 214,121–133.

[59] D. Fischer, Y. X. Li, B. Ahlemeyer, J. Krieglstein, T. Kissel, In vitro cytotoxicity testing of polycations: influence of polymer structure on cell viability and hemolysis. Biomaterials, 2003, 24, 1121–1131.

[60] F. Alexis, E. Pridgen, L. K. Molnar, O. C. Farokhzad, Factors Affecting the Clearance and Biodistribution of Polymeric Nanoparticles. Molecular pharmaceutics vol. 5, NO. 4, 505–515.

[61] R. Agarwal, V. Singh, P. Jurney, L. Shi, S. Sreenivasan, K. Roy, Mammalian cells preferentially internalize hydrogel nanodiscs over nanorods and use shape-specific uptake mechanisms. Proc Natl Acad Sci, 2013, 110, 17247–52.

[62] A. Albanese, P. S. Tang, W. C. W. Chan, The Effect of Nanoparticle Size, Shape, and Surface Chemistry on Biological Systems. Annu. Rev. Biomed. Eng., 2012, Vol. 14, 1-16.

[63] Y. Matsumura, H. Maeda, A new concept for macromolecular therapeutics in cancer chemotherapy: mechanism of tumoritropic accumulation of proteins and the antitumor agent smancs. Cancer Res., 1986, 46, 6387–6392.

[64] H. Maeda, T. Sawa, T. Konno, Mechanism of tumor-targeted delivery of macromolecular drugs, including the EPR effect insolid tumor and clinical overview of the prototype polymeric drug SMANCS, J. Control. Release, 2001, 74, 47–61.

[65] H. Maeda, G. Y. Bharate, J. Daruwalla, Polymeric drugs for efficient tumortargeted drug delivery based on EPR-effect, Eur. J. Pharm. Biopharm., 2009, 71, 409–419.

[66] J. Fang, H. Nakamura, H. Maeda, The EPR effect: unique features of tumor bloodvessels for drug delivery, factors involved, and limitations and augmentation of the effect, Adv. Drug Deliv. Rev.,2011, 63, 136–151.

[67] S. K. Hobbs, et al. Regulation of transport pathways in tumor vessels: Role of tumor type and microenvironment. Proc. Natl. Acad. Sci. U.S.A. 1998, 95, 4607–4612.

[68] Z.M. Qian, H. Li, H. Sun, K. Ho, Targeted drug delivery via the transferrin receptor-mediated endocytosis pathway, Pharmacol. Rev., 2002, 54, 561–587.

[69] A. Gabizon, H. Shmeeda, H. Baabur, R. Satchi-Fainaro, Targeting the folate receptor with liposomes and polymer therapeutics, in: C. Leamon, A. Jackman (Eds.), Targeted Drug Strategies for Cancer and Inflammation, Springer-Verlag, Heidelberg, Germany, 2011, pp. 217–247.

[70] T. Minko, Drug targeting to the colon with lectins and neoglycoconjugates, Adv. Drug Deliv. Rev., 2004, 56, 491–509.

[71] H. Zhang, J. Chen, C. Waldherr, Karin Hinni, B. Waser, J. C. Reubi, Helmut, R. Maecke, Synthesis and Evaluation of Bombesin Derivatives on the Basis of Pan-Bombesin Peptides Labeled with Indium-111, Lutetium-177, and Yttrium-90 for Targeting Bombesin Receptor-Expressing Tumours, Cancer Research, 2004, 64, 6707–6715.

[72] M. Shadidi, M. Sioud, Selective targeting of cancer cells using synthetic peptides, Drug Resist. Updat., 2003, 6, 363–371.

[73] J. S. Desgrosellier, D. A. Cheresh, Integrins in cancer: biological implications and therapeutic opportunities, Nat. Rev. Cancer, 2010, 10, 9–22.

[74] A. Dienst, A. Grunow, M. Unruh, B. Rabausch, J. E. Nor, J. W. Fries, C. Gottstein, Specific occlusion of murine and human tumor vasculature by VCAM-1-targeted recombinant fusion proteins, J. Natl Cancer Inst., 2005, 97, 733–747.

2. Experimental and numerical simulations study of diluted polymer solutions irradiated by pulsed electron beams

2.1. Introduction

The radiation chemistry of dilute polymer solutions subjected to e-beam irradiation from electron accelerators working in pulsed mode is fairly complex because of the intermittent nature of the initiation reactions. The system is constituted by water, polymer and other solutes deriving from the gaseous atmosphere and produced by water radiolysis. The polymer itself contributes significantly to this complexity, concentrating a large number of repeating units in a relatively small volume element, continuously changing its molecular weight, hence diffusivity, chemical composition, conformation and segmental mobility.

Elucidating the mechanism of nanogels formation has a significant impact in the design and production of these nanomaterials, straightening the confidence in the robustness of the synthetic process, clarifying the composition of the obtained products, and opening the space for new macromolecular architectures.

The work described here is aimed to analyse two pulsed e-beam irradiation conditions, used to transform dilute (or semi-dilute) aqueous solutions of PVP into nanogel dispersions. In one set of irradiations, the vials containing the polymer solution were individually placed in front of the beam of a 9 MeV Microtron electron accelerator (Fig 2.1-a). In another set of irradiations several samples, horizontally placed inside a box, were conveyed under the beam of a 10 MeV accelerator by means of a transporter belt (Fig 2.1-b). The electron beam scans the box along the width with a given frequency. As a result, the samples absorb the irradiation dose in a number short trains of fast pulses separated by relatively long dark times between the sweeps. The electron beam set up ensures a specific overall absorbed dose per pass to all vials in the box. This experimental set-up is typically used for industrial sterilisation processes, where

the sterilisation dose must be delivered to large volumes of material with a high throughput.

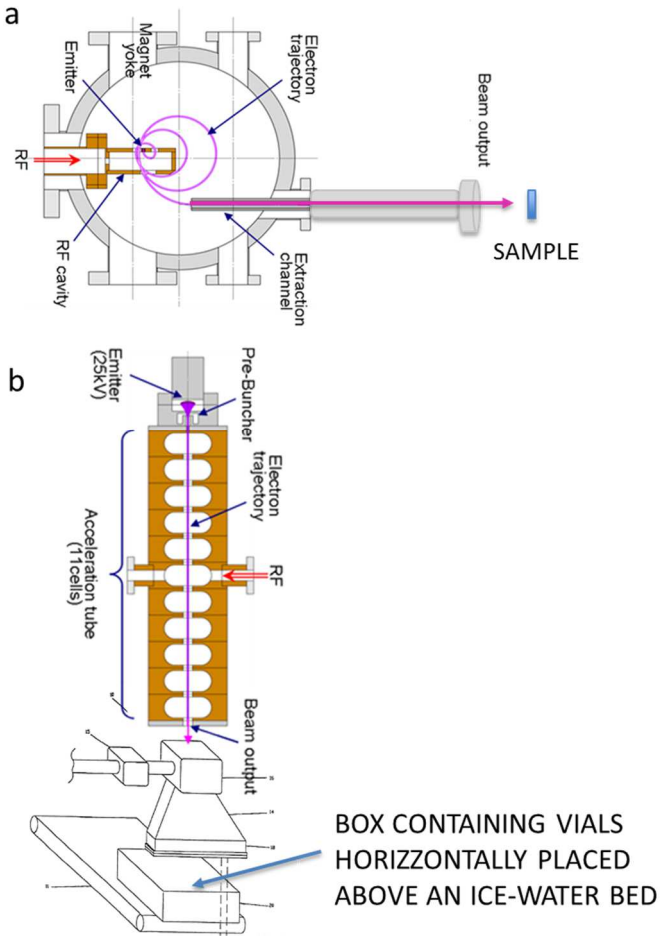

Figure 2.1 Scheme of the two accelerators: the 9 MeV Microtron electron accelerator (a) and the 10 MeV linear accelerator (b).

The main structural modifications of the polymer irradiated at various concentrations and doses with the two set-ups were investigated by dynamic light scattering (DLS) and static light scattering (SLS) and gel filtration chromatography (GFC).

Since varying the irradiation conditions and polymer concentration, the polymer may not be able to scavenge all the hydroxyl radicals produced in the system by water radiolysis, any eventual H_2O_2 present in the system, as a result of hydroxyl radicals recombination, was determined by the Ghormley triiodide method. [1] This method estimates the concentration of H_2O_2 from the I_3^- produced by its reaction with I^-, by means of UV-vis absorbance measurements.

The experimentally measured H_2O_2 concentrations were compared with the values obtained from the numerical simulation of the reactions occurring in pure water and in the presence of a hydroxyl radical scavenger. The simulations were based on all reactions that are involved in the radiolysis of water, using rate constants and G-values available from the literature. The details are provided in par. 2.2.5. The simulations were run iteratively for the whole duration time/dose of irradiation, with the specific time function (i.e. pulse duration time, dose rate within the pulse and dark times) used for each of the experimental set-ups.

In a first set of simulations, the production of H_2O_2 was studied as a function of dose for N_2O- and air-saturated pure water. The simulated H_2O_2 profiles were compared with the experimentally measured values. Since the simulations generate data for all reactants and products as a function of dose/irradiation time, we also calculated the concentration of O_2 present in the system.

In a second set of simulations the impact of the presence of a hydroxyl radical scavenger on H_2O_2 and O_2 profiles was studied. The concentration of the molecular scavenger in the system was “locked” to mimic the large number of abstractable hydrogen atoms of the polymer. The scavenger initial concentration was systematically varied until we could obtain a H_2O_2 profile similar to the experimental one obtained for the lowest polymer concentration. Then, the initial concentration of the scavenger was increased as the weight concentration of polymer in the

experiments. All the reactions involving the polymer radicals have not been included at this stage and will consititute the next stage of development of the simulation code. Measurements of I_3^- absorbance for the determination of H_2O_2, carried out as function of the time, revealed the occurrence of a competitive, relatively slower reaction that was consuming I_3^-. The cause of this reaction was investigated and identified. This enabled a more complete description of the chemical modifications occurring in the irradiated polymer in its "metamorphosis" from a linear chain of vinyl pyrrolidone units into a multifunctional nanoscalar network.

2.2. Experimental

2.2.1. Materials

Poly(N-vinyl pyrrolidone) (PVP k60 and PVP 1300000 with M_w=0.41 and 0.64 MDa (from static light scattering measurements [2,3] and characterized by a critical hydrodynamic concentrations of ~ 1 wt% [2] and ~ 0.85 wt% [3], respectively) were purchased from Sigma Aldrich. Potassium iodide 99.0 wt% (KI, VWR BDH Prolabo), ammonium molybdate tetrahydrate (AMT, VWR), sodium acetate (NaAc, Sigma Aldrich), acetic acid 99.0 wt% (HAc, Sigma aldrich), hydrogen peroxide 30.0 vol% (Sigma Aldrich), 1-Vinyl-2-pyrrolidone (VP, Sigma Aldrich), N-cadaverine-BOC (Cad-BOC, Sigma Aldrich), glutharaldehyde (GA, Sigma Aldrich), poly(acrylic acid) (PAA, M_v=0.45 MDa, Sigma Aldrich), fluorescamine (Sigma Aldrich), acetonitrile (Sigma Aldrich), pyrocatechol violet (PV, Sigma Aldrich), Nickel(II) chloride hexahydrate, Hepes (Sigma Aldrich), Pullulan standard solutions (M_w=0.2-2.56 MDa, Sigma Aldrich) were all used as received.

2.2.2. Electron beam irradiation of PVP solutions

Electron-beam irradiations were carried out in two with a 9 MeV Microtron electron accelerator (KTH, Royal Institute of Technology, Stockholm) at average beam current of 65 mA, pulse length of 50 ns, pulse repetition frequency of 25 Hz and with a 10

MeV linear accelerator (Elektronika 10/10, ICHTJ Warsaw) equipped with a scan horn, at average beam current of 380 mA, pulse length of 5 μs and pulse repetition rate of 400 Hz.

With the first set-up, samples of PVP k60 aqueous solutions were individually irradiated in 10 ml sealed vials. The vial is vertically placed in front of the beam at a distance of 3 cm from the beam output (Fig. 2.1). The dose per pulse is of 0.8 Gy, as determined by both Fricke and ferrous cupric sulfate dosimetry. [4] Doses in the range of 0.3-4.8 kGy were imparted varying the exposure time. These systems are collectively named "Low Dose" (LD) systems.

In the second set-up, several 20 ml vials filled with PVP 1.300.000 solution for ¾ of their volume were horizontally placed in a box filled with ice (4–8 °C) and conveyed under the beam via a transporting belt at a speed of 0.48 m min^{-1}. The beam is scanned over the samples with a triangular scan frequency of 5 Hz. The scan length is 850 mm at a distance 355 mm from the window (conveyor surface) and beam cross-section diameter is 50 mm. The samples absorb 20 ± 0.14 kGy per pass, as determined using a graphite calorimeter.

Samples were irradiated also at 40, 60 and 80 kGy total absorbed doses by multiple pass exposure. These systems are collectively named "High Dose" (HD) systems.

With both set-ups, 0.22 μm syringe filtered solutions at various polymer concentrations, from 0.05 to 0.5 wt%, were irradiated in sealed vials either in the presence of air or after thorough purging with N_2O.

Each irradiated system is coded as X_YZ, where X is the concentration of PVP in the aqueous solution (wt%); Y defines the irradiation conditions (LD or HD); Z is the total absorbed dose in kGy. "Air" was added to the code to distinguish them from their N_2O-saturated analogues irradiated systems. All the details are summarized in Tab 2.1. Pure water was also irradiated in all the above irradiation conditions.

Table 2.1. Overview of system compositions and irradiation conditions

	LD systems	HD systems
System composition		
Polymer M_w (MDa)	0.41	0.64
Critical hydrodynamic concentration (wt%)	~ 1	~ 0.85
Polymer concentration (wt%)	0.05 - 0.5	0.05 - 0.5
Polymer concentration (μM)	1.2 - 12	0.77 - 7.7
PVP repeating unit concentration (mM)	4.5 - 45	4.5 - 45
Atmosphere	N_2O Air	N_2O Air
Accelerator set up parameters		
Current (mA)	65	380
Frequency (Hz)	25	400
Pulse length (μs)	0.05	5.0
Dose rate per pulse (MGy/s)	16	32
Dose per pass	n.a.	20 kGy
Total Abs Dose (kGy)	0.6 - 4.8	20 - 80
Ice Bath	NO	YES

2.2.3. Physico-chemical characterization of irradiated poly(N-vinyl pyrrolidone)s

The hydrodynamic diameters (D_H) of the irradiated polymers in water were measured by dynamic light scattering (DLS) (for more details see Appendix A.1). The irradiated systems were analysed as produced and after 0.45 μm cut-off syringe filtration.

The weight average molecular weight of the irradiated polymers in water were measured by static light scattering (SLS). More details are reported in Appendix A.2

Hydrodynamic volume distributions were determined by Gel Filtration Chromatography (see Appendix A.3) The measurements were performed at 0.05 wt% polymer concentration with addition of 0.02 wt% of sodium azide after 0.45 μm cut-off syringe filtration. The two non irradiated PVP variants and Pullulan standard solutions (M_w=0.2-2.56 MDa) were also treated and analysed in the same conditions.

2.2.4. Determination of H_2O_2 production

The amount of H_2O_2 produced in the irradiated systems was evaluated using the Ghormley triiodide method. [1]

In particular, in the presence of the catalyst (AMT), H_2O_2 oxidizes I^- into I_2 (Eq. 2a) and, I_3^- is obtained as a result of the equilibrium reaction between the three iodine oxidation states (Eq. 2b).

Eq. 2a $$2\,I^- + H_2O_2 \rightleftharpoons I_2 + 2\,OH^-$$

Eq. 2b $$I_2 + I^- \rightleftharpoons I_3^-$$

The concentration of H_2O_2 in the system is determined by UV-vis spectroscopy measuring the I_3^- absorbance at peak (λ_{max} = 350 nm). A calibration curve was built by plotting I_3^- absorbance at peak as a function of known concentrations of H_2O_2 solutions in 5-35 µM range, as shown in Fig. 2.2 A molar extinction coefficient of 25.0 10^3 M^{-1} cm^{-1} was estimated. In particular, 65 µl of the irradiated sample was diluted in 2.275 ml of milliQ water, mixed with 130 µl of KI (1 M) and 130 µl of HAc/NaAc (1 M) after addition of few drops of AMT (4 %wt/v). The full UV-vis absorption spectrum (200-800 nm) was acquired immediately after the preparation and after different time intervals (5, 15, 30 minutes and 24 hours), and no peak shifts were detected over time. Instead, for the HD-systems, a gradual decrease of the

absorbance at peak with time was observed. Therefore, for these systems the time-course variation of absorbance at λ_{max} was also acquired.

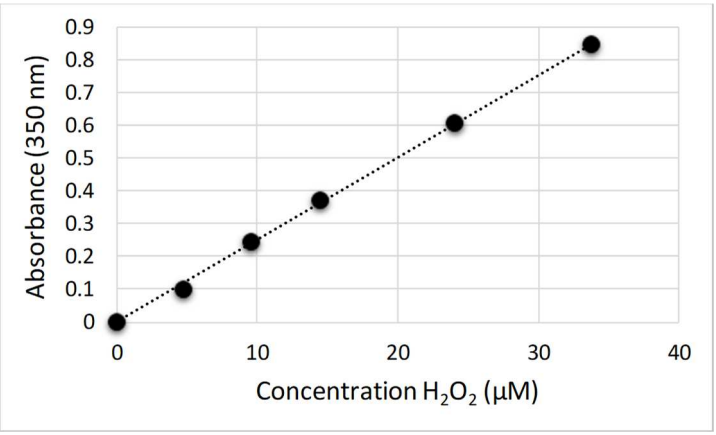

Fig 2.2. UV-vis calibration curve (ΔAbs=350 nm) for H_2O_2 water solutions.

2.2.5. Numerical Simulations

The pulsed radiolysis was modelled as a system of ordinary differentials equations. Rate constants describing aqueous radiolysis (reaction from 1 to 46), N_2O-electron scavenging reaction (reaction 47) and the hydroxyl radical-scavenger reaction (reaction 48) were taken from the literature [5-7], respectively. For reaction 49 and 50 typical alkyl-alkyl and alkyl-O_2 rate were taken into account. All the rate constants are reported in Tab. 2.2. In Tab 2.3 the G-values used in the numerical simulations are reported.

Two software packages (ChemPy[8] and Pyodesys[9]) were used to formulate the equations, pulse sequences and perform the integration and analyse the results. The results presented here used the Sundials library [10] for the numerical integration.

Tab 2.2. Reactions and related rate constants taken into account for the numerical simulations

Id	Reaction			k
1	$2\ e^-_{(aq)} + (\ 2\ H_2O)$	→	$H_2 + 2\ OH^-$	$7.2598 \cdot 10^9$ ($dm^3\ mol^{-1}\ s^{-1}$)
2	$2\ H^\bullet$	→	H_2	$5.1417 \cdot 10^9$ ($dm^3\ mol^{-1}\ s^{-1}$)
3	$2\ {}^\bullet OH$	→	H_2O_2	$4.814 \cdot 10^9$ ($dm^3\ mol^{-1}\ s^{-1}$)
4	$e^-_{(aq)} + H^\bullet + (\ H_2O)$	→	$H_2 + OH^-$	$2.7621 \cdot 10^{10}$ ($dm^3\ mol^{-1}\ s^{-1}$)
5	$e^-_{(aq)} + {}^\bullet OH$	→	OH^-	$3.5532 \cdot 10^{10}$ ($dm^3\ mol^{-1}\ s^{-1}$)
6	$H^\bullet + {}^\bullet OH$	→	H_2O	$1.0937 \cdot 10^{10}$ ($dm^3\ mol^{-1}\ s^{-1}$)
7	$e^-_{(aq)} + H_2O_2$	→	${}^\bullet OH + OH^-$	$1.3616 \cdot 10^{10}$ ($dm^3\ mol^{-1}\ s^{-1}$)
8	$e^-_{(aq)} + O_2$	→	$O_2^{\bullet-}$	$2.2905 \cdot 10^{10}$ ($dm^3\ mol^{-1}\ s^{-1}$)
9	$e^-_{(aq)} + O_2^{\bullet-} + (\ 2\ H_2O)$	→	$H_2O_2 + 2\ OH^-$	$1.2982 \cdot 10^{10}$ ($dm^3\ mol^{-1}\ s^{-1}$)
10	$e^-_{(aq)} + HO_2^\bullet$	→	$HO_2^{\bullet-}$	$1.2982 \cdot 10^{10}$ ($dm^3\ mol^{-1}\ s^{-1}$)
11	$H^\bullet + H_2O_2$	→	${}^\bullet OH + H_2O$	$3.6503 \cdot 10^7$ ($dm^3\ mol^{-1}\ s^{-1}$)
12	$H^\bullet + O_2$	→	$HO_2^\bullet$	$1.3077 \cdot 10^{10}$ ($dm^3\ mol^{-1}\ s^{-1}$)
13	$H^\bullet + HO_2^\bullet$	→	$2\ {}^\bullet OH$	$1.1384 \cdot 10^{10}$ ($dm^3\ mol^{-1}\ s^{-1}$)
14	$H^\bullet + O_2^{\bullet-}$	→	HO_2^-	$1.1384 \cdot 10^{10}$ ($dm^3\ mol^{-1}\ s^{-1}$)
15	${}^\bullet OH + H_2O_2$	→	$HO_2 + H_2O$	$2.9195 \cdot 10^7$ ($dm^3\ mol^{-1}\ s^{-1}$)
16	${}^\bullet OH + O_2^{\bullet-}$	→	$O_2 + OH^-$	$1.0974 \cdot 10^{10}$ ($dm^3\ mol^{-1}\ s^{-1}$)
17	${}^\bullet OH + HO_2^\bullet$	→	$O_2 + H_2O$	$8.84 \cdot 10^9$ ($dm^3\ mol^{-1}\ s^{-1}$)
18	$2\ HO_2^\bullet$	→	$H_2O_2 + O_2$	$8.3993 \cdot 10^5$ ($dm^3\ mol^{-1}\ s^{-1}$)
19	$O_2^{\bullet-} + HO_2^\bullet + (\ H_2O)$	→	$H_2O_2 + O_2 + OH^-$	$1.0116 \cdot 10^8$ ($dm^3\ mol^{-1}\ s^{-1}$)
20	$H_2O_2 + (\ H_2O_2)$	→	$O_2 + 2\ H_2O$	$1.2975 \cdot 10^{-7}\ s^{-1}$
21	${}^\bullet OH + HO_2^{\bullet-}$	→	$H_2O + O_2^{\bullet-}$	$4.0671 \cdot 10^9$ ($dm^3\ mol^{-1}\ s^{-1}$)
22	$O^{\bullet-} + H_2O_2$	→	$OH^- + HO_2^\bullet$	$4.0671 \cdot 10^9$ ($dm^3\ mol^{-1}\ s^{-1}$)
23	$O^{\bullet-} + HO_2^{\bullet-}$	→	$OH^- + O_2^{\bullet-}$	$7.8637 \cdot 10^8$ ($dm^3\ mol^{-1}\ s^{-1}$)
24	$O^{\bullet-} + H_2$	→	$OH^- + H^\bullet$	$1.2793 \cdot 10^8$ ($dm^3\ mol^{-1}\ s^{-1}$)
25	H_2O	→	$H^+ + OH^-$	$2.1161 \cdot 10^{-5}\ s^{-1}$
26	$H^+ + OH^-$	→	H_2O	$1.1777 \cdot 10^{11}$ ($dm^3\ mol^{-1}\ s^{-1}$)
27	H_2O_2	→	$H^+ + HO_2^{\bullet-}$	$0.09428\ s^{-1}$
28	$H^+ + HO_2^{\bullet-}$	→	H_2O_2	$5.0222 \cdot 10^{10}$ ($dm^3\ mol^{-1}\ s^{-1}$)
29	$H_2O_2 + OH^-$	→	$HO_2^{\bullet-} + H_2O$	$1.3303 \cdot 10^{10}$ ($dm^3\ mol^{-1}\ s^{-1}$)
30	$HO_2^{\bullet-} + H_2O$	→	$H_2O_2 + OH^-$	$1.2734 \cdot 10^6$ ($dm^3\ mol^{-1}\ s^{-1}$)

31	$^{\bullet}OH$	→	$H^+ + O^{\bullet-}$	0.09428 s^{-1}
32	$H^+ + O^{\bullet-}$	→	$^{\bullet}OH$	$5.0222 \cdot 10^{10}$ ($dm^3\ mol^{-1}\ s^{-1}$)
33	$^{\bullet}OH + OH^-$	→	$O^{\bullet-} + H_2O$	$1.3303 \cdot 10^{10}$ ($dm^3\ mol^{-1}\ s^{-1}$)
34	$O^{\bullet-} + H_2O$	→	$^{\bullet}OH + OH^-$	$1.2734 \cdot 10^{6}$ ($dm^3\ mol^{-1}\ s^{-1}$)
35	$HO_2^{\bullet}$	→	$H^+ + O_2^{\bullet-}$	$7.7266 \cdot 10^{5}$ s^{-1}
36	$H^+ + O_2^{\bullet-}$	→	$HO_2^{\bullet}$	$5.0222 \cdot 10^{10}$ ($dm^3\ mol^{-1}\ s^{-1}$)
37	$HO_2^{\bullet} + OH^-$	→	$O_2^{\bullet-} + H_2O$	$1.3303 \cdot 10^{10}$ ($dm^3\ mol^{-1}\ s^{-1}$)
38	$O_2^{\bullet-} + H_2O$	→	$HO_2 + OH^-$	0.15538 ($dm^3\ mol^{-1}\ s^{-1}$)
39	$H^{\bullet}$	→	$H^+ + e^-_{(aq)}$	5.8322 s^{-1}
40	$H^+ + e^-_{(aq)}$	→	$H^{\bullet}$	$2.0949 \cdot 10^{10}$ ($dm^3\ mol^{-1}\ s^{-1}$)
41	$H^{\bullet} + OH^-$	→	$e^-_{(aq)} + H_2O$	$2.4404 \cdot 10^{7}$ ($dm^3\ mol^{-1}\ s^{-1}$)
42	$e^-_{(aq)} + H_2O$	→	$H^{\bullet} + OH^-$	15.751 ($dm^3\ mol^{-1}\ s^{-1}$)
43	$H^{\bullet} + H_2O$	→	$H_2 + {}^{\bullet}OH$	$4.5752 \cdot 10^{-5}$ ($dm^3\ mol^{-1}\ s^{-1}$)
44	$H_2 + {}^{\bullet}OH$	→	$H^{\bullet} + H_2O$	$3.9535 \cdot 10^{7}$ ($dm^3\ mol^{-1}\ s^{-1}$)
45	$O^{\bullet-} + O_2$	→	$O_3^{\bullet-}$	$3.7474 \cdot 10^{9}$ ($dm^3\ mol^{-1}\ s^{-1}$)
46	$O_3^{\bullet-}$	→	$O^{\bullet-} + O_2$	2616.9 s^{-1}
47	$N_2O + e^-_{(aq)}$	→	$N_2 + O^{\bullet-}$	$9.6 \cdot 10^{9}$ ($dm^3\ mol^{-1}\ s^{-1}$)
48	$C_4H_{10}O + {}^{\bullet}OH$	→	$C_4H_{10}O + C_4H_9O + H_2O$	$6 \cdot 10^{8}$ ($dm^3\ mol^{-1}\ s^{-1}$)
49	$2\ C_4H_9O$	→	$C_8H_{18}O_2$	10^{9} ($dm^3\ mol^{-1}\ s^{-1}$)
50	$C_4H_9O + O_2$	→	$C_4H_9O_3$	10^{9} ($dm^3\ mol^{-1}\ s^{-1}$)

Tab 2.3. Radical and molecular products yields (μmol J^{-1}) used in the numerical simulations.

$e^-_{(aq)}$	H_2O_2	H_2	$^{\bullet}OH$	$^{\bullet}H$	H^+	H_2O	O_2
0.285	0.074	0.045	2.90	0.062	0.285	-0.438	$2.73 \cdot 10^{-6}$

2.2.6. Functional groups characterisation

The chemical structure modification of the polymer was investigated by FTIR analysis and colorimetric titrations. More details are reported in appendix A.6

2.3 Results and discussion

2.3.1. Physico-chemical characterisation of poly(N-vinyl pyrrolidone)s irradiated as N_2O-saturated aqueous solution

In Fig 2.3 a-b the hydrodynamic volume distributions and the dynamic light scattering correlation curves for non-irradiated two commercial PVP variants, PVP K60 and PVP 1300000, are shown. Both polymers are highly polydisperse, with chains with a molecular weight between 1 and 800 kDa for PVP k60, and between 10 kDa and 2,000 kDa for PVP 1300000. Despite the high polydispersity evidenced by GFC (fig. 2.3a), the scattering light autocorrelation functions of both polymers (fig. 2.3b) are characterised by a single decay, therefore the hydrodynamic size distribution of the polymer chains can be described with a single average hydrodynamic diameter value (D_H) and a variation on this value that represents the width of the size distribution deriving from cumulant analysis. Indeed, the application of a stretched exponential function, that is generally used for highly polydisperse systems, yielded to a β (stretched exponential) of about 0.8 thus supporting the correctness of the approach. For PVP k60, D_H is 25±7 nm and for PVP 1300000 is 35±8 nm.

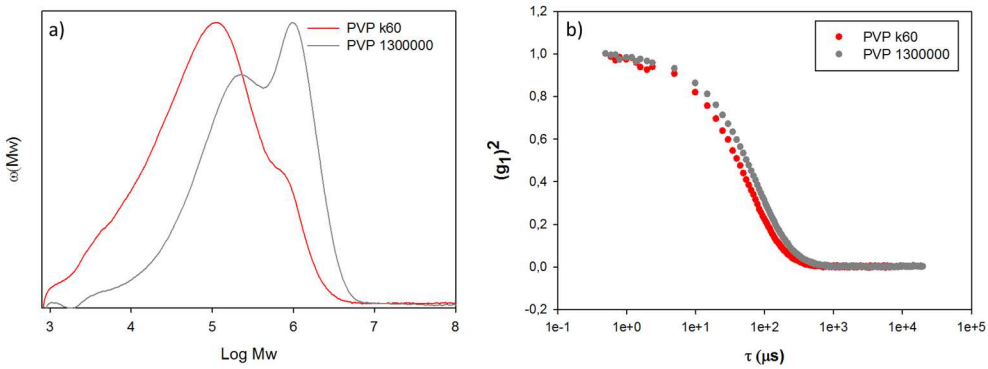

Figure 2.3. GFC Chromatograms (a) and autocorrelation function of the scattered light intensity (b) for non-irradiated PVP K60 and PVP 1300000.

All irradiated systems were optically transparent, except for the 0.5_HD system, that was heterogeneous (macrogel islands dispersed in an opalescent medium). 0.05_HD, 0.1_HD and 0.2_HD systems were characterized by a yellow coloration that increased in intensity with the dose. In Tab. 2.4 the average hydrodynamic diameter and width of the size distribution of selected LD-type systems and the corresponding non-irradiated PVP are reported.

Table 2.4. Average hydrodynamic diameter (D_H) and width of the size distribution of 0.05 wt% and 0.5 wt% LD irradiated systems and of the non-irradiated polymer.

Dose (kGy)	**D_H (nm)**	
	0.05_LD	0.5_LD
0	25±7	
2.4	23±8	43 ±14
3.6	22±6	53±16
4.8	25±9	67±20

For the 0.05 wt% PVP concentration, there is no dose effect on the hydrodynamic diameter, while for the 0.5 wt% PVP concentration D_H increases with dose, in good agreement with previous studies [3,12].

In Fig 2.4 a-b, the corresponding GFC curves are shown. For the 0.05_LD systems (Fig. 2.4a), the distributions of hydrodynamic volumes are slightly narrower than for the non-irradiated PVP. This phenomenon is even more evident at the higher doses and will be discussed later. For the 0.5_LD systems, a "migration" of objects from the smaller size (lower hydrodynamic volume) population to the bigger size (higher hydrodynamic volume) population with increasing the total absorbed dose is observed. For this polymer concentration and dose-range, inter-molecular combination seems to be the prevailing follow-up reaction of the formed macroradicals, affecting mainly the shorter chains.

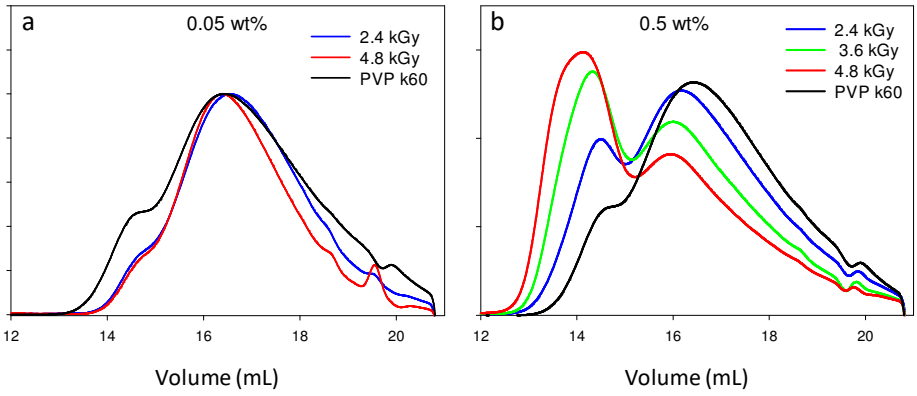

Figure 2.4 a-b Chromatographic profiles polymer solutions irradiated at 2.4, 3.6 and 4.8 kGy.: (a) 0.05 wt%; (b) 0.5 wt%. The chromatogram of the non-irradiated polymer is also included as reference.

The average hydrodynamic diameters and widths of size distribution for 0.05 wt%, 0.1 wt% and 0.2 wt% HD-type systems are reported in Table 2.5.

In particular, the D_H of 0.05_HD and 0.1_HD systems are all similar and smaller than for linear PVP; the 0.2_HD systems are close in size to the non-irradiated PVP and the 0.5 wt% corresponds to a situation where portions of the networks become macroscopic, therefore impossible to characterize by DLS and GPC.

Average weight molecular weight (Mw), determined from static light scattering measurements, showed no significant change for the 0.05 and 0.1 wt% systems with respect to the non-irradiated polymer, and a twofold increase with no dose effects for the 0.2 wt% systems. The increase of molecular weight of the nanogels when moving from dilute (C<<C*) to semi-dilute regime (C<C*) is a well known effect, resulting from a higher yield of intermolecular cross-linking when increasing polymer concentration. [11, 3] Insensitivity of both Mw and D_H from dose was observed by Kadublowski [11] above 6 kGy and by Dispenza et al. [3] in the 20-80 kGy dose range.

Indeed, inter-molecular crosslinking becomes less and less probable with dose/time, since the molar concentration of polymer/nanogel in solution is progressively reduced by the earlier intermolecular crosslinking events. Intra-molecular crosslinking is also less favoured with dose/time due the decrease of segmental mobility, because of the earlier intra-molecular crosslinking reactions that had occurred.

Table 2.5. Average hydrodynamic diameter (D_H) and width of the size distribution for 0.05 wt%, 0.1 wt% and 0.2 wt% HD irradiated systems and for the non-irradiated polymer.

Dose (kGy)	**D_H (nm)**		
	0.05_HD	0.1_HD	0.2_HD
0		35±8	
20	17±4	21±6	37±12
40	21±4	20±6	36±11
60	20±4	24±5	33±10
80	22±4	24±5	33±9

In Fig 2.5a-d the GFC chromatograms related to HD irradiated systems are reported. Accordingly to previous findings [3], for all the three concentrations investigated, the synthetic process allows a significant reduction in polydispersity with respect to the

linear polymer, with the disappearance of both the higher and lower hydrodynamic volume fractions, respectively. Expectedly, macroradicals formed on shorter chains (or smaller nanogel embryos) preferably combine intermolecularly, since they are fewer and with higher translational diffusivity. Contrariwise, macroradicals formed on longer chains (or bigger nanogel embryos) mainly combine intramolecularly, being more numerous and with lower translational diffusivity.

As shown in Fig 2.5 a-d, no influence of dose on the size distribution can be appreciated with the only exception of the 0.05 wt% that shows a fraction of short chains that increases with dose. This evidence suggests that at the higher doses and for the lower polymer concentrations, chain scission of loose polymer ends may become a competitive reaction. This reaction generates smaller fragments without impacting significantly on the polymer molecular weight distribution and on the average hydrodynamic diameter of the nanogels.

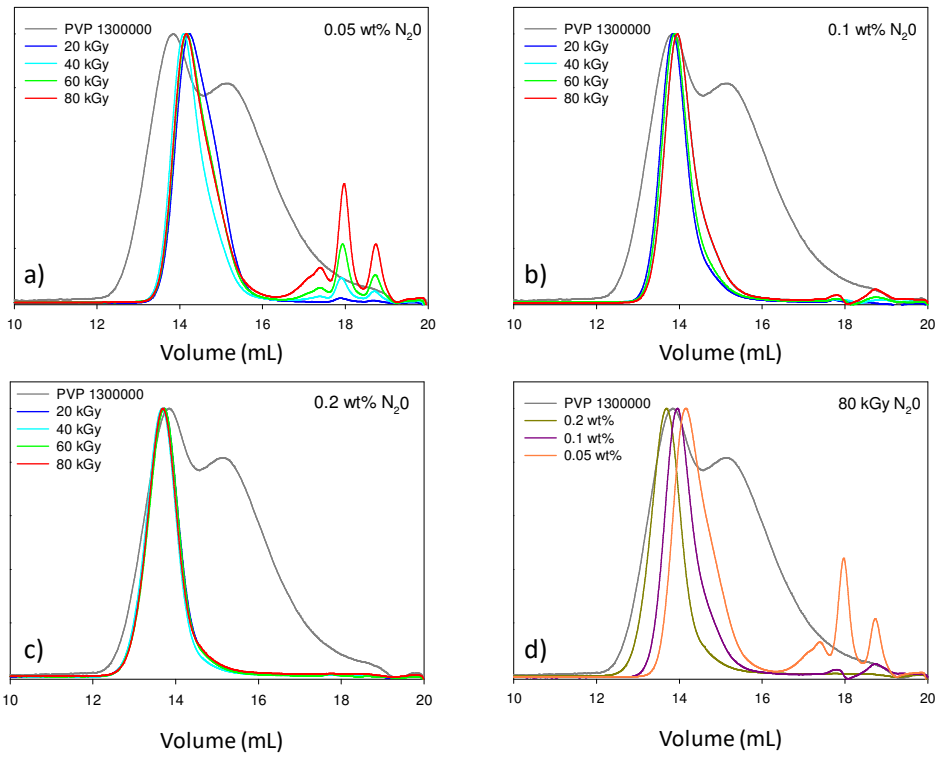

Figure 2.5. Chromatographic profiles of N_2O-saturated (a) 0.05 wt%, (b) 0.1 wt%, (c) 0.2 wt% polymer solutions irradiated at four total absorbed doses (20, 40, 60 and 80 kGy), (d) Comparison of the three systems irradiated at 80 kGy.

In order to confirm that the peaks were related to small fragments, GFC measurements were repeated on 0.05_HD 80 samples subjected to dialysis for 48h using either a 12 or 100 kDa cut-off membrane, against water. For the dialysed samples with both cut-offs, the peaks at high elution volumes have disappeared and the main peak is shifted to bigger hydrodynamic volumes (see Fig 2.6). The observed increase of hydrodynamic volumes upon dialysis is probably due to the pH increase (generally of one pH unit) and shift of protonation equilibria of the formed functional groups. [3].

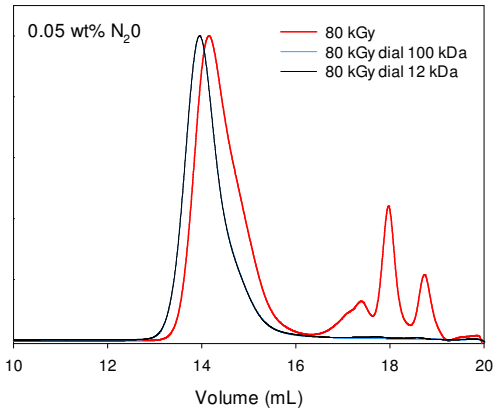

Figure 2.6. Chromatographic profiles of 0.05_HD 80, and 0.05_HD 80 dialysed with 12 or 100 kDa cut-off membranes.

In Fig. 2.5d, the GFC chromatograms related to three systems irradiated at 80 kGy are compared; the main peak is gradually shifted towards the higher hydrodynamic volumes still remaining within the linear polymer hydrodynamic volumes envelop.

2.3.2. Physico-chemical characterisation of poly(N-vinyl pyrrolidone)s irradiated as air-saturated aqueous solution

The influence of a different composition of the gaseous atmosphere above the polymer solution, air as opposite to N_2O, on hydrodynamic diameters and hydrodynamic volumes distribution was investigated for the HD systems at two concentrations, 0.05 and 0.5 wt%.

At a visual inspection, 0.05_HD_Air is colourless and perfectly transparent, while 0.5_HD_Air is slightly hazy, yet it was possible to analyse it with both DLS and GFC. In Tab. 2.6, the average hydrodynamic diameters and corresponding widths of the size distribution are reported. The total absorbed dose does not have an effect on the

average hydrodynamic diameter, as already observed for the N_2O-saturated systems (see Table 2.5).

From the GFC analysis, it is possible to appreciate a pronounced reduction of polydispersity for the 0.05_HD_Air and 0.5_HD_Air systems upon irradiation with respect to the non-irradiated polymer, similarly to the N_2O-saturated systems.

The influence of polymer concentration is also the same as for the N_2O-saturated systems: the higher is the polymer concentration the higher is hydrodynamic size (see Tab. 2.6 and Fig. 2.7).

Table 2.6. Average hydrodynamic diameter (D_H) and width of the size distribution of non-irradiated PVP, 0.05_HD_Air and 0.5_HD_Air systems.

Dose (kGy)	**D_H (nm)**	
	0.05_HD_Air	0.5_HD_Air
0	35±8	
20	9.6±3.2	109±33
40	10±3	107±28
60	9.9±3	106±28
80	9.8±3	106±27

The presence of oxygen from the beginning of the irradiation treatment has a strong effect on the final hydrodynamic diameter. Indeed, the 0.05_HD_Air system is characterized by smaller D_H than its N_2O-saturated analogue. The same effect was observed for 0.5_HD_Air system, being sized ca. 100 nm as opposite to the macrogels islands obtained for N_2O-saturated solutions. This evidence is confirmed by comparing the Log Mw curves, obtained using Pullulan standards solutions, for the 0.05 wt% irradiated at 20 and 80 kGy, as shown in Fig 2.8 a-b. Air-saturated systems are characterized by lower molecular weights and narrower distributions than their N_2O-saturated analogues. Interestingly, at 80 kGy, the peaks related to low molecular weight chains are present in both systems but the area under these peaks for 0.05_HD 80 is considerably smaller than for 0.05_HD 80_Air. We could conclude that air-

saturated systems are affected by chain scission in the very early stage of the process, when the polymer chains are not yet crosslinked and scission reactions may cleave backbone bonds with significant effects on molecular weights. They seem to become less affected by chain scission reactions than the N_2O saturated systems with increasing dose.

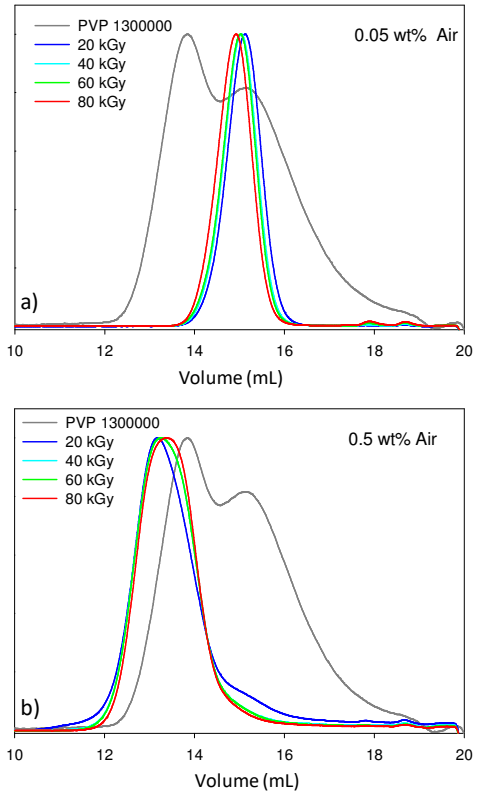

Figure 2.7. Chromatographic profiles of air-saturated (a) 0.05 wt%, (b) 0.5 wt% polymer solutions irradiated at four total absorbed doses (20, 40, 60 and 80 kGy) in HD-conditions.

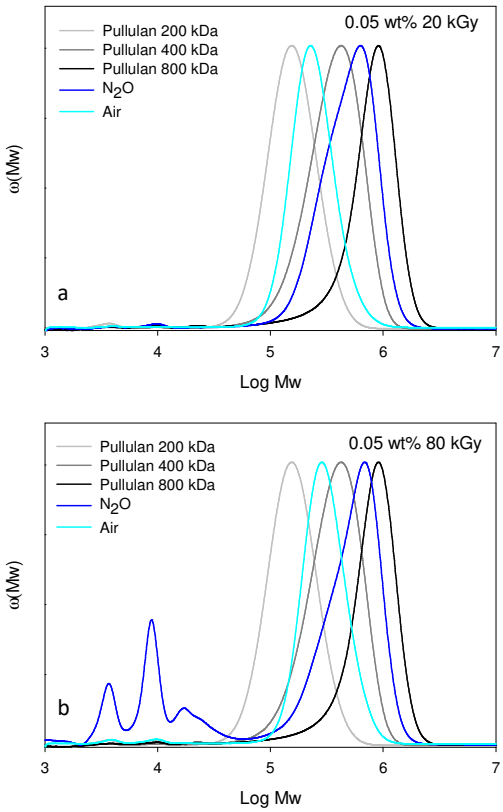

Figure 2.8. Molecular weight distributions for air- and N_2O-saturated 0.05_HD systems irradiated with (a) 20 kGy and (b) 80 kGy. Pullulan standard solutions are shown as reference.

2.3.3 H_2O_2 production in N_2O-saturated systems

The H_2O_2 concentration build-up in the various irradiated systems was experimentally measured using the Ghormley triiodide method. In particular, in the presence of the catalyst (AMT), H_2O_2 oxidizes I^- to I_3^-, which is quantified by UV-vis absorption spectroscopy at λ_{max} = 350 nm. All the measurements were conducted using the same concentration of KI (50 mM) and molybdenum-based catalyst.

For the measurements carried out on irradiated PVP aqueous solutions, the method will actually not distinguish between hydrogen peroxide and organic hydroperoxides that may have formed along the polymer chain. Therefore, although we need to be aware that attributing I_3^- formation only to H_2O_2 may lead to its overestimation, this does not necessarily mean that the polymer scavenging ability has been actually underestimated. Actually, we can speculate that H_2O_2 is formed but also consumed during irradiation, leading to the formation of molecular oxygen that is, in turn, involved in organic hydroperoxide formation. In conclusion, both H_2O_2 and organic hydroperoxides are the products of reactions that compete with hydrogen abstraction operated by hydroxyl radicals.

One further aspect related to the Ghormley triiodide method needs to be clarified. For the irradiated PVP systems, the absorbance at 350 nm rises very rapidly to its maximum value to slowly decrease over time. In Figure 2.9, the behaviour of the 0.1wt% PVP solution irradiated at 80 kGy (0.1_HD 80) is shown and compared to the behaviour of water irradiated in the same conditions and non-irradiated PVP (0.1 wt%) that was added of H_2O_2. Both for irradiated pure water and non-irradiated PVP/H_2O_2 systems, the absorbance at peak reaches rapidly a plateau and does not change with time.

The decay in absorbance is affected by polymer concentration (0.05 wt%) and dose of the irradiated system (see figures 2.10a-b). This suggests that in the irradiated systems containing PVP, a competitive and relatively slower reaction - that consumes part of the I_3^- formed by reaction between I^- and H_2O_2 - is occurring. A series of experiments and simulations were performed to identify the moiety responsible for this reaction and estimate its importance on the estimated H_2O_2 concentrations, which will be presented in the following.

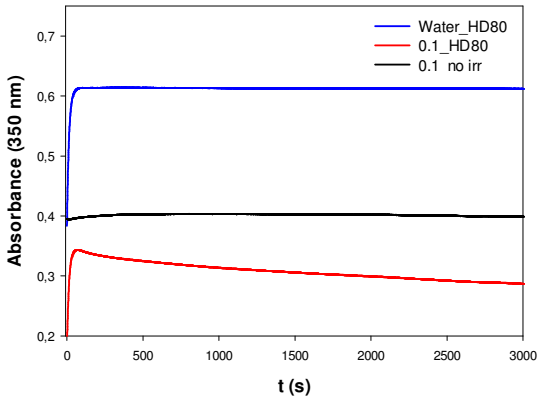

Figure 2.9. Time-course absorbance (350 nm) measurements for 0.1_HD80 systems, pure water irradiated with 80 kGy, and non-irradiated PVP (0.1 wt%) with added H_2O_2.

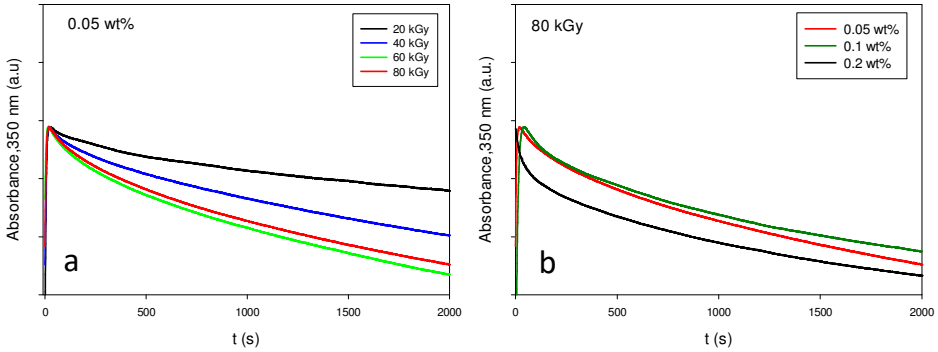

Figure 2.10. Time-course absorbance (350 nm) measurements (a) varying the dose; (b) varying the polymer concentration. Values have been shifted to the same value of absorbance at peak for ease of representation.

In the Table 2.7 and 2.8, the H_2O_2 concentrations (determined in correspondence to the highest measured value of absorbance at peak) are reported. H_2O_2 concentration for pure water, irradiated in the same conditions as the polymer solutions, is also included as reference. Data were also plotted in Fig. 2.11 a-b.

Tab. 2.7. H_2O_2 concentration for LD systems and for water irradiated in the same conditions.

Irradiated systems	Dose (kGy)	H_2O_2 (M)
Water	0.6	$9.02\ 10^{-5}$
	1.8	$1.30\ 10^{-4}$
	2.4	$1.73\ 10^{-4}$
	3.6	$2.00\ 10^{-4}$
	4.8	$2.02\ 10^{-4}$
0.05_LD	0.6	$5.92\ 10^{-5}$
	1.8	$9.31\ 10^{-5}$
	2.4	$1.78\ 10^{-4}$
	3.6	$8.21\ 10^{-5}$
	4.8	$7.28\ 10^{-5}$
0.5_LD	0.6	$2.38\ 10^{-5}$
	1.8	$4.16\ 10^{-5}$
	2.4	$5.49\ 10^{-5}$
	3.6	$9.90\ 10^{-5}$
	4.8	$6.85\ 10^{-5}$

Table 2.8. H_2O_2 concentration for the HD systems and for water irradiated in the same conditions.

Irradiated systems	Dose (kGy)	H_2O_2 (M)
Water	20	$1.78\ 10^{-3}$
	40	$1.85\ 10^{-3}$
	60	$2.02\ 10^{-3}$
	80	$2.13\ 10^{-3}$
0.05_HD	20	$9.07\ 10^{-4}$
	40	$1.05\ 10^{-3}$
	60	$8.67\ 10^{-4}$
	80	$7.32\ 10^{-4}$
0.1_HD	20	$8.22\ 10^{-4}$
	40	$6.63\ 10^{-4}$
	60	$5.31\ 10^{-4}$
	80	$5.50\ 10^{-4}$
0.2_HD	20	$3.24\ 10^{-4}$
	40	$3.40\ 10^{-4}$
	60	$2.54\ 10^{-4}$
	80	$2.71\ 10^{-4}$

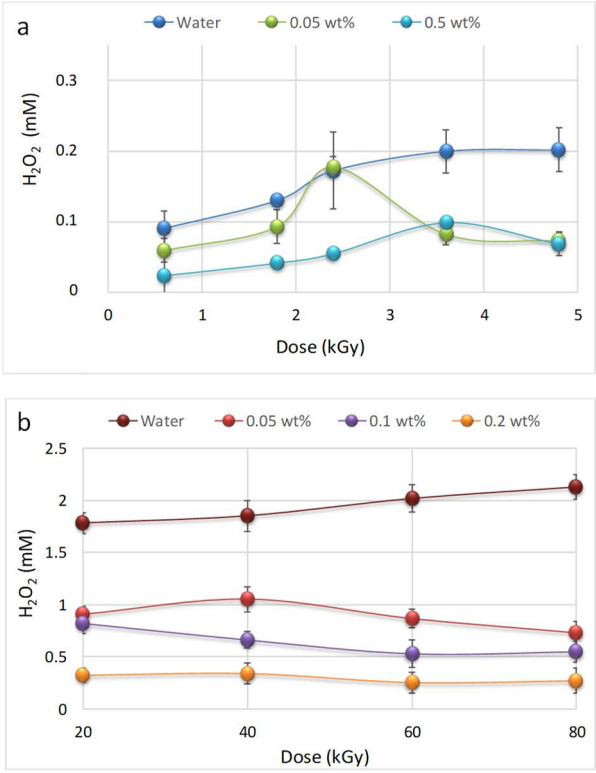

Figure 2.11 a-b. H_2O_2 build-up for LD systems (a) and HD systems (b) as function of the dose. Pure water irradiated in the same conditions is also reported for comparison.

The main observations are the following: measurable amounts of H_2O_2 are detected in all irradiated systems; the lower is the polymer concentration the higher is the H_2O_2 concentration; the higher is the dose the higher is H_2O_2 concentration, when comparing LD and HD systems.

2.3.4 Investigation of possible causes of I_3^- consumption over time in the irradiated polymer solutions

In order to understand which moiety in the system is responsible for the observed I_3^- consumption in samples subjected to the Ghormley triiodide method, various molecules with different functional groups, which could be possibly formed in PVP upon irradiation, were mixed with I_3^- (25 μM). In particular, primary or secondary amino groups-, carboxyl groups-, hydroxyl groups- and aldehyde groups-carrying molecules, 1-vinyl 2-pyrrolidone (VP), poly(N-vinyl pyrrolidone) and poly carboxylic acid (PAA) were tested. Progressive increasing amounts of each of these species (corresponding to concentrations in the 10-200 μM range) were added to the solution of I_3^- and, after each addition, the absorbance spectrum of the solution was measured. Among all the tested molecules and polymers, only VP caused a decrease in I_3^- absorbance (after correction for dilution) and for this reason, the reaction of VP with I_3^- was further investigated.

Known volumes of VP were progressively added to the solution of known concentration of I_3^- and, after each addition, the full absorbance spectrum was measured, as shown in Fig. 2.12a. For each system, the spectrum was acquired immediately and 15 minutes after VP addition; no changes in the spectrum were detected.

As a result, considering that non-irradiated PVP does not cause any change in I_3^- absorbance while VP does, we concluded that the double bonds of the vinyl monomer were the functional groups formed upon irradiation in the PVP networks most likely involved in the reaction with I_3^-. A calibration curve was built by plotting the variation in absorbance (ΔAbs, λ= 350 nm) as a function of VP concentration (1.5 -14 μM), where ΔAbs was calculated as ΔAbs = Abs (I_3^-, 25 μM) – Abs (after VP addition), as shown in Fig 2.12b. A molar extinction coefficient of 26.7 x 10^3 M^{-1} cm^{-1} was estimated.

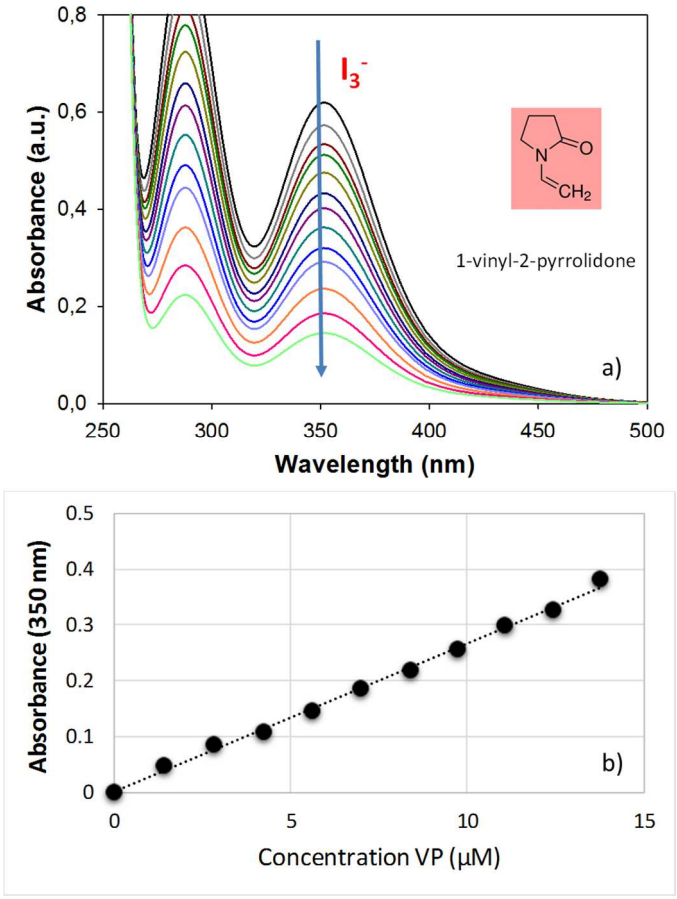

Fig 2.12. (a) UV-vis absorbance spectra of I_3^- solutions at various VP concentrations in the system. (b) Calibration curve of absorbance decay vs. VP concentration.

In Fig. 2.13 the concentrations of I_3^- and double bonds calculated using the molar extinction coefficients of Fig. 2.2 and 2.12, respectively, for the same values of absorbance at 350 nm are plotted. These values differ for less than 5%. Therefore, a 1:1 stoichiometric ratio between I_3^- and double bonds can be assumed.

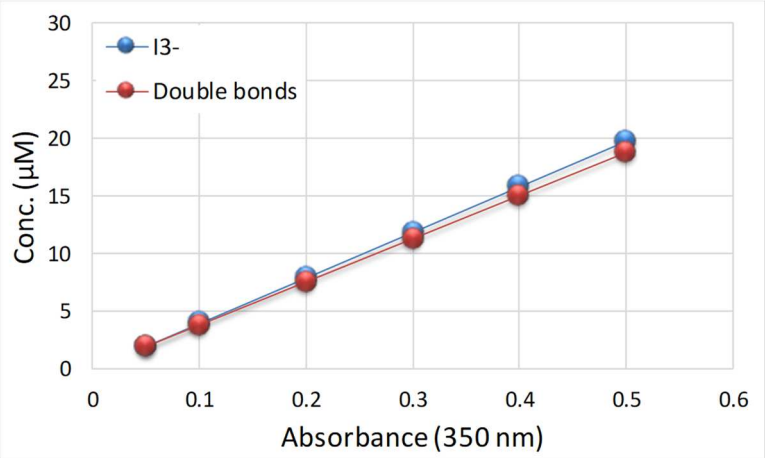

Fig. 2.13. Comparison between the calculated concentrations of I_3^- and double bonds from their respectively molar extinction coefficients.

In order to quantify the effect of the concurrent reaction between I_3^- and double bonds on the estimation of H_2O_2 concentration, the reaction rate constants (k_p and k_c) of the two reactions (I_3^- production vs I_3^- consumption) were determined. KI in large excess, AMT and H_2O_2 (6 µM in the final volume) were mixed with known volumes of VP in order to have concentrations of 6, 8, 10 and 12 µM in the final volume. After each addition a measurement of the time-course absorbance at λ= 350 nm was performed. From the curve obtained after the first addition, in the hypothesis of a pseudo-first order reaction of the reaction between I^- and H_2O_2 a $t_{1/2}$ (t of half-life) of 7.2 seconds was determined, corresponding to $k_p = 9.63\ 10^{-2}\ s^{-1}$ (or $1.95\ M^{-1}\ s^{-1}$, taking into account the initial concentration of I^- in the systems) was calculated.

From the decays obtained from the measurements after the subsequent VP additions, k_c was calculated. In fact, solving the kinetic equation (Eq. 2.3), where "a" and "b" are the molar concentrations of I_3^- and VP respectively, for each I_3^- - VP concentration, an average rate constant, $k_c = 4.0 * 10^3\ M^{-1}s^{-1}$ was determined.

Eq. 2.3 $$ln\frac{a-x}{b-x} + ln\frac{b}{a} = kt(a-b)$$

These rate constants will be used to qualitatively evaluate the impact of double bonds on the quantitative analysis of H_2O_2 by I_3^- (see par 2.3.8)

2.3.5 H_2O_2 production in air-saturated systems

The H_2O_2 concentration values that correspond to highest measured absorbance value for LD irradiated systems are reported in Tab. 2.9 and Figure 2.14. For pure water H_2O_2 concentration increases with dose, while an opposite trend was detected for the PVP irradiated systems. Moreover, differently from the N_2O-saturated systems, the air-saturated systems do not show any effect of polymer concentration on the formation of H_2O_2. These results will be discussed in next paragraph in the light of the numerical simulations.

For the HD systems, in Tab 2.10 only the H_2O_2 concentration values related to air-saturated water are reported, since for all the PVP-based HD systems no detectable amount of I_3^- was found. This result is not surprising since the concentration of H_2O_2 produced in pure water was already 70% lower than in N_2O-saturated water and we might have consumption of I_3^- by double bonds.

Table 2.9. H_2O_2 molar concentration as function of total absorbed dose for air-saturated water, 0.05_LD and 0.5_LD systems.

Systems	Dose (kGy)	H_2O_2 (M)
Water_Air	0.6	$1.06\ 10^{-4}$
	1.8	$1.30\ 10^{-4}$
	2.4	$1.42\ 10^{-4}$
	3.6	$1.74\ 10^{-4}$
	4.8	$1.85\ 10^{-4}$
0.05_LD_Air	0.6	$6.04\ 10^{-5}$
	1.8	$4.00\ 10^{-5}$
	2.4	$2.04\ 10^{-5}$
	3.6	$1.72\ 10^{-5}$
	4.8	$2.00\ 10^{-5}$
0.5_LD_Air	0.6	$5.80\ 10^{-5}$
	1.8	$2.84\ 10^{-5}$
	2.4	$2.08\ 10^{-5}$
	3.6	$1.52\ 10^{-5}$
	4.8	$1.72\ 10^{-5}$

Table 2.10. H_2O_2 molar concentration as function of total absorbed dose for air-saturated water irradiated under HD conditions.

Systems	Dose (kGy)	H_2O_2 (M)
Water_Air	20	$4.09\ 10^{-4}$
	40	$5.10\ 10^{-4}$
	60	$5.51\ 10^{-4}$
	80	$5.93\ 10^{-4}$

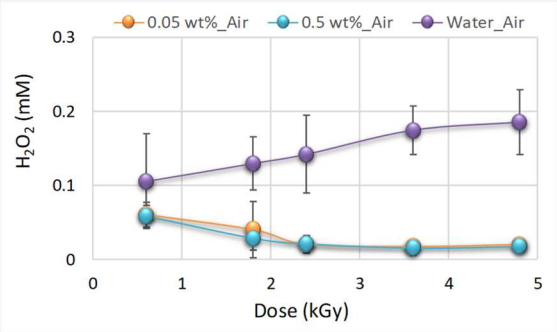

Figure 2.14. H_2O_2 production in air-saturated LD systems.

A comparison between N_2O- and air-saturated irradiated PVP systems is shown in Fig. 2.15a-b. Except for 0.6 kGy, a higher amount of H_2O_2 was always produced in N_2O-saturated systems.

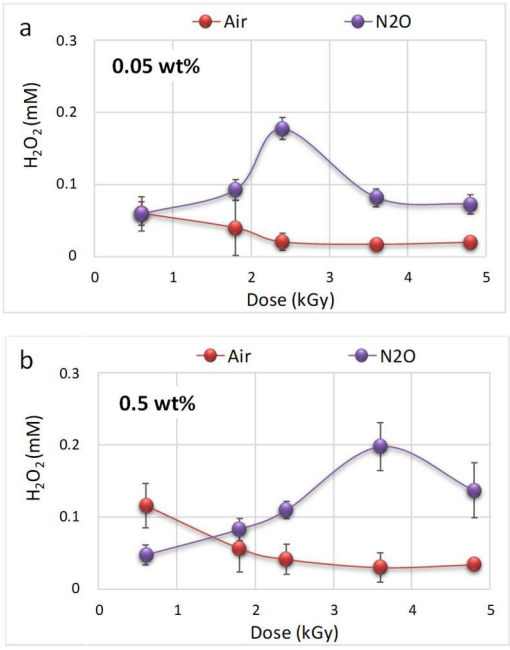

Figure 2.15. Comparison of H_2O_2 produced in air- and N_2O-saturated 0.05wt% (a) 0.5wt% LD systems (b).

2.3.6 Numerical analysis of the radiation chemistry of aqueous solutions exposed to pulsed electron beams

In order to capture the most relevant differences in the two irradiation set-ups and various irradiation conditions used for the experimental studies described above, a numerical code was developed to simulate the radiation chemistry of aqueous solutions exposed to pulsed e-beams for the specific pulse sequences and dose rates during the pulse used in the two experimental set-ups described above.

In a first set of simulations, the production of H_2O_2 was studied as a function of dose for N_2O- and air-saturated water. The simulations generated data for all reactants and products as a function of dose/irradiation time. In particular, we focused our attention on H_2O_2 and O_2 build-up. In a second set of simulations the impact of the presence of a hydroxyl radical scavenger on H_2O_2 and O_2 build-up was studied. The concentration of the molecular scavenger in the system was "locked" to mimic the large number of abstractable hydrogen atoms of the polymer. The scavenger initial concentration was systematically varied until we could obtain a H_2O_2 profile similar to the experimental one obtained for the lowest polymer concentration. Then, the initial concentration of the scavenger was increased with respect to that value, with the same ratios of the polymer weight concentration in the experiments.

The H_2O_2 profiles obtained are presented in Fig 2.16 a-b and 2.17 a-b for the LD and HD conditions, respectively. The simulations are in fairly good agreement with the experimental results, both for the LD and the HD irradiation conditions.

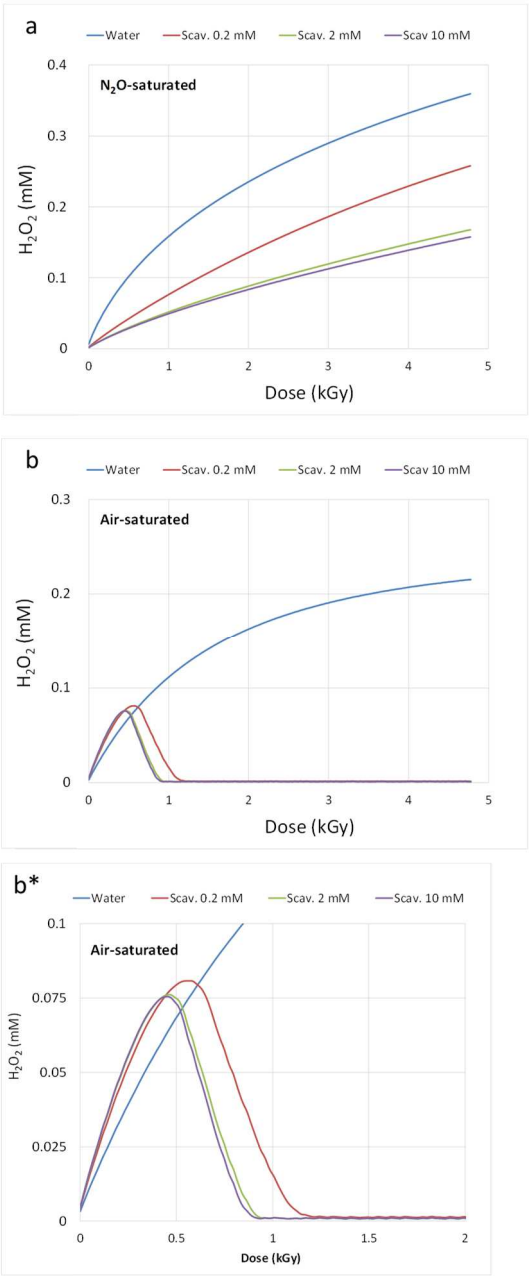

Figure 2.16. H_2O_2 profiles determined from the numerical simulations (a) N_2O- and (b and b*) air-saturated LD systems.

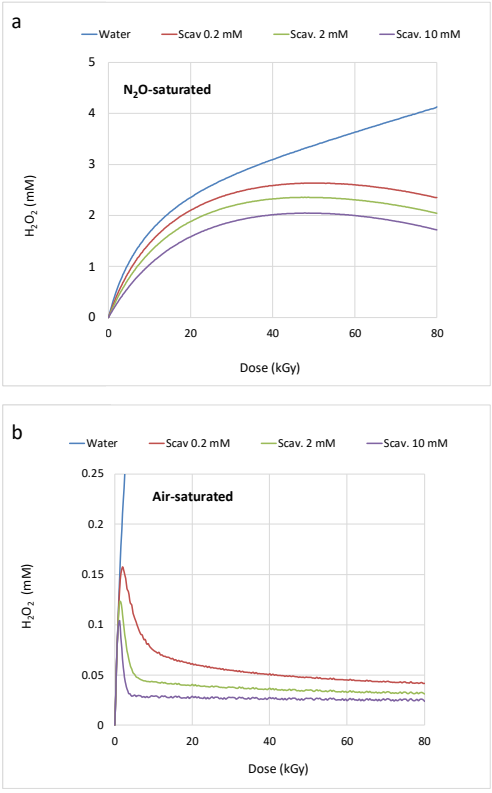

Figure 2.17. H_2O_2 profiles determined from the numerical simulations (a) N_2O- and (b) air-saturated HD systems.

It is interesting to observe that for the air-saturated HD systems, that did not show detectable amounts of H_2O_2, the simulation predicts fairly low concentrations of produced H_2O_2 (10^{-5} M) for the dose of 20 kGy and higher, while the experimentally determined concentration of double bonds is one order of magnitude higher, thus explaining the impossibility to experimentally detect H_2O_2 with the Ghormley triiodide method. As molecular oxygen is a potentially important reactant, we also plot the calculated O_2-concentrations from the simulations (Fig. 2.18 a-b). It can be noticed that all systems appear to become almost O_2-free within a relatively short time in the presence of the hydroxyl radical scavenger. However, it should be pointed out

that the O_2-concentration is several orders of magnitude higher in the N_2O-saturated systems compared to the air-saturated systems (μM compared to nM) (Fig. 2.18* a-b). Furthermore, since in pure water, and particularly for the N_2O-saturated water, O_2 reaches millimolar concentrations at higher doses, we expect that a significant amount of O_2 (theoretically all of it) can react with the organic substrate (the polymer). This can provide some important hints for the elaboration of the reaction mechanisms that explain the observed chemical modifications of the PVP structure.

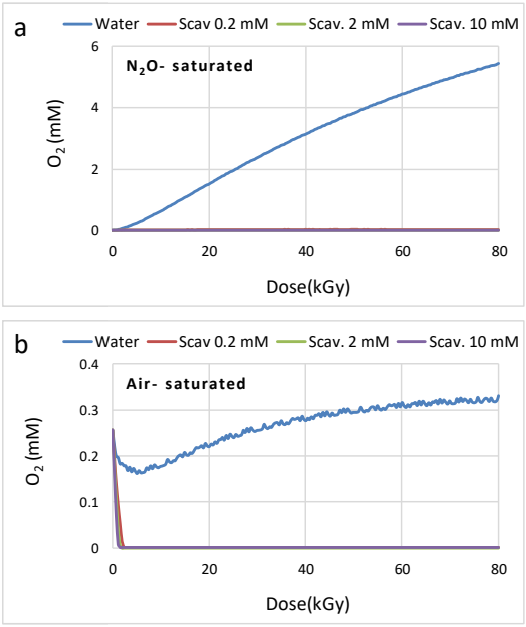

Figure 2.18. O_2 profiles determined from the numerical simulations for (a) N_2O- and (b) air-saturated HD systems.

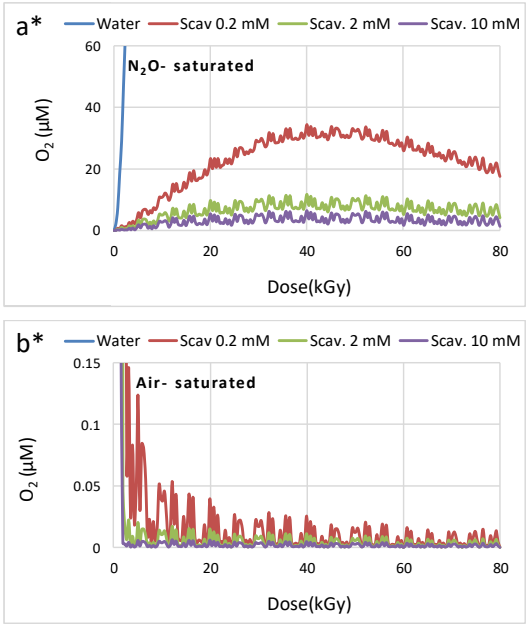

Figure 2.18*. y-axes enlargement of Fig. 2.18 (a-b): O_2 profiles determined from the numerical simulations for (a*) N_2O- and (b*) air-saturated HD systems.

2.3.7 Experimental study of functional groups modification in irradiated aqueous poly(N-vinyl pyrrolidone)s

Chemical modifications of PVP occurring upon irradiation were evaluated by FTIR analysis and colorimetric titrations. In this work, differently from previous investigations carried out by our research groups [2,3], the study of chemical functionalities modification has been performed on the whole system and not on the purified nanogels since is aimed to evaluate the overall changes occurring in the systems.

FTIR analysis

FTIR analysis was carried out for 0.05 wt% and 0.5 wt% PVP solutions irradiated in the HD-type irradiation conditions at the two extreme doses (20 and 80 kGy) of the investigated range, in both N_2O- and air-saturated conditions.

FTIR spectra of 0.05_HD irradiated at 20 and 80 kGy are shown in Fig 2.19 a-b. The broad absorption in the region 3600-3200 cm^{-1} is associated to the overlapping contributions of O-H stretching vibrations, related to residual free and bound water (ca. 3600-3500 cm^{-1}) and polymeric hydroxyl groups (3400-3200 cm^{-1}), and to free and associated N-H stretching vibrations of primary and secondary amines (3500-3300 cm^{-1}). The 0.05_HD 20 system shows an increase of the hydroxyl groups absorption band, while 0.05_HD 80 is characterized by the enlargement of this band towards lower wavenumbers, with possible contributions from C-H stretch vibrations of double bonds (3100-3000 cm-1), hydroxyl to carbonyl coupling vibrations (3200-2500 cm^{-1}) and νN^{+}-H of ammonium compounds (3000-2250 cm^{-1}). A decrease of the methylene band (2956 cm^{-1}) can be observed. Magnification of the spectra in 2000-500 cm^{-1} wavenumbers region (Fig 2.19b) evidences the modification of the carbonyl group vibration band. For the non-irradiated polymer, the band is essentially due to the absorption of the carbonyl group of the pyrrolidone moiety (1660 cm^{-1}). The 0.05_HD 20 system shows an increase of absorbance of this peak and two shoulders at 1769 and 1698 cm^{-1}, ascribable to the C=O symmetric and asymmetric stretching vibrations of a 5-members cyclic imide, respectively. These spectral modifications may suggest a consumption of part of the methylene groups (that contribute to the increase of both the hydroxyl and the pyrrolidone carbonyl groups bands) and the transformation of some pyrrolidone groups into imide groups. The 0.05_HD 80 shows a decrease of the pyrrolidone carbonyl absorbance and a more significant enlargement of the carbonyl band towards higher wavenumbers, which suggest the presence of cyclic imides and carboxylic groups. In both irradiated systems a new band at 1540 cm^{-1}, associated to δN-H and δN^{+}-H, is visible. This band increases with dose. The presence of double bonds is also supported by the presence of the peaks at 1415 and

721 cm^{-1} attributable to in plane and out of plane δC-H vibrations, respectively. Carboxylate anions seem to revealed by the peak at 1400 cm^{-1} and the enlargement of the carbonyl band towards the lower wavenumbers.

In Fig 2.20 the full spectra (4000–500 cm^{-1}) and its enlargement (2000-400 cm^{-1}) of the 0.5_HD systems irradiated at 20 and 80 kGy and of the non-irradiated PVP are shown. For these systems the spectral modifications with respect to non-irradiated PVP are essentially an increase in the absorbance of hydroxyl and amino groups in the high wavenumbers range, and an increase of 1660 cm^{-1} band (C=O of pyrrolidone). These changes occur almost to the same extent in both systems. In the 0.05_HD 80 system only, new small bands at 1769, 1698 cm^{-1} (imides) and 1540 cm^{-1} (δN-H and δN^{+}-H) are also present.

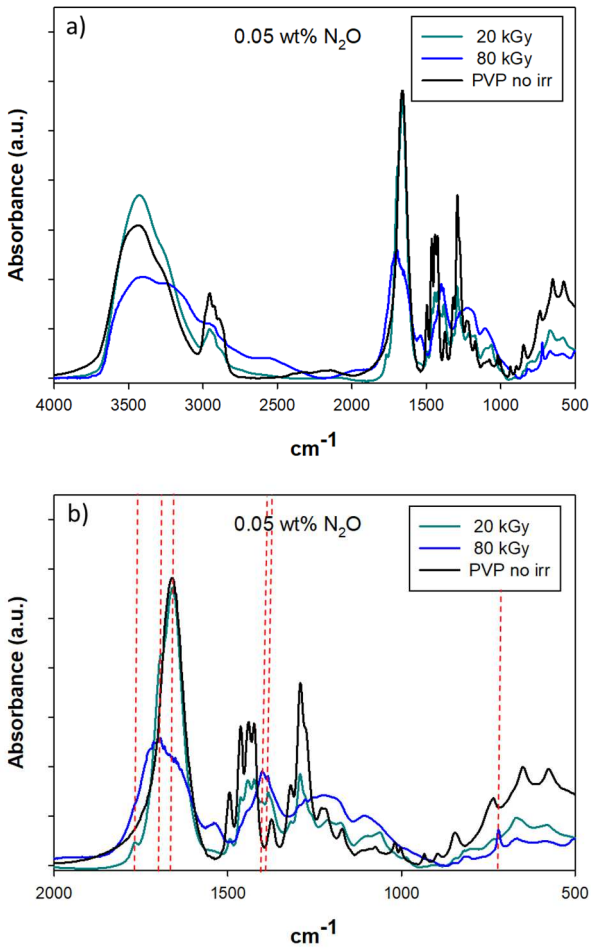

Figure 2.19. FTIR spectra of N_2O-saturated 0.05_HD systems irradiated with 20 and 80 kGy and non-irradiated PVP: (a) full spectrum; (b) enlargement of the 2000 cm^{-1} – 500 cm^{-1} wavenumber region.

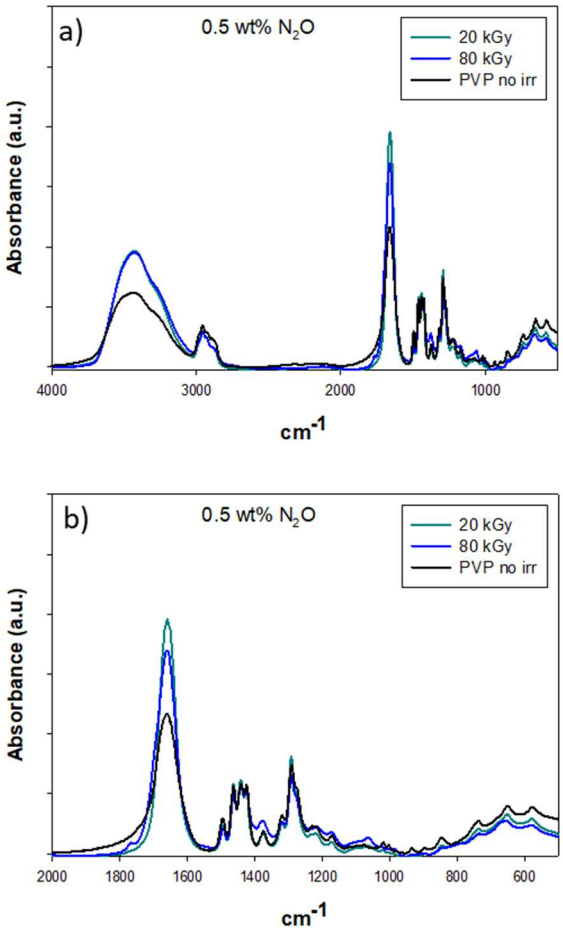

Figure 2.20. FTIR spectra of 0.5_HD N_2O-saturated systems irradiated with 20 and 80 kGy and non-irradiated PVP (a) full spectrum; (b) enlargement of the 2000 cm^{-1} – 450 cm^{-1} wavenumber region.

The FTIR spectra of the air-saturated 0.05 and 0.5 wt% systems irradiated at 20 and 80 kGy are shown in Fig. 2.21a-b and 2.22a-b. While the 0.5 wt% systems appear rather unmodified, for the 0.05 wt% systems there is (i) a slight enlargement of the

3800-3500 cm^{-1} band towards the lower wavenumbers; (ii) the attenuation of the methylene absorption band at 2956 cm^{-1}; (iii) the appearance of spectral features of the cyclic imide in the carbonyl group envelop; and (iv) of the band at 1400 cm^{-1} attributable to out of plane bending C-H vibrations of double bonds. These features are the more evident the higher is the dose.

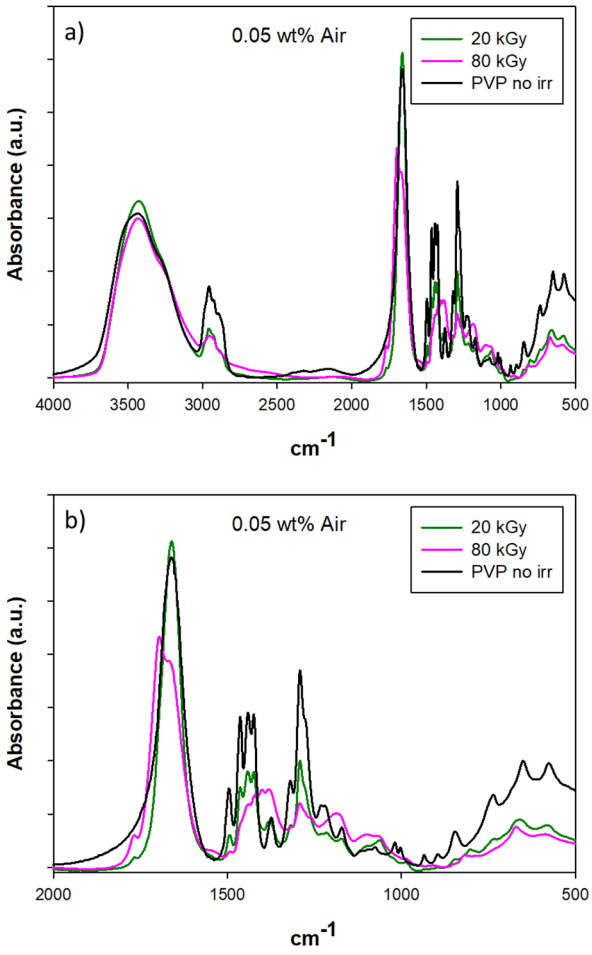

Figure 2.21. (a) FTIR spectra of air-saturated 0.05_HD systems irradiated at 20 and 80 kGy and of non-irradiated PVP; (b) Magnification of the 1900-600 cm^{-1} wavenumber region.

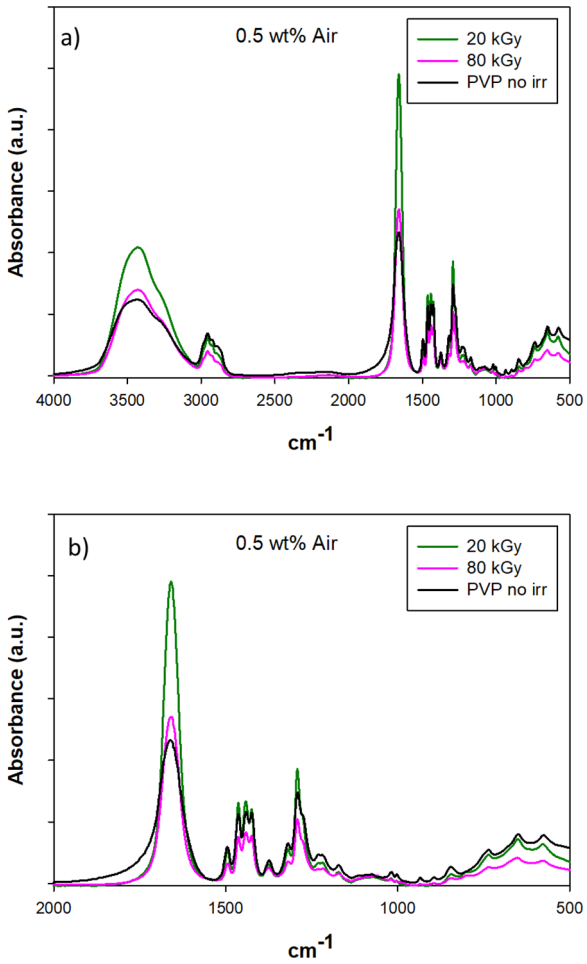

Figure 2.22. (a) FTIR spectra of air-saturated 0.5_HD systems irradiated at 20 and 80 kGy and of non-irradiated PVP; (b) Magnification in the 1900-600 cm^{-1} wavenumber region.

In Fig 2.23 a-b the comparison between the air-saturated and N_2O-saturated 0.05 wt% systems irradiated at the two doses is reported. In general, N_2O-saturation leads to a more marked spectral modification of the irradiated PVP, especially at high dose.

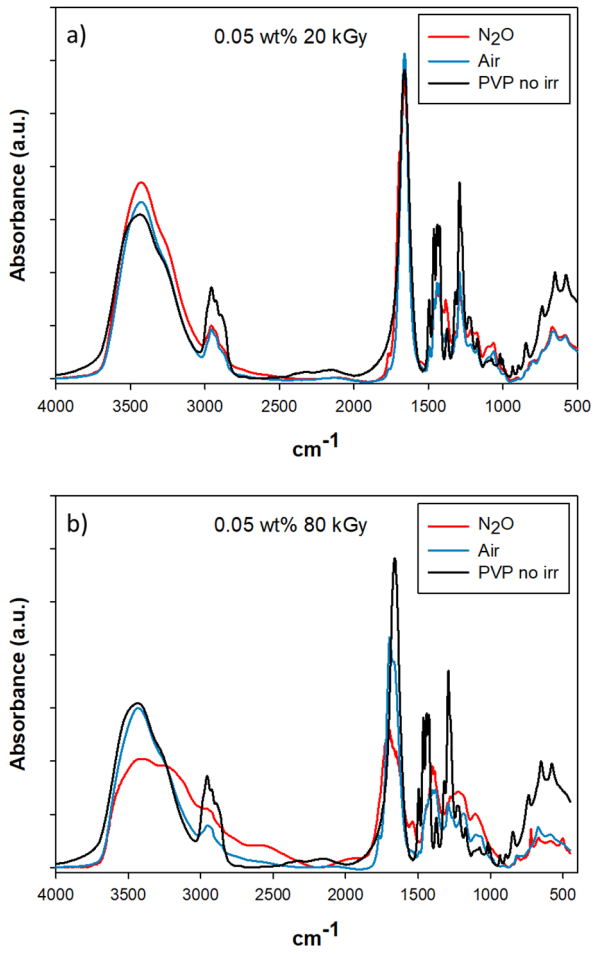

Figure 2.23. FTIR spectra of N_2O- and air-saturated 0.05_HD systems irradiated at 20 kGy (a) and 80 kGy (b). Non-irradiated PVP is reported as reference.

Double bonds

In the light of the findings described in par 2.3.4, the Ghormley triiodide method was applied to estimate the concentration of double bonds in the irradiated polymers. In particular, the double bonds were determined by the amount of reacted I_3^-, calculated from the difference between the sum of the I_3^- produced in the system by reaction of

KI and a purposed added amount of H_2O_2 and the I_3^- produced by H_2O_2 already present in the system (produced upon irradiation) and the residual I_3^-, measured when the absorbance at 350 nm reaches a plateau.

The double bonds present in N_2O-saturated, LD and HD systems are reported in Tab. 2.11 and 2.12, respectively, and plotted as function of dose in Fig. 2.24 a-b. In all the irradiation conditions, the concentration of double bonds increases with dose. For LD systems, the double bond concentration increases also with polymer concentration. The same trend cannot be appreciated for the HD systems. It should be emphasised that the double bonds measured are the residual amount resulting from their formation through disproportionation and chain scission reactions and their consumption, e.g. by addition reactions involving the various radical species formed during irradiation. The air-saturated systems show a similar trend for the low dose range, with double bonds concentration increasing with dose and polymer concentration (see Tab. 2.13 and 2.14 and Fig. 2.25 a). For the high dose range, at higher polymer concentration the double bond concentration decreases with dose, while is almost invariant with dose for the lower polymer concentration (see Tab. 2.14 and Fig. 2.25 b).

In Fig. 2.26, the comparison between N_2O- and air-saturated 0.05 wt% systems in the whole dose range is shown. Interestingly, despite of the differences in the e-beam set-up parameters the values that refer to the low dose range and the high dose range nicely connect. Furthermore, the values for the N_2O-saturated conditions are approximately twice as higher than those for the air-saturated conditions, which is also the difference in the G value for hydroxyl radicals in N_2O and air-saturated conditions.

Table 2.11. Double bonds in N_2O-saturated LD-systems expressed as molar concentration in the system and mole of double bonds per mole of PVP repeating unit (%)

System	Dose (kGy)	-C=C- (M)	-C=C- /PVP RU (%)
0.05_LD	0.6	$2.30\ 10^{-5}$	0.50
	1.8	$3.15\ 10^{-5}$	0.70
	2.4	$4.42\ 10^{-5}$	0.97
	3.6	$4.29\ 10^{-5}$	0.94
	4.8	$5.94\ 10^{-5}$	1.30
0.5_LD	0.6	$5.39\ 10^{-5}$	0.12
	1.8	$1.12\ 10^{-4}$	0.25
	2.4	$1.22\ 10^{-4}$	0.27
	3.6	$1.63\ 10^{-4}$	0.36
	4.8	$1.84\ 10^{-4}$	0.40

Table 2.12. Double bonds in N_2O-saturated HD systems expressed as molar concentration in the system and mole of double bonds per mole of PVP repeating unit (%)

System	Dose (kGy)	-C=C- (M)	-C=C-/PVP RU (%)
0.05_HD	20	$1.12\ 10^{-4}$	2.50
	40	$1.77\ \ 10^{-4}$	3.90
	80	$2.14\ 10^{-4}$	4.70
0.1_HD	20	$1.23\ 10^{-4}$	1.35
	40	$1.62\ 10^{-4}$	1.80
	80	$2.37\ 10^{-4}$	2.60
0.2_HD	20	$7.68\ 10^{-4}$	0.42
	40	$1.63\ 10^{-4}$	0.90
	80	$2.46\ 10^{-4}$	1.35

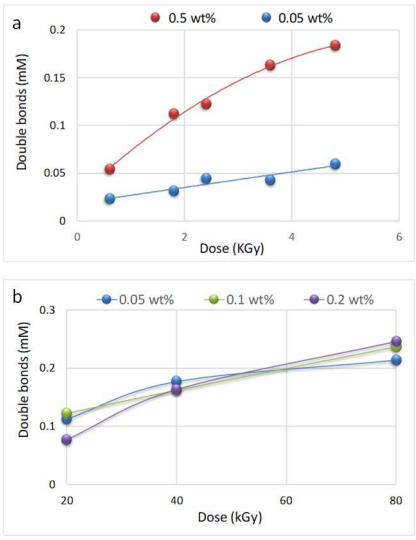

Figure 2.24. Double bonds as function of the irradiation dose in N_2O-saturated systems: (a) LD systems; (b) HD systems.

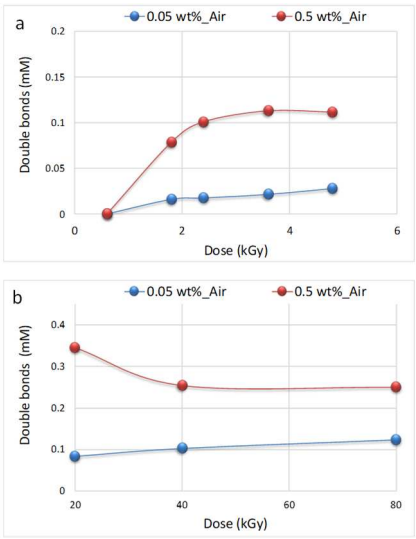

Figure 2.25 Double bonds as function of the irradiation dose produced in air-saturated (a) LD-systems and (b) HD-systems.

Table 2.13 Double bonds in air-saturated LD-systems expressed as molar concentration in the system and mole of double bonds per mole of PVP repeating unit (%)

System	Dose (kGy)	-C=C- (M)	-C=C- /PVP RU (%)
0.05_LD Air	0.6	0.0	0
	1.8	$1.62\ 10^{-5}$	0.36
	2.4	$1.77\ 10^{-5}$	0.39
	3.6	$2.17\ 10^{-5}$	0.48
	4.8	$2.82\ 10^{-5}$	0.62
0.5_LD Air	0.6	0.0	0
	1.8	$7.86\ 10^{-5}$	0.17
	2.4	$1.01\ 10^{-4}$	0.22
	3.6	$1.13\ 10^{-4}$	0.25
	4.8	$1.11\ 10^{-4}$	0.25

Table 2.14 Double bonds in air-saturated HD-systems expressed as molar concentration in the system and mole of double bonds per mole of PVP repeating unit (%)

System	Dose (kGy)	-C=C- (M)	-C=C-/PVP RU (%)
0.05_HD Air	20	$8.43\ 10^{-5}$	1.9
	40	$1.03\ 10^{-4}$	2.3
	80	$1.24\ 10^{-4}$	2.7
0.5_HD Air	20	$3.45\ 10^{-4}$	0.76
	40	$2.54\ 10^{-4}$	0.56
	80	$2.50\ 10^{-4}$	0.55

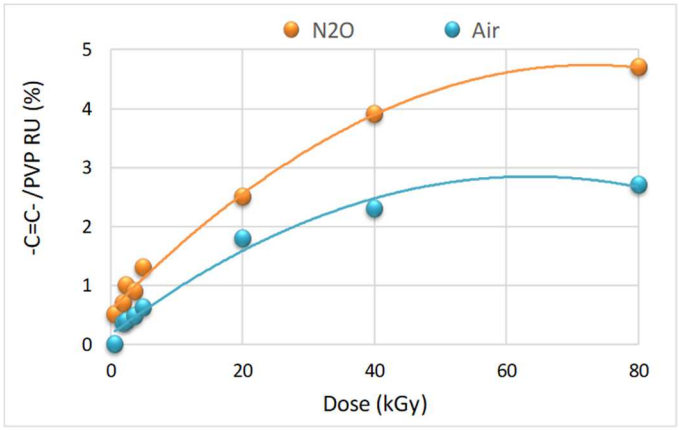

Figure 2.26. Comparison of number of double bonds per PVP RU formed in N_2O- and air-saturated 0.05 wt% irradiated systems (LD and HD systems).

The lack of linear dependence of double bond concentration from dose, in the whole range of investigated doses, makes meaningless the determination of their G-values.

Carboxyl groups and primary amino groups

The estimation of carboxyl groups was performed via a colorimetric titration method based on their ability to complex Nickel cations. Since this complexation requires between two and three carboxyl groups per Nickel ion, the method is not able to detect isolated carboxyl groups. Primary amino groups were estimated via formation of their fluorescent adduct with fluorescamine (λ_{exc}=391nm, λ_{em}=481nm).

For the LD irradiation conditions, no carboxyl groups were detected. The concentration of amino groups for N_2O-saturated systems is reported in Table 2.15 and Figure 2.27. This concentration is one order of magnitude lower than the concentration of double bonds in the system for the same dose and polymer concentration. It increases with dose and polymer concentration, similarly to the concentration of double bonds.

Table 2.15. Concentration of primary amino groups (–NH_2) in N_2O-saturated LD systems.

Dose (kGy)	-NH_2 (M)	
	0.05_LD	0.5_LD
2.4	1.79 10^{-6}	1.03 10^{-5}
3.6	4.33 10^{-6}	1.26 10^{-5}
4.8	6.09 10^{-6}	1.88 10^{-5}

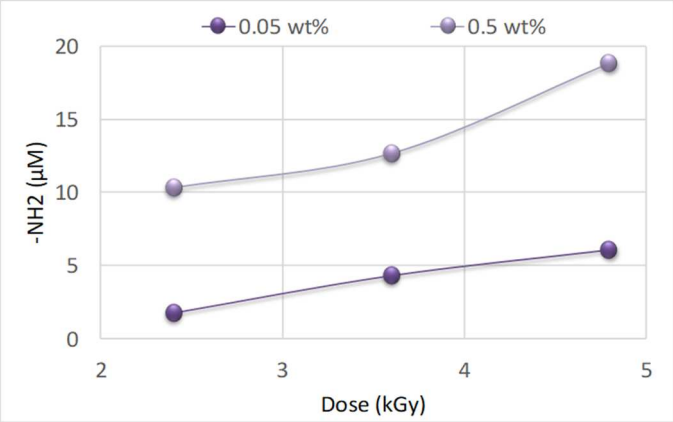

Figure 2.27. Primary amino groups (-NH_2) in N_2O-saturated LD systems on varying the total absorbed dose.

Carboxyl groups and the amino group concentrations for the N_2O-saturated HD-systems are presented in Tab. 2.16 and Fig. 2.28 a-b. While in this range of doses the concentration of amino groups in almost constant with dose, for the carboxyl groups we observe one order of magnitude increase from 20 to 80 kGy. Both carboxyl and amino groups concentrations increase with polymer concentration.

Data for the air-saturated systems are presented in Tab. 2.17 and Fig 2.29 a-b. The concentration of carboxyl groups is fairly low at 20 kGy and increases significantly with dose only for the low concentration system. The concentration of amino groups is not affected by dose for the lower concentration system, while increases with the dose for the higher concentration system. In Fig 2.30 the comparison between the air-saturated and N_2O-saturated 0.05 wt% systems irradiated at the two doses is reported. We observe that the amount of primary amino groups in N_2O and air-saturated 0.05 wt% systems are almost the same. On the contrary, the formation of carboxyl groups is influenced by the composition of the gaseous solutes present in the irradiated systems. Indeed, when N_2O-saturation is employed, the concentration of –COOH groups is higher than in the air-saturated analogues.

Table 2.16. Carboxyl and primary amino groups produced in N_2O-saturated HD systems.

System	Dose (kGy)	-COOH (M)	-NH_2(M)
0.05_HD	20	$2.58\ 10^{-5}$	$1.71\ 10^{-5}$
	40	n.a	$1.68\ 10^{-5}$
	60	n.a	$1.58\ 10^{-5}$
	80	$2.60\ 10^{-4}$	$2.40\ 10^{-5}$
0.1_HD	20	$4.81\ 10^{-5}$	$2.59\ 10^{-5}$
	40	n.a	$2.55\ 10^{-5}$
	60	n.a	$1.76\ 10^{-5}$
	80	$5.78\ 10^{-4}$	$1.68\ 10^{-5}$
0.2_HD	20	$1.03\ 10^{-5}$	$6.19\ 10^{-5}$
	40	n.a	$6.47\ 10^{-5}$
	60	n.a	$6.93\ 10^{-5}$
	80	$6.97\ 10^{-4}$	$5.48\ 10^{-5}$

Table 2.17. Carboxyl and primary amino groups produced in air-saturated HD systems.

System	Dose (kGy)	-COOH (M)	-NH_2 (M)
0.05_HD_Air	20	$1.61\ 10^{-8}$	$1.70\ 10^{-5}$
	40	n.a.	$1.69\ 10^{-5}$
	60	n.a.	$1.20\ 10^{-5}$
	80	$1.16\ 10^{-4}$	$1.52\ 10^{-5}$
0.5_HD_Air	20	$1.63\ 10^{-5}$	$2.58\ 10^{-5}$
	40	n.a.	$4.55\ 10^{-5}$
	60	n.a.	$7.67\ 10^{-5}$
	80	$2.47\ 10^{-5}$	$1.16\ 10^{-4}$

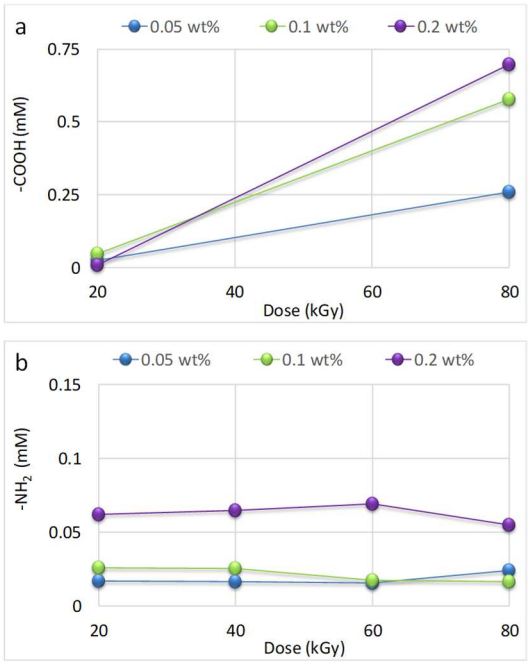

Figure 2.28 Carboxyl and primary amino groups produced in N_2O-saturated HD systems as function of the dose.

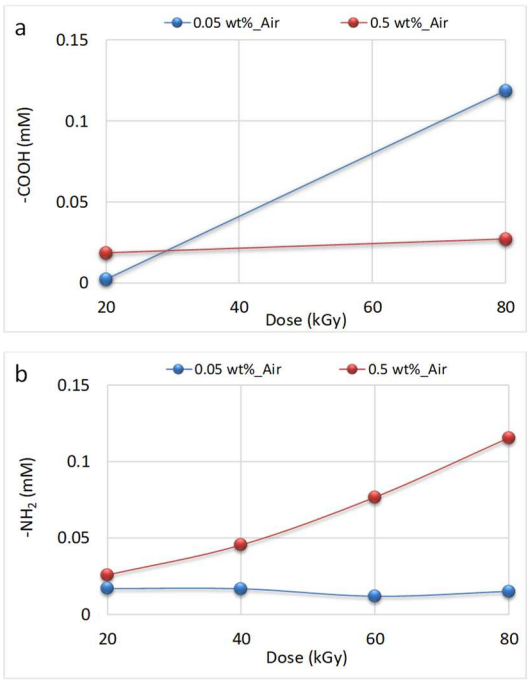

Figure 2.29. Carboxyl and primary amino groups produced in air-saturated HD systems as function of the dose.

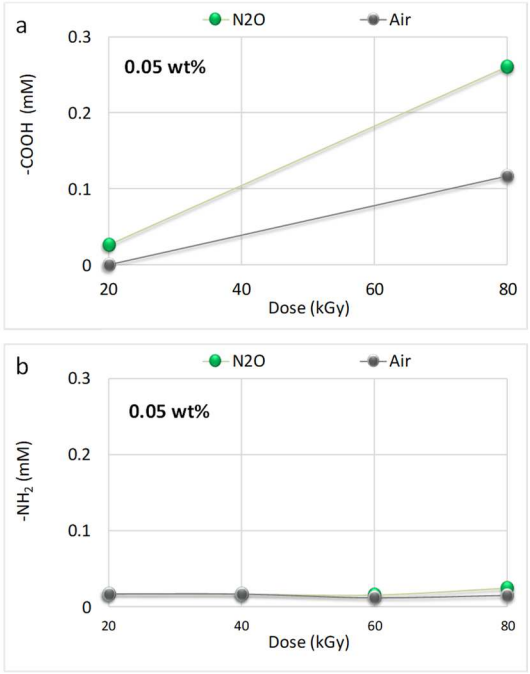

Figure 2.30. Primary amino groups (a) and carboxyl groups (b) produced in air- and N_2O-saturated 0.05 wt% HD irradiated systems.

2.3.8 Impact of double bonds on the quantitative analysis of H_2O_2 by I_3^-

The impact of double bonds on the quantitative analysis of H_2O_2 using the Ghormley triiodide method due to the presence of double bonds in the system was evaluated by a numerical simulation of the I_3^- production by H_2O_2 and consumption by double bonds using the experimentally determined rate constants (see Par. 2.3.4). The simulation was carried out for three possible situations: absence of double bonds in the system; concentration of double bonds lower than concentration of H_2O_2; and equal concentration of H_2O_2 and double bonds. The plots reported in Figure 2.31 refer to these three cases and the concentrations of I_3^- are representative of the concentrations in the cuvette where the measurement is performed (diluted with respect to the actual concentrations in the samples). When the concentration of double bonds is five times lower than the concentration of H_2O_2 the estimated H_2O_2

concentration is 20% lower than in the absence of double bonds. Significantly higher underestimations of H_2O_2 are made when their concentration are comparable. In Table 2.18 the ranges of the experimentally determined concentrations for H_2O_2 and double bonds are reported. We can conclude that the measured amount of H_2O_2 is generally lower than the effective concentration. In a future development of this work an alternative method for H_2O_2 quantification, using a method based on the complexation of H_2O_2 by $Ti(IV)OSO_4$ [13], will be applied.

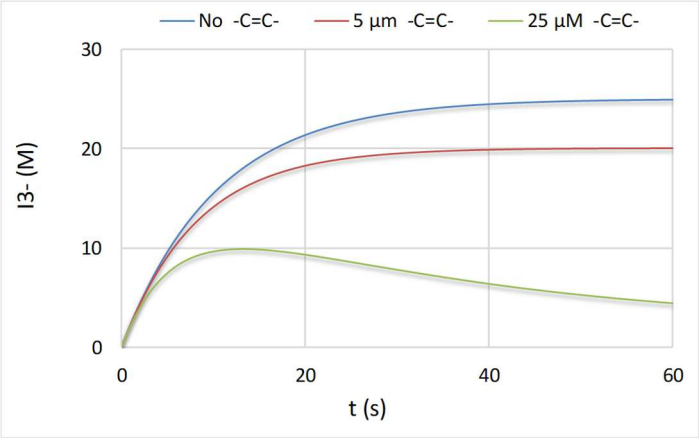

Figure 2.31. Numerical simulation of the I_3^- production by H_2O_2 (25 µM) and consumption by double bonds

Table 2.18. Concentration ranges of produced H_2O_2 and double bonds in N_2O- and air-saturated LD and HD systems

System	H_2O_2 (M)	Double bonds (M)
N_2O-sat LD	$10^{-5} – 10^{-4}$	$10^{-5} – 10^{-4}$
N_2O-sat HD	$10^{-4} – 10^{-3}$	10^{-4}
Air-sat LD	10^{-5}	$10^{-5} – 10^{-4}$
Air-sat HD	Non detectable	10^{-4}

2.4. Concluding remarks

The work presented in this chapter has confirmed that pulsed electron beam irradiation is able to transform a highly polydisperse linear polymer into a relatively monodisperse nanogel dispersion. Inter-/intramolecular crosslinking cause appreciable molecular effects in the early stages of the process, well below 20 kGy and then, up to 80 kGy there is not a significant modification of the molecular weight and hydrodynamic size of the irradiated PVPs. Inter-molecular crosslinking affects preferentially the shorter chains and/or smaller nanogel embryos, while intra-molecular crosslinking affects more the longer chains or bigger nanogel embryos. This explains the observed focusing effect on particle size distributions.

It was confirmed, experimentally and by numerical simulations, that in the typical polymer concentration range (dilute or semi-dilute conditions) required for the synthesis of nanoscalar networks the hydroxyl radicals are not quantitatively scavenged by the polymer precursor. This leads to H_2O_2 build up in the system and, subsequently, to production of molecular oxygen that, in turn, can react with the polymer radicals. Therefore, prolonging irradiation above 20 kGy, especially for those systems (and irradiation conditions) that favour hydrogen peroxide build up, oxidative chain scission occurs. This reaction does not significantly impact on the molecular weight and hydrodynamic size of the nanogels in virtue of the crosslinking points that join the chains, but generates a small fraction of low molecular weight fragments and introduces new useful chemical functionalities.

It was demonstrated that sealed vials, irradiated in N_2O-saturated conditions, are not strictly "oxygen free" throughout the process, while in sealed vials irradiated in air, O_2 is actually rapidly consumed. Yet, this "initial" difference in composition between the systems has a significant impact on the hydrodynamic size of the obtained nanogels. Indeed, when the oxidative chain scission is occurring in the early stages of the process (air-saturated systems) it has an impact on the molecular weight and size of the nanogels produced, allowing smaller particles to be obtained. Additionally, the lower G-value for hydroxyl radicals in air-saturated systems accounts for the lower

amount of hydrogen peroxide and oxygen produced, that results in a lower degree of polymer functionalization.

For the first time, double bonds were quantitatively estimated. Double bonds can be produced in radical-radical disproportionation reactions or in scission of alkyl radicals. At low doses, it appears that the increase in size at high and low polymer concentration parallels the formation of double bonds at the same concentrations. This may suggest that, for the low doses, the double bonds are mainly produced by disproportionation reactions. Since the ratio between crosslinking (combination) and disproportionation is known to be constant, double bonds concentration can be an indirect measurement of crosslinking density.

In the high dose range, we can expect that double bonds, as well other the other functional groups, are continuously formed but also consumed by reactions with water radiolysis products. Indeed, the chemical structure of the polymer appears profoundly modified, especially at the highest dose and lowest polymer concentration of the investigated ranges. The simulations will require further developments to include the specific features of the radiation chemistry of the polymer.

Acknowledgements

I wish to thank Prof. Mats Jonsson of the School of Chemical Science and Engineering, Applied Physical Chemistry, KTH Royal Institute of Technology, Stockholm, Sweden and Prof. Grazyna Przybytniak of the Centre for Radiation Research and Technology, Institute of Nuclear Chemistry and Technology, Warsaw, Poland for the access to the e-beam facilities at their respective Institutes. My gratitude goes also to the technical staff responsible for running the facilities.

Collaborators' contributions to the Chapter

Mr. Björn Dahlgren under the supervision of Prof. Mats Jonsson performed the numerical simulations.

Dr. Maria Antonietta Sabatino performed SLS measurements and provided support for GFC data analysis.

References

[1] J. A. Ghormley and A. C. Stewart, J. Am. Chem. Soc., 1956, 78,2934–2939.

[2] M.A. Sabatino, D. Bulone, M. Veres, A. Spinella, G. Spadaro, C. Dispenza, Structure of e-beam sculptured poly(N-vinylpyrrolidone) networks across different length-scales, from macro to nano. Polymer, 2013, 54(1), 54–64.

[3] C. Dispenza, M. A. Sabatino, N. Grimaldi, M. R. Mangione, M. Walo, E. Murugand and M. Jonsson, On the origin of functionalization in one-pot radiation synthesis of nanogels from aqueous polymer solutions. RSC Adv., 2016, 6, 2582–2591

[4] W. L. McLaughlin, A. W. Boyd, K. H. hadwick, J. C. McDonald and A. Miller, Dosimetry for radiation processing, Taylor and Francis, London, 1989.

[5] A.J. Elliot and D.M. Bartels, The reaction set, rate constants and g-values for the simulation of the radiolysis of light water over the range 20° to 350° C based on information available in 2008. AECL 153-127160-150-001. 2009

[6] A.J. Elliot, A pulse radiolysis study of the temperature dependence of reactions involving H, OH and e-aq in aqueous solutions. Int J Radiat Appl Instrum C Radiat Phys Chem, 1989, 34(5), 753-758.

[7] G.V Buxton, C.L. Greenstock, W.P. Helman, A.B. Ross, Critical review of rate constants for reactions of hydratatedelectrons, hydrogen atoms and hydroxyl radicals (•OH/•O-) in aqueous solutions. J.Phys Chem Ref Data, 1988, 17, 513-886.

[8] B. Dahlgren (2017, November 9). pyodesys (Version 0.11.5). Zenodo. http://doi.org/10.5281/zenodo.1044464

[9] B. Dahlgren (2017, December 4). chempy (Version 0.5.7). Zenodo. http://doi.org/10.5281/zenodo.1077133

[10] A.C. Hindmarsh et al. ACM Transactions on Mathematical Software 31 (2005) 363–396

[11] S. Kadlubowski Radiation-induced synthesis of nanogels based on poly(N-vinyl-2-pyrrolidone)— a review. Radiat Phys Chem., 2014, 102, 29–39.

[12] D. W. O'Sullivan, M. Tyree, The kinetics of Complex formation between Ti(IV) and Hydrogen peroxide. Int. J. Chem. Kinet. 2007, 39, 457– 461.

3. Ionising radiation engineered PVP-co-AA nanogel as biomedical nanocarrier

This chapter is dedicated to the PVP-based nanogel used as substrate in the development of potential biomedical nanodevices for the treatment of Alzheimer's disease and colorectal cancer.
In consideration of the envisaged application, this material has to fulfil some specific physico-chemical and biological requirements. The analysis of these aspects will be the topic of this chapter.

3.1 Introduction

Despite the many progresses done in medicine, successful early diagnosis and treatment strategies for several pathologies are still limited. The use of nanoparticles, if properly designed, can be an opportunity. Since they are characterized by a large surface-to-volume ratio and can be engineered to have a surface with several different reactive groups for multivalent bio-conjugation, they hold the promise to be multifunctional platforms with tunable size and properties able to carry out several functions in parallel, combining both diagnosis and therapy.
In order to maximize therapeutic efficacy while minimizing unfavourable side effects, the ideal nanocarrier should be able to accomplish as many of the following functions: (i) *protect* the drug minimizing its degradation and inactivation; (ii) *recognize* the pathological site where the drug release is required, avoiding the healthy tissues or cells; (iii) *modulate* the release upon an internal or external stimulus; (iv) enable in vivo *diagnosis* and carry out a *tracking* function; (v) easy to be degradable and/or eliminated, once completed his action on the organism.
Furthermore, these nanosized materials should be compliant with required physico-chemical properties (*i.e.* size, shape, charge), non-toxic, non-immunogenic,

hemocompatible, colloidally stable upon storage and administration, as reported in 1.4.

In this scenario, nanogels, 3D nanoscalar structure made by crosslinked hydrophilic polymers, are promising candidates. Indeed, nanogels are characterized by tuneable physico-chemical properties; they are flexible and adaptive in shape; they can be *stimuli responsive*. In particular, in this PhD project, dilute water solution of poly(N-vinyl pyrrolidone) (PVP) were irradiated using an industrial accelerator in the presence of a small amount of acrylic acid (AA). The use of AA allowed functionalizing the nanogels with more carboxyl groups (in addition to those produced by the PVP modification upon irradiation), since these groups can be employed for further NGs modification through the covalent attachment of molecules of interest. E-beam irradiation, in these systems, simultaneously promotes (i) intramolecular crosslinking of the linear polymer; (ii) some degree of intermolecular crosslinking and chain scission; (iii) AA grafting to the forming PVP nanoscale network and (iv) sterilization [1]. One advantage of using PVP as main component of our nanocarriers is its well-known biocompatibility, non-antigenicity [2] and mucoadhesive properties [3,4].

In order to understand if the synthesized PVP-co-AA nanogel satisfies the requirements of a biomedical nanocarrier, it was preliminary physico-chemically and biologically tested. For some *in vitro* and *in vivo* biological evaluations, fluorescent NG variants were produced and characterized.

3.2 Experimental

3.2.1 Materials

PVP k60 water solution (45 wt%), acrylic acid (AA), N-cadaverine-BOC (N-Boc-Cad), fluorescamine, acetonitrile, pyrocatechol violet (PV), Nickel(II) chloride hexahydrate, tetramethylrhodamine isothiocyanate mixed isomers (TRITC), amino-functionalized Atto488 (Atto488), amino-functionalized Atto633 (Atto633), 1-ethyl-

3-[3-dimethylaminopropyl] carbodiimide hydrochloride (EDC), N-hydroxysulfosuccinimide sodium salt (Sulfo-NHS), 2-(N-morpholino)ethanesulfonic acid hydrate (MES), Hepes. All chemicals were purchased from Sigma Aldrich and used as received.

3.2.2 Synthesis of poly(N-vinyl pyrrolidone)-co-acrylic acid nanogels

PVP aqueous solutions (0.5 wt%, molar concentration of repeating unit 45 mM) were prepared by overnight stirring, added with AA (0.9 mM, corresponding to a theoretical PVP repeating unit/AA molar ratio of 50), filtered with 0.22 μm pore size syringe filters, carefully deoxygenated with gaseous nitrogen and then saturated with N_2O ($N_2O \geq 99.99\%$) prior to irradiation. Electron beam irradiation was performed using a linear accelerator at the ICHTJ of Warsaw (Poland), Electronika 10/10 and supplying an integrated dose of 40 kGy in a single pass.

Irradiation was carried out at an average beam current of 0.45 mA, pulse length of 4.5 μs and pulse repetition rate of 400 Hz (or 300 Hz). A detailed description of the irradiation conditions is reported in 2.2.2. In general, irradiated systems after irradiation were dialyzed (12 kDa cut-off) against distilled water for 48h to remove eventual unreacted monomers, oligomers and low M_W polymer fractions.

3.2.3 NG-fluorescent variants

Nanogel was labeled with three different fluorescent probes: TRITC, Atto633 and Atto488. TRITC was grafted on NG through diaminopentane linker following a three steps reaction (see Fig 3.1): i. Grafting of the Boc-protected diaminopentane, N-Boc-Cad, on NG via amide-bond formation ($NG^{N\text{-}Boc\text{-}Cad}$); ii. Deprotection of the primary amino groups (NG^{Cad}); iii. Grafting of TRITC on NG^{Cad} (NG^{TRITC}).

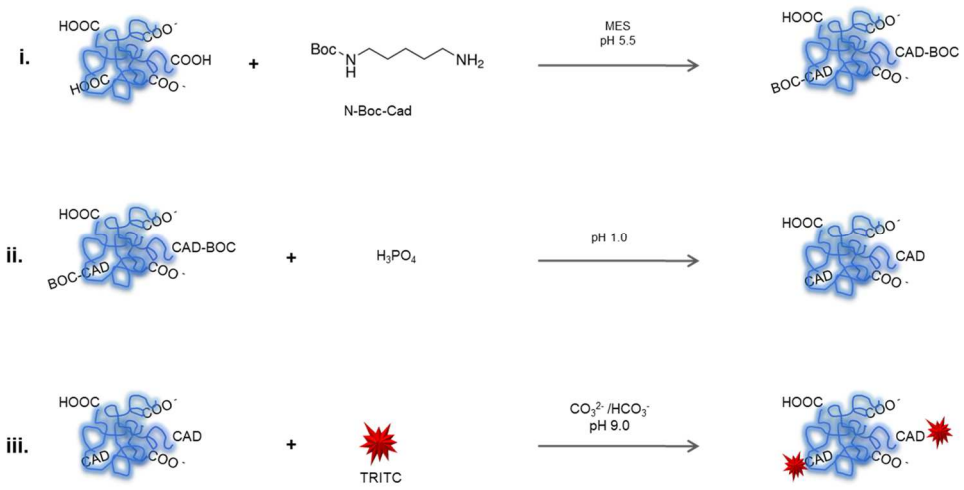

Figure 3.1. Reaction scheme of the conjugation in tree steps of TRITC on NG. Adapted from [5]

In detail, grafting of N-Boc-Cad on NG was achieved adapting an EDC/Sulfo-NHS protocol (for more details see Appendix A.7). A given volume of NG aqueous dispersion was mixed with EDC and Sulfo-NHS aqueous solution (MES, pH 5.5) for 30 minutes and, then, given volumes of N-Boc-Cad were added to partially convert the carboxyl groups in amino groups (20:1, 10:1, 3:1, carboxyl to amino group molar ratio). The reaction was conducted for four hours under gentle stirring at room temperature. For the deprotection step, a known volume of phosphoric acid was added to the $NG^{N\text{-}Boc\text{-}Cad}$ system to have a pH equal to 1-2 and stirring was provided for 24h. For the last reactive step TRITC, previously dissolved in DMSO, was added (carbonate-bicarbonate buffer, pH 9). In order to remove the unreacted reagents, prolonged dialysis against MilliQ water with 12 kDa cut-off membranes was conducted, after every reaction step. Grafting of TRITC on NGs was also carried out through a single step reaction. TRITC, previously dissolved in DMSO (1 mg/mL) was added to a given volume of NGs dispersion and carbonate/bicarbonate buffer (pH=9) and then incubated for 4 hours under gentle stirring at room temperature. In order to

remove the unreacted reagents, prolonged dialysis was conducted on NG-fluorescent system using 12 KDa cut-off membrane, against milli-Q water. Both reaction and purification were conducted under dark conditions.

The fluorescent NG-Atto variants (NG-Atto633 and NG-Atto488) were synthetized coupling the amino-functionalized dyes Atto 488 and Atto633 to the NG, using EDC and Sulfo-NHS to activate the carboxyl groups of the nanogel. In particular, a given volume of NG aqueous dispersion was mixed with EDC and Sulfo-NHS aqueous solution (MES, pH 5.5) for 30 minutes and, then, a given volume of fluorescent probe, previously dissolved in DMSO (1 mg/mL), was added in order to ensure two molar ratios between the nanogel carboxyl groups and Atto equal to 1.6 and 3.2. The reaction was conducted for further four hours under gentle stirring.

In order to remove the unreacted reagents, prolonged dialysis was conducted on the NG-fluorescent systems using a 12 KDa cut-off membrane, against milli-Q water. Both reaction and purification were conducted under dark conditions at room temperature. The conjugation degree, defined as the average number of fluorescent probe molecules per nanogel, was estimated by UV-vis absorption spectroscopy on purified NG-TRITC, NG-Atto633 and NG-Atto488 at λ= 552 nm, λ= 629 nm and λ= 501 nm, respectively. The measurements were performed at room temperature using a Jasco V 670 spectrophotometer (scan-speed 100 nm/min, band width 1 nm). In Fig. 3.2-3.4 the related calibration curves were built plotting the absorbance at peak on varying the fluorescent probe concentration. In order to calculate the concentration of NG it was taken into account the average Mw of NG (measured by SLS, for more details see Appendix A.2) and the polymer concentration upon conjugation and purification.

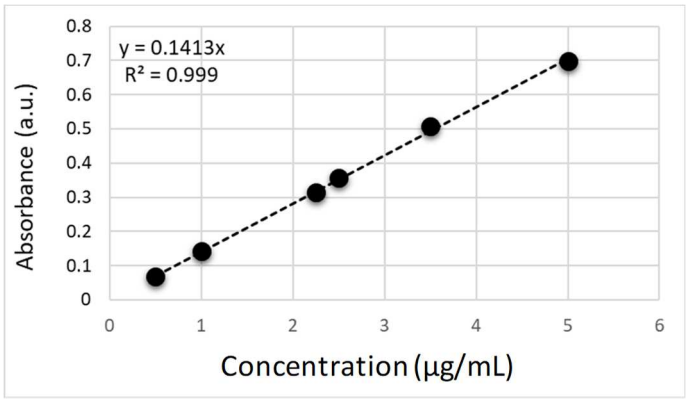

Figure 3.2. Calibration curve of TRITC fluorescent probe

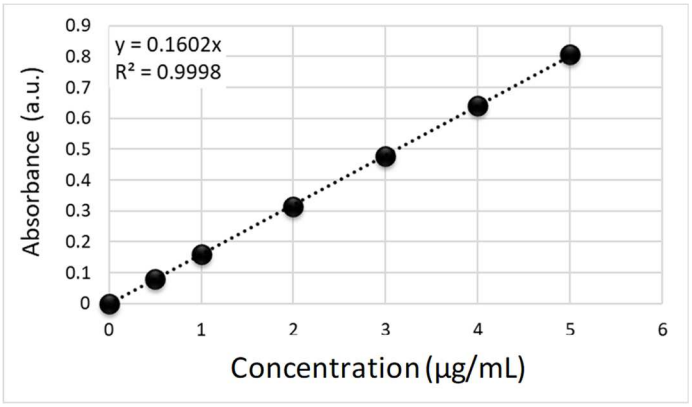

Figure 3.3. Calibration curve of ATTO 488 dye.

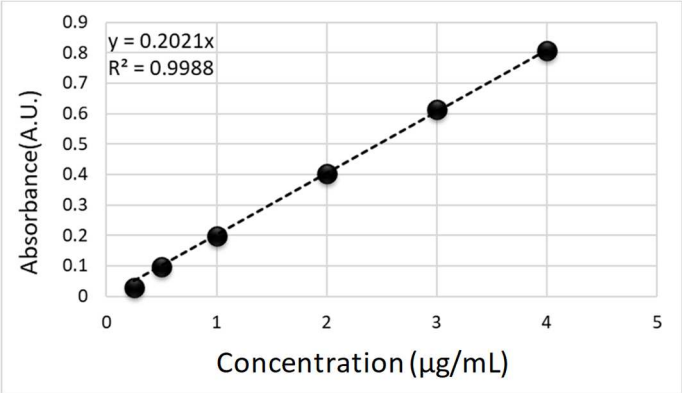

Figure 3.4. Calibration curve of ATTO633 dye

3.2.4 Physico-chemical characterizations of NG-fluorescent variants

Dynamic Light Scattering analysis (DLS)

The hydrodynamic dimensions of the differently conjugated NG variants were measured by DLS (for more details see Appendix A.1). All samples were measured at the concentration of 0.05 wt% to avoid multiple scattering. Samples recovered from dialysis were also filtrated with 0.45 µm syringe filters to remove impurities. In consideration of their monomodal size distribution, DLS data were analyzed according to the method of cumulants [6].

Gel Filtration Chromatografy (GFC)

Gel filtration chromatography (GFC) analysis was performed on selected NG systems at the concentration of 0.05 wt%. For more details, see Appendix A.3.

ζ-potential measurements

ζ-potential measurements were carried out on selected NG systems dispersed in water, previously diluted to the final concentration of 0.05 wt% and at 25 °C. Systems were

characterized by a monomodal ζ-potential distribution. Measurements were carried out in triplicate from minimum two batches with good reproducibility. For more details, see Appendix A.4.

3.2.5 Stability studies

NG-Atto633 system was subjected to storage stability studies at 4°C over a period of 9 months as colloidal dispersion. In order to test the colloidal stability in the presence of serum proteins, pre-filtered (0.45 μm pore size filter) NG-Atto633 was incubated with fetal bovine serum (FBS, 10% v/v) at 37°C for 24 hours. DLS measurements were then performed at 25±0.1 °C and at 90° scattering angle without filtration, after dilution with isotonic PBS to the final concentration of 0.025 wt% to minimize FBS absorption at the laser wavelength.

3.2.6 Morphological analysis of NG-Atto633 in mouse urine

Surface morphology of urine NG-Atto633 dispersion after dialysis in Milli-Q water and NG dispersion control systems were evaluated by SEM measurements. For more details, see Appendix A.5.

3.2.7 Biological Evaluations

In collaboration with IBIM and IBF of the Council of National Research, Palermo and with Dipartimento di Biopatologia e Biotecnologie Mediche, Sezione di Biologia e Genetica, Università degli Studi di Palermo, "bare" and selected NG fluorescent variants were subjected to *in vitro* and *in vivo* biological evaluations.

In particular, *in vitro* biocompatibility of "bare" NG was tested on different cell lines: neuroblastoma cells (LAN5), peripheral blood mononuclear cells (PBMCs), colon cancer cell lines (SW620). Cellular uptake experiments of NG-Atto633 systems were conducted on SW480 cell line.

The *in vivo* evaluations were performed on a selected NG-Atto633 system after

intraperitoneal administration. In particular, biocompatibility, biodistribution and clearance were investigated. More details on this experimental section are reported in Appendix B1.

3.3 Results and discussion

3.3.1 Synthesis of nanogel and its fluorescent variants

Characterization of the nanogel used as substrate

The synthetic strategy used to produce nanogels by high energy irradiation of semi-dilute aqueous solutions of the poly(N-vinyl pyrrolidone) in the presence of small amounts of a functional monomer, developed my research group, is described more in detail elsewhere [1,7,8]. Briefly, irradiation with pulsed electron beams induces mainly intra-molecular crosslinking of PVP (although also inter-molecular crosslinking may occur up to some extent) and the grafting of the functionalized monomer on the polymer. For the purpose of the present study, a new variant of functionalized PVP nanogel was synthesized, choosing a relatively high polymer concentration in water (0.5 wt%) and adding a small amount of acrylic acid to generate an anionic nanocarrier with pendant carboxyl groups. Hydrophilicity and slightly anionic surface charge are likely to create unfavorable conditions for protein opsonization in the bloodstream and eliminate initiation of immunogenic responses, thus increasing the circulation time [9].

The NGs used as substrates for the different applications were produced in different sets of syntheses that correspond to slightly different irradiation parameters, but always with the same dose per pass of 40 kGy and in N_2O-saturated conditions. Systems produced with the same set-up were reproducible, but some differences in terms of hydrodynamic dimension and ζ-potential were observed among the different sets. Some general features can be identified: average hydrodynamic diameters in the 40-80 nm range, weight average molecular weight in the 4.5-6 MDa range, fairly

narrow particle size distribution (PDI between 0.25 and 0.3), and slightly negative surface electric charge density (-17± 5.8 to -32 ± 5.6 mV). The nanogels have both carboxyl (av. 40 ± 5 per NG) and primary amino groups (av. 70 ± 5 per NG) [1,10].

Synthesis and physico-chemical characterization of NG fluorescent variants

NG modification to produce fluorescent variants was performed by optimizing the conjugation reaction conditions in order to ensure an adequate emission signal for the characterization and limit to the minimum the modification of NGs physico-chemical properties upon conjugation. In particular, in this study the conjugation of three different fluorescent probes, TRITC, Atto488 and Atto633 was performed.

TRITC conjugation was performed promoting the reaction between a primary amino group and the isothiocyanate group of the fluorescent probe according two different approaches. In particular, in the first one, a linker, namely N-Boc-Cad, was employed and a shift in chemical functionality of the nanogels from carboxyls to primary amines occurred (see Figure 3.1). In the second conjugation approach, a direct conjugation reaction with the amino groups of NG was performed. When the linker was employed, three conjugation degrees (24, 7, and 2 were obtained, which all yield to fluorescent nanogels suitable to perform the required biological characterizations. In Tab. 3.1 the corresponding hydrodynamic size and ζ-potential values are reported.

Table 3.1. Average hydrodynamic diameter (D_H) and size distribution width (±) and ζ-potential with variation indicating the width of the distribution related to bare NGs and NG-TRITC conjugated variants [5].

System	Conjugation degree	D_H (nm)	ζ-potential (mV)
NG	/	65 ± 21	-32 ± 5.6
NG-TRITC	2	62 ± 18	-30 ± 6.1
NG-TRITC	7	64 ± 19	-15 ± 8.2
NG-TRITC	24	66 ± 21	5 ± 12

Hydrodynamic diameter is never appreciably modified upon conjugation, due to the comparatively small size of the probe with respect to the nanogel, whereas the surface charge density, originally negative, increases approaching zero at the increase of the conjugation degree that corresponds to a higher carboxyl-to-primary amino group shift. For this reason, in order to preserve the anionic charge, the system with the lowest conjugation degree was selected in the *in vitro* biological tests. For a selected condition, TRITC was conjugated also promoting the reaction between the primary amino groups of NGs and obtaining comparable yield. (data non shown).

NGs were also conjugated with two amino-modified, fluorescent probes, Atto488 and Atto633, by reacting the amino group of the probe with the EDC/SulfoNHS activated carboxyl group of the NG. Atto488 and Atto633 were selected since they are highly emissive and highly photo-stable. Thanks to high quantum yield, they ensure measurable signals even at very low conjugation degrees, hence with minimal modification of the physico-chemical properties of the nanocarrier. The high photo-stability makes them suitable for *in vivo* and *ex vivo* studies. In Tab 3.2 the hydrodynamic size and ζ-potential values of Atto-modified nanogels are reported.

Table 3.2. Average hydrodynamic diameter (D_H) and size distribution width (±) and ζ-potential with variation indicating the width of the distribution related to bare NGs and NG-Atto conjugated variants.

System	Conjugation degree	D_H (nm)	ζ-potential (mV)
NG	/	67 ± 21	-17 ± 5.8
NG-Atto488	1	72 ± 23	-15 ± 8.90
NG-Atto488	2.5	74 ± 22	-18 ± 7.9
NG-Atto633	4	75 ± 23	-16 ± 5.9
NG-Atto633	7	75 ± 26	-12 ± 6.9

As shown in Tab 3.2, hydrodynamic size and the surface charge density were not significantly modified upon conjugation. Under the selected reaction conditions, the conjugation efficiency of Atto488 and Atto633 was of ca. 6% and 22%, respectively. Since NG-Atto633 with 7 probe molecules per NG showed the best emission

response, it was selected for further physico-chemical and *in vitro*, *in vivo* and *ex vivo* biological evaluations.

In Fig 3.5 the GFC chromatograms of NG and NG-Atto633 are reported.

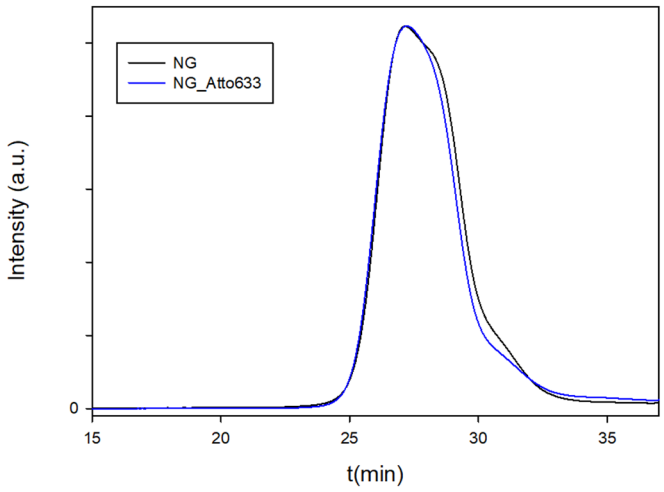

Figure 3.5. GFC chromatograms of "bare" NG and NG-Atto633 conjugated system

The GFC measurements confirm the results obtained from DLS analysis; no appreciable modification of the hydrodynamic volume distribution of NG upon conjugation was observed.

In order to confirm that a strong bond is formed between NG and Atto633, the purified NG-Atto633 dispersion was subjected to centrifuge-filtration (100 kDa cut-off). The eluted systems were then analyzed by both UV-vis absorption and fluorescence spectroscopy. No signals related to Atto633 were detected in the eluted solutions. In order to ascertain if a less hydrophilic medium could trigger the release of Atto633, centrifuge-filtration was also conducted after incubation with cell culture medium for 3 h at 37°C (1:1 volume ratio). Also in this case, no release of probe was detected.

3.3.2 Stability studies

NG-Atto633 dispersion was subjected to two different colloidal stability tests. In particular, the colloidal stability of NG-Atto633 over time (9 months, 4° C) and in presence of serum proteins was investigated. In Table 3.3, hydrodynamic diameters and width of size distribution of NG-Atto633 under these conditions are reported. The hydrodynamic diameters of NG-Atto633 conjugated systems did not change over a period of 9 months (sored at 4°C) neither it did after incubation with Fetal Bovine Serum (10% v/v) for 24 h. In the latter case, only a slight increase of polydispersity was observed. However, these results suggest that no irreversible aggregation phenomena occur. The fluorescence signal from NG-Atto633 was also unmodified after incubation.

Table 3.3. Average hydrodynamic diameter (D_H) and width of size distribution values for NG-Atto633 as produced, after 9 months storing at 4°C, and after incubation with FBS (10% v/v) for 24h at 37° C

System	**D_H (nm)**		
	t = 0	t = 9 months, 4°C	After 24h in FBS
NG-Atto633	75 ± 26	76 ± 26	77 ± 37

3.4 Biological evaluations

3.4.1 Biocompatibility and immunogenic response after NG treatment

In order to ensure an effective and safe use of the synthetized nanogels in medical applications, it is crucial to evaluate as a first step their *in vitro* and *in vivo* biocompatibility, ascertaining that, when interacting with the cells, they do not induce toxicity as well as proliferative, immunogenic and thrombogenic responses.

In vitro evaluations

LAN5 neuroblastoma cells were used as cell model in order to test the effect of NG

on cell viability. Cells were treated with the NGs at increasing concentrations, for 24 hours. No cytotoxicity was observed up to a concentration of 0.65 mg mL^{-1}, as detected by MTS cell metabolic activity test (Figure 3.6-a). This result was confirmed by microscopic inspection of the cells, which did not show any morphological change when treated with NG up to the concentration of 0.65 mg mL^{-1}, and degeneration when treated with higher concentrations (Figure 3.6-b). Moreover, at the concentrations tested, no proliferative effect was observed. Furthermore, other parameters, such as mitochondrial activity and mitochondrial membrane potential ($\Delta\Psi m$), were analyzed (data not shown). All the analyzed parameters were maintained at basal level, thus showing that no cellular or mitochondrial stress or proliferative processes were activated by NG.

Further investigations were performed on human blood cells. Indeed, human lymphocytes are a suitable model for studying response to different stresses and effect on inflammation caused by different stimuli such as Aβ [11,12]. To evaluate whether NG could produce injurious effects we treated peripheral blood mononuclear cells (PBMCs) with NG dispersions at two concentrations, lipopolysaccharides (LPS), an activator of inflammatory response, and Aβ. Cell viability, oxidative stress and inflammatory tests were performed. In particular, in presence of LPS, cell viability was redoubled [13]; in contrast, in presence of Aβ, it was reduced to 50%, whereas the value of the samples treated with NG was comparable to the control (Figure 3.7). NG did not induce oxidative stress and did not cause an inflammatory response on the contrary of Aβ and LPS, respectively. (data no shown).

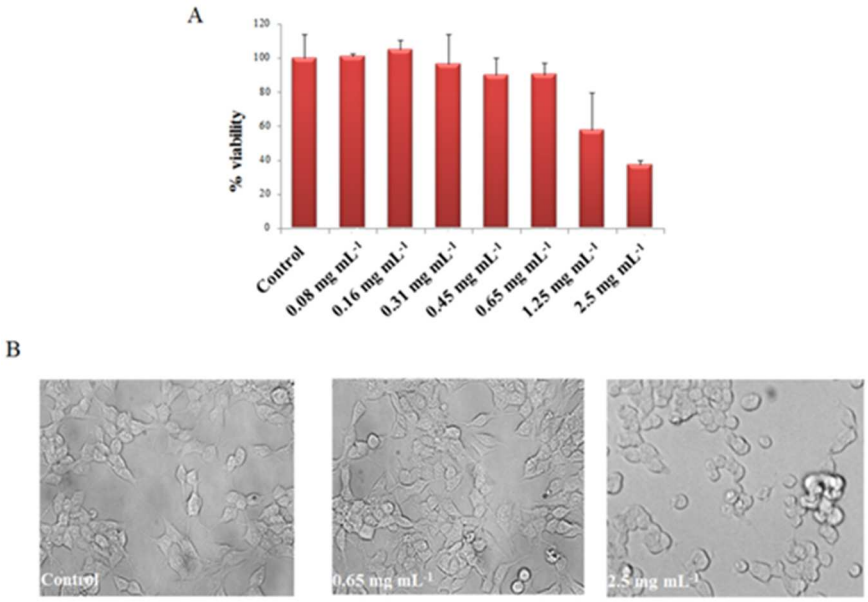

Figure 3.6. NG in LAN5 cells does not activate cellular toxicity, mitochondrial and oxidative stresses.A) LAN5 neuroblastoma cells untreated (Control) and treated with NG at different concentrations (0.08, 0.16, 0.31, 0.45, 0.65,1.25 and 2.5 mg mL^{-1}) for 24 hand submitted to MTS assay. B) Representative morphological images of LAN5 untreated cells (Control), or treated with NG at the concentrations of 0.65 and 2.5 $mgmL^{-1}$ for 24 h. [5]

Moreover, to be assured of its biosafety, the hemocompatibility and plasma coagulation skill of NG was investigated by *in vitro* tests. The results showed that the hemolysis percentage and blood indicators of plasma coagulation (prothrombin time and partial thromboplastin time) induced by the presence of NG are comparable to the negative and untreated controls. (data no shown).

All these findings indicate that the chemical structure and functional groups of NGs, make them not cytotoxic, non immunogenic and hemocompatible.

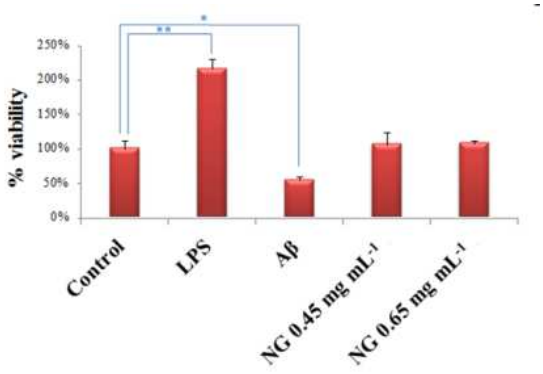

Figure 3.7. Cell viability responses in blood cells. PBMCs untreated (Control) or treated with NG at different concentrations or with Aβ and LPS and submitted to MTS assay. Adapted from [5]

In vivo evaluations

In order to test the *in vivo* biocompatibility and the immunogenic response of NG, an intraperitoneal injection in a mouse model was performed. A histological analysis was done to evaluate if the NG administration could damage tissues and organs. In particular, accumulation in liver and kidneys can cause organ toxicity [14,15]. Thus, these two organs, in which NGs are mostly present after injection (as it will be discussed in the next paragraph), were inspected 4 and 24 hours after the treatment (Fig. 3.8). As seen in Figure 3.8, no tissue or cellular damages were observed in the mice injected with the NGs, when compared to images obtained from untreated mice. In particular, neither degeneration of the tubules and glomeruli nor hemolysis and inflammatory processes in the kidneys section were observed at both the examined times. In the liver hepatocyte sections, necrosis with swollen cellular nuclei, hypertrophied blood vessels, cytoplasmic lesions were not present.

Furthermore, it was proven that NGs did not cause any immune or hemolytic response *in vivo*. After NG administration the total blood proteins were analyzed and no significant difference was revealed with respect to the control.

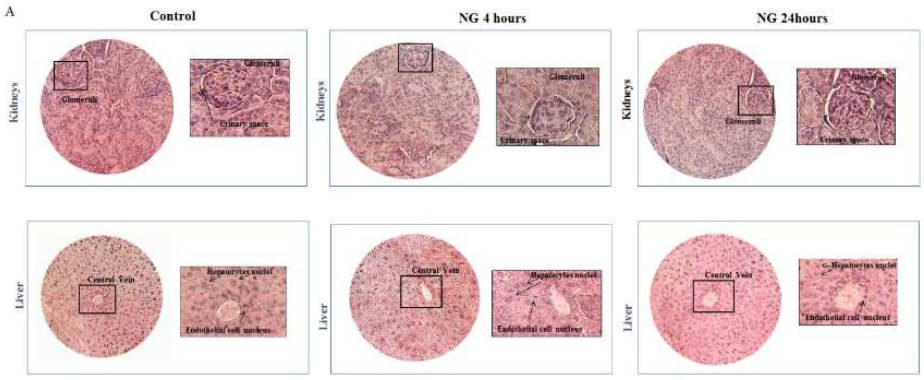

Figure 3.8. Biocompatibility of kidneys, liver tissues, blood parameters and immunological response after NG-Atto633 i.p. injection. Representative histological sections of kidneys and liver of control (left) and NG-Atto633 treated mice (right). Sections were stained with H&E and observed under a light microscope at 40X magnification. Adapted from [16]

3.4.2 Cell uptake experiments

In order to investigate the ability of NG-fluorescent variants to penetrate the cell membranes, uptake assays by confocal analysis on SW cells (colon cancer cell lines) after 1h and 3h of treatments was performed. In particular, NG-Atto633 (CD=4 or 7) characterized by the conjugation degree reported in brackets were used. In Fig 3.9 the confocal analysis microscopies performed on these conjugated systems are reported. NG-Atto633 with the two different conjugation degrees, was internalized at the cytosolic and nuclear level (Fig 3.9). These results suggested the use of NG-Atto633 (CD = 7) for further *in vivo* evaluations.

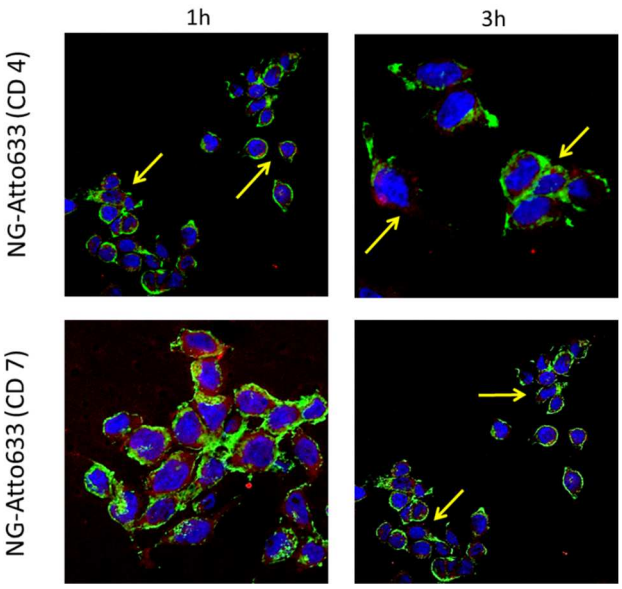

Figure 3.9. Confocal maximum projection of SW480 cells (nuclei labeled with DAPI (blue fluorescence) and cellular membranes labeled with AlexaFluor 488 Phalloidin (green fluorescence)) incubated 1 or 3 hours with NG-Atto633 (red fluorescence).

3.4.3 Biodistribution and clearance of the nanogel

Intraperitoneal administration was chosen to study the biodistribution and clearance of NG. For this purpose, we used NG-Atto633 with the highest conjugation degree (7 Atto633 per NG). NG-Atto633 was intraperitoneally injected in mice and the blood was sampled at 4 and 24 hours and analysed by using a fluorescence scanner.

The results are shown in the histogram in Figure 3.10-a. After 4 hour from administration, the nanogels were able to reach the bloodstream and were completely eliminated in 24 hours. The biodistribution of the labeled nanogel was verified 4 and 24 hours after treatment in several organs; in particular, brain, lungs, heart, bladder, kidneys, spleen and liver have been explanted and analyzed (Fig. 3.10-b). It is evident

that 4 hours after administration most of the NG-Atto633 signal is detected in liver and kidneys that are the two organs implicated in the route of excretion from the body. Noticeably, 24 hours after administration, the fluorescence is drastically reduced indicating that NG has been or is being eliminated from the body. A residual fluorescence signal, that is about 30% of the 4-hour value, is still present in liver and spleen. Longer observation times and repeated administrations will be required to ascertain that no accumulation occurs.

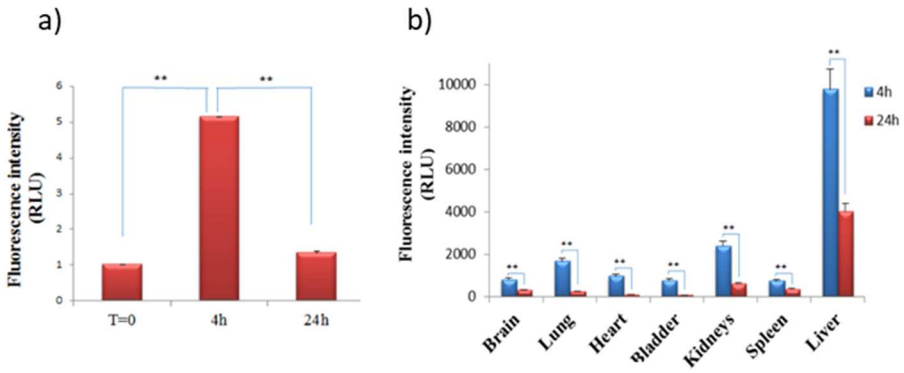

Figure 3.10. Ex vivo blood and organ fluorescence imaging after NG-Atto633 intraperitoneal injection. a) Relative fluorescence intensity values recorded in blood samples after 4 and 24 hours from injection of 50 µl of NG-Atto633. s and b) Relative fluorescence intensity values of whole organs of control mouse and injected mice after 4 and 24 hour. Each data point represents the mean ± SD of n = 5. **p<0.02 vs. indicated groups. Adapted from [16]

In order to test the clearance of NGs from the body, analyses were performed by fluorescence spectroscopy, scanning electron microscopy (SEM) and light scattering techniques on the urines collected at different times up to 24 hours. As shown in Figure 3.11-a, the peak of fluorescence intensity of the NG-Atto633 was detected in the urines spotted 4 hours after the treatment. Then, a decrease of the signal at longer times, up to 24 hours was observed. In order to confirm the presence of the NGs in

the urines, a SEM analysis was performed and particles of the order of 100 nm were observed (Fig. 3.11-b). Also, DLS measurements in the urines collected after 0, 4, 8, 12 and 24 hours from the treatment with NG-Atto633, showed a maximum light scattered intensity after 4 hours, that rapidly decreased as a function of time, in perfect agreement with fluorescence signal (Fig. 3.11-c). DLS measurements performed on dialyzed urines, collected after 4 hours from i.p. injection of NG-Atto633 dispersion, show the same hydrodynamic size of NG-Atto633 before administration. Moreover, fluorescence measurements performed in the 4-hour urine samples, before and after dialysis, indicated that the probe remained linked to NG (data not shown)

Although the renal cutoff is about 8 nm [17], it has been hypothesized that the flexible, open structure of NGs [10,18,19] made them capable of passing through glomerular filtration. (Fig. 3.11-b).

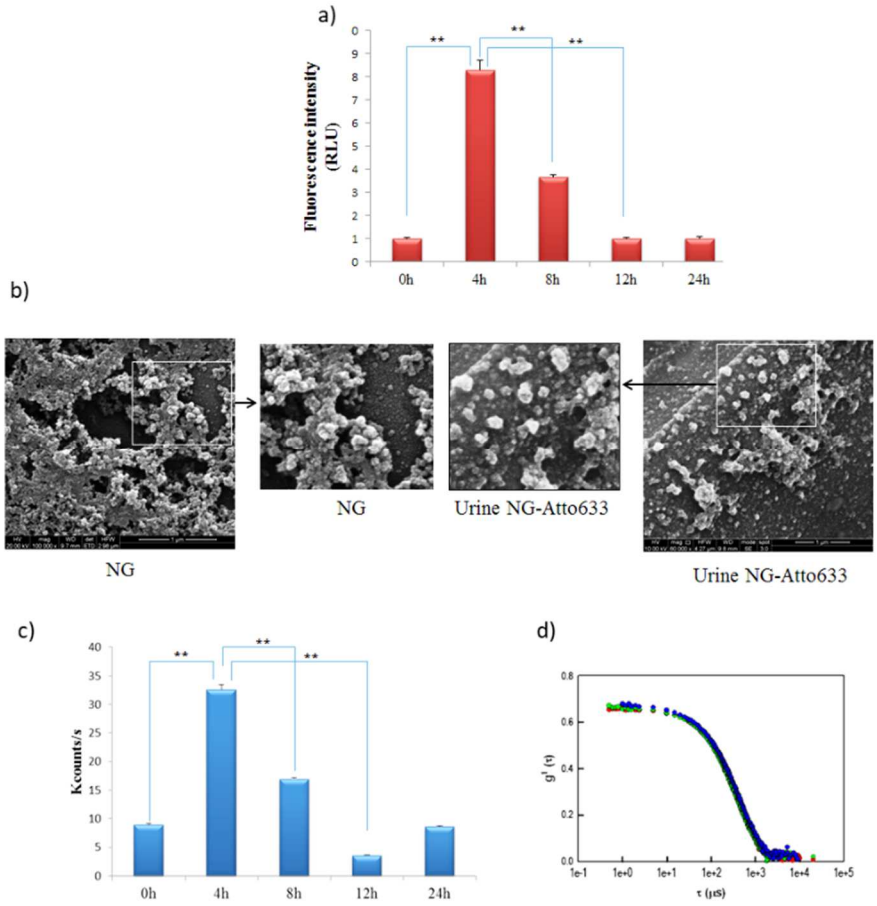

Figure 3.11. Urine analysis after NG-Atto633 intraperitoneal injection. a) Relative fluorescence intensity values recorded in urine samples collected after 0, 4, 8, 12 and 24 hours from injection. b) Morphological analysis of NG-Atto633 as prepared and in urine after 4 hours from injection by SEM. High magnification SEM images are evidenced in the squares. c) Light scattering intensity obtained by urine samples collected from pre-treated (0h) and treated mice at 4, 8, 12 and 24 hours. d) Correlation functions obtained by light scattering measurements performed on: bare NG dispersion (green), "as prepared" NG-Atto633 dispersion (red) and NG-Atto633 in urine collected after 4 hours from i.p. injection (blue). Each data point represents the mean ± SD of n = 5. **p<0.02 vs. indicated groups. Adapted from [16]

3.5 Conclusions

The synthetic strategy that makes recourse to ionizing irradiation enables the manufacturing of nanogels at a large scale. Product purification via ultrafiltration is straightforward since no recourse to catalysts, initiators, organic solvents or surfactants is made. The engineered nanogel system shows hydrodynamic size (ca. 60 nm), negative surface charge density, and useful functional groups particularly suitable for the envisaged application.

The *in vitro* and *in vivo* biological response of NG is encouraging. In fact, NG biocompatibility (absence of toxicity, proliferative, immunogenic, and thrombogenic responses) and clearance from the bloodstream and urines within 24 h encourage the use of the PVP-co-AA based nanogel as substrate of biomedical nanodevices.

Acknowledgements

I wish to thank Dr. Grazyna Przybytniak and the Centre for Radiation Research and Technology, Institute of Nuclear Chemistry and Technology, Warsaw, Poland for access to the e-beam facilities.

This research was partially supported by a grant from the Italian Ministry of University and Scientific Research (PRIN 2010-2011 NANOMED), by the Università of Palermo "Fondo Finalizzato alla Ricerca (FFR) 2012/2013" and by the Italian Ministry of University and Research in the framework of the Flagship Project NonoMAX (n° 79E13000270005).

Collaborators' contributions to the Chapter

Dr. Maria Antonietta Sabatino performed SLS measurements and analysed the data; she also advised me in the design of some experiments and in performing DLS measurements.

Dr. Viviana Costa (Piattaforma Tecnologica per l'Ingegneria Tissutale, Teranostica ed Oncologia, Istituto Ortopedico Rizzoli, Palermo, Italy) performed cell uptake assays

by confocal microscopy.
Dr. Pasquale Picone (Istituto di Biomedicina e Immunologia Molecolare (IBIM) of National Research Council (CNR), Palermo, Italy) performed all the other biological evaluations.

References

[1] N. Grimaldi, M.A. Sabatino, G. Przybytniak, I. Kaluska, M.L. Bondì, D. Bulone, S. Alessi, G. Spadaro, C. Dispenza, High-energy radiation processing, a smart approach to obtain PVP-graft-AA nanogels, Radiat. Phys. Chem. 9 (2014) 76–79.

[2] H.A. Ravin, A.M. Seligman, J. Fine, Polyvinyl pyrrolidone as a plasma expander - Studies on its excretion, distribution and metabolism, N. Eng. J. Med. 247 (1952) 921-929.

[3] I.A. Alsarra, Mucoadhesive polymeric hydrogels for nasal delivery of acyclovir, Drug Dev. Ind. Pharm. 35 (2009) 352-362.

[4] K. Suknuntha, V. Tantishaiyakul, N. Worakul, W. Taweepreda, Characterization of muco- and bioadhesive properties of chitosan, PVP, and chitosan/PVP blends and release of amoxicillin from alginate beads coated with chitosan/PVP, Arch. Neurol. 69 (2012) 29-38.

[5] P. Picone, L.A. Ditta, M.A. Sabatino, V. Militello, P.L. San Biagio, M.L. Di Giacinto, L. Cristaldi, D. Nuzzo, C. Dispenza, D. Giacomazza, M. Di Carlo, Ionizing radiation-engineered nanogels as insulin nanocarriers for the development of a new strategy for the treatment of Alzheimer's disease, Biomaterials 80 (2016) 179–194.

[6] D.E. Koppel, Analysis of macromolecular polydispersity in intensity correlation spectroscopy: the method of cumulants, J. Chem. Phys. 57 (1972) 4814-4820.

[7] C. Dispenza, M.A. Sabatino, N. Grimaldi, G. Spadaro, D. Bulone, M.L. Bondì, G. Adamo, S. Rigogliuso, Large-scale Radiation Manufacturing of Hierarchically Assembled Nanogels, Chem. Eng. Transact. 27 (2012) 229-234.

[8] C. Dispenza, N. Grimaldi, M.A. Sabatino, S. Todaro, D. Bulone, D. Giacomazza, G. S. Przybytniak, S. Alessi, G. Spadaro, Studies of network organization and dynamics of e-beam crosslinked PVPs: From macro to nano, Radiat. Phys. Chem. 81 (2012) 1349-1353.

[9] D.E. III Owens, N.A. Peppas, Opsonization, biodistribution, and pharmacokinetics of polymeric nanoparticles, Int. J. Pharm.307 (2006)93–102.

[10] G. Adamo, N. Grimaldi, S. Campora, D. Bulone, M.L. Bondì, M. Al-Sheikhly, M.A. Sabatino, C. Dispenza, G. Ghersi, Multi-functional nanogels for tumor targeting and redox-sensitive drug and siRNA delivery, Molecules 21 (2016) art. # 1594.

[11] C. Velez-Pardo, G.G. Ospina, M. Jimenez del Rio, Abeta peptide and iron promote apoptosis in lymphocytes by an oxidative stress mechanism: involvement of H_2O_2, caspase-3, NF-kappaB, p53 and c-Jun, Neurotoxicology 23 (2002) 351-365.

[12] M. Pellicanò, M. Bulati, S. Buffa, M. Barbagallo, A. Di Prima, G. Misiano, P. Picone, M. Di Carlo, D. Nuzzo, G. Candore, C. Vasto, D. Lio, C. Caruso, G. Colonna-Romano, Systemic immune responses in Alzheimer's Disease: in vitro mononuclear cell activation and cytokine production, J. Alzheimer's Dis. 21 (2010) 181-192.

[13] L. Jansky, P. Reymanova, J. Kopecky, Dynamics of cytokine production in human peripheral blood mononuclear cells stimulated by LPS or infected by Borrelia, Physiol Res. 52 (2003) 593-598.

[14] D. Naraynan, S. Nair, D. Menon, A systematic evaluation of hydroxyethyl starch as a potential nanocarrier for parenteral drug delivery, Int. J. Biol. Macromol. 74 (2015) 575–584.

[15] C.A. Simpson, B.J. Huffman, A.E. Gerdon, D.E. Cliffel, Unexpected toxicity of monolayer protected gold clusters eliminated by PEG-Thiol place exchange reactions, Chem. Res. Toxicol. 23 (2010) 1608–1616.

[16] P. Picone, M.A. Sabatino, L.A. Ditta, A. Amato, P.L. San Biagio, F. Mulè, D. Giacomazza, C. Dispenza, M. Di Carlo, Nose-to-brain delivery of insulin enhanced by a nanogel carrier, J. Control. Release, 270 (2018) 23-36.

[17] M. Longmire, P.L. Choyke, H. Kobayashi, Clearance properties of nano-sized particles and molecules as imaging agents: Considerations and caveats, Nanomedicine 3 (2008) 703-717.

[18] C. Dispenza, M. Sabatino, N. Grimaldi, M. Mangione, M. Walo, E. Murugan, M. Jonsson, On the origin of functionalization in one-pot radiation synthesis of nanogels from aqueous polymer solutions, RSC Advances 6 (2016) 2582-2591.

[19] C. Dispenza, G. Spadaro, M. Jonsson, Radiation Engineering of Multifunctional Nanogels, Top. Curr. Chem. 374 (2016) 69.

4. NG-Insulin: a nanodrug delivery system for the potential treatment of Alzheimer's disease

In this Chapter the potential therapeutic applications of insulin-nanogel conjugate for the treatment of neurodegenerative disorders, and, particularly, in Alzheimer's disease is presented.

4.1 Introduction

A psychiatrist and neuropathologist, Alois Alzheimer, reported "A peculiar severe disease process of the cerebral cortex" to the 37th Meeting of South-West German Psychiatrists in Tubingen on Novembers, 1906. [1]

Dr. Alzheimer could not imagine that "his" disease still nowadays, after about one hundred years, has not a well-established explanation, or timely diagnosis and efficacious treatments.

According to Alzheimer's Disease International (the worldwide federation of Alzheimer associations), nearly 44 million people worldwide have Alzheimer's or a related dementia but only 1 out off 4 people with Alzheimer's disease have been actually diagnosed. Alzheimer's disease is officially listed as the sixth-leading cause of death in the United States. In 2010 it was estimated that 5.4 million Americans would be affected by AD in 2016, 97% of them older than 65 years old. [2] According several studies and statistics, a dramatic increase of affected people in the next years is to be expected. By 2025, the number of people age 65 and older with AD is predicted to increase to almost 40% reaching 7.1 million, and to an impressive number of 13.8 million by 2050, this without any medical breakthroughs both in diagnosis and treatment. [2]

From an economical point of view, it is obvious that with this massive number of involved patients, also the costs of care are enormous. Indeed, the cost of Alzheimer's and dementia care in 2016 was estimated to be $605 billion worldwide and $236

billion in US only.

For decades now, researchers have investigated multiple aspects of AD pathogenesis in order to provide suitable treatment strategies, but much more is yet to be learnt about the specific biological changes that cause this pathology and how prevention, slowdown and cure can be attained.

What it is known so far about this neurodegenerative disease is that the decline in memory, language and other cognitive skills is due to damage or destruction of neuronal cells in several brain area including the cerebral cortex, hippocampus, entorhinal cortex, and ventral striatum, all involved in cognitive functions[3].

The hallmark of AD is the progressive accumulation of the protein fragment β-amyloid (plaques Aβ) outside neurons in the brain and of twisted strands of the protein tau (tangles) inside neurons.

Currently, six drugs are approved by the U.S. Food and Drug Administration (FDA) for the treatment of Alzheimer's: tacrine (discontinued in the United States due to potentially severe side effects), galantamine, rivastigmine, donepezil, memantine, and a drug that combines memantine and donepezil. They temporarily improve the AD symptoms by increasing the amount neurotransmitters in the brain but none of them slows down or stops the progression of AD.

All the "conventional" AD treatments are affected by several and severe side effects. In fact, they are characterized by poor solubility, unfavourable absorption by biological barriers, and toxicity to tissues, but also a difficulty to reach the central nervous system (CNS). [4]

Indeed, the efficacious delivery of therapeutic agents to CNS is currently a challenging task and not only for the treatment of neurological diseases. The main limitation is represented by the blood brain barrier (BBB), that is an overall area of 20 m^2 of brain capillary endothelial cells connected by tight-junctions (TJ). [5-8]

The BBB is a semipermeable selective membrane that provides the brain with the required nutrients and necessary agents while protecting it from foreign organisms, noxious chemicals and other harmful substances present in the blood stream.

Thus, strategies to reach the brain, which can either facilitate a non-invasive and non-toxic permeation of the BBB or bypass it have to be developed. Many attempts have been done to this aim by using: i) polymeric or lipidic colloidal carriers [9]; ii) chimeric peptides/drugs [10,11] obtained by coupling the otherwise non-transportable drug to a transporter protein by a disulfide bond that, after endocytosis by the endothelial cells or binding to the receptor, is cleaved by redox enzymes releasing the drug; and iii) cell-penetrating peptides, a class of peptides discovered in 1994 that can assist the release of hydrophilic macromolecules through the plasma membrane.[12-14] None of these approaches is fully satisfactory, due to induced toxicity, inefficient drug delivery [9-11] and limited understanding of the cellular uptake and penetration mechanisms.

A better understanding on the mechanism of AD pathogenesis in the last few decades has allowed the investigation of other possible treatments. In recent years, a growing body of evidence has shown an important role of insulin and insulin resistance in AD [15,16]. In fact, in healthy brain insulin and insulin receptors (IRs) are mainly localized in hippocampus and cerebral cortex, and are involved in learning and memory skills. From postmortem evaluation of AD patients brain, a decreased presence of IRs was observed that is a feature of insulin resistance. As a consequence, at molecular level, an impairment in insulin signaling and reduced activation of specific pathways involved in metabolism and growth is expected. Moreover, in vitro studies have demonstrated that activation of insulin signaling provides a neuroprotective mechanism to counteract oxidative stress, mitochondrial damage and neurodegeneration triggered by Ab oligomers in neuroblastoma cells. [17] All these evidences strongly encourage the insulin brain delivery as a potential treatment of AD. The administration of insulin to the brain is a hard challenge. In fact, its peripheral administration is not practicable owing to the risk of hypoglycemia.

A new therapeutic strategy is the normalization of brain insulin levels through intranasal administration. The olfactory and trigeminal nerve pathways, taking advantage of the exceptional direct connection between the nasal cavity and the brain

structures and bypassing almost completely the BBB. [18] In 2004, Benedict et al. for the first time demonstrated in a clinical trial that 8-week intranasal insulin administration significantly improves the brain functions of the treated AD patients, compared to placebo treated ones, while leaving unmodified their blood glucose level [19] Clinical studies have demonstrated that insulin administration to mild cognitive impairment or mild to moderate AD affected patients improves their cognitive performances. [20,21]

If on one hand the intranasal route appears to be preferable for administering insulin to the brain, since it bypasses the BBB, avoids the first pass through the liver and the systemic bloodstream dilution and reduces the delivery of the drug to non-targeted sites [22-25], on the other hand, it is characterized by several limitations.

In particular, the main limitations are (i) low bioavailability because of several biological barriers across the nasal mucosa; (ii) rapid clearance from the olfactory epithelium due to the mucociliary mechanism; (iii) degradation for the presence of degrading enzymes in the mucus; (iv) small administered volumes; (v) damage of the nasal mucosa.

For all these reasons, new approaches to improve the i.n. absorption of insulin and its delivery efficiency to the brain are necessary. To this aim, the topic of this chapter is to show the potential of conjugating insulin to PVP-based nanogel. In particular, insulin molecules were covalently attached to NG and subjected to several physico-chemical characterizations to determine the conjugation degree, the hydrodynamic size and size distribution, and surface electric charge density. Colloidal stability tests were also conducted investigating several storage conditions and possible medium-triggered aggregation phenomena. Finally, NG-insulin conjugated systems were biologically evaluated both *in vivo* and *in vitro*.

4.2 Experimental

4.2.1 Materials

Poly(N-vinyl pyrrolidone)-co-acrylic acid (PVP-co-AA) nanogels (NG) (for more details see 3.2.2), human insulin HEPES solution (In, 10 mg mL^{-1}), human insulin labeled with fluorescein isothiocyanate (FITC), (In^{FITC}), 2-(N-morpholino) ethanesulfonic acid hydrate (MES), 1-ethyl-3-[3-dimethylaminopropyl] carbodiimide hydrochloride (EDC), N-hydroxysulfosuccinimide sodium salt (Sulfo-NHS). All chemicals were purchased from Sigma Aldrich and used as received.

4.2.2 Preparation of NG-In conjugated variants

Conjugation of In and In^{FITC} on NG (NG-In and NG- In^{FITC}) was carried out promoting the formation of an amide bond between the carboxyl group of NG and the primary amino group of insulin. In particular, a two steps EDC/Sulfo-NHS protocol was adapted (more details in Appendix A.7).

In order to find the optimal reaction conditions, several reaction parameters were investigated: the molar ratio of insulin to NG carboxyl groups, pH and reaction time. In Tab. 4.1, details on the investigated parameters for NG-In conjugation are provided. In general, a given volume of NG aqueous dispersion, was mixed with EDC and Sulfo-NHS aqueous solution (MES, pH =5.5 or isotonic PBS, pH =7.4) for a given time, then known volumes of In or In^{FITC} were added, corresponding to various In/NG carboxyl groups ratios (see Tab 1). The reaction was conducted for further 4 (or 6 or 24) hours under gentle stirring. In order to remove unreacted reagents, NG-In conjugated variants were purified through 7 days dialysis against MilliQ water or isotonic PBS, using 100 kDa cut-off membrane. For a selected NG-In conjugated system, dialysis was also performed using a 300 kDa cut-off membrane. Synthesis and purification steps were conducted under dark conditions at room temperature.

Table 4.1. Investigated conjugation reaction parameters

	NG COOH groups /In ratio	Buffer-pH	Duration step (I-II), h	Dialysis medium
NG-In conjugated systems	0.1	MES-5.5	0.5 - 4	MilliQ water
	0.5	MES-5.5	0.5 - 4	MilliQ water
	1	MES-5.5	0.5 - 4	MilliQ water
	1	PBS-7.4	0.5 - 4	PBS-7.4
	1	PBS-7.4	0.5 - 6	PBS-7.4
	1	PBS-7.4	2 - 6	PBS-7.4
	2	PBS-7.4	0.5 - 6	PBS-7.4
	10	PBS-7.4	0.5 - 6	PBS-7.4

The conjugation degree, defined as molecules of insulin per NG, was estimated by UV-VIS absorption spectroscopy on the NG-In^{FITC} variants at $\lambda_{(max\ Abs)}$= 480 nm (Jasco V 670 spectrophotometer at room temperature, scan-speed 100 nm min^{-1}, band width 1 nm). In Fig 4.1 a calibration curve was built plotting the absorbance at peak as a function of In^{FITC} concentration.Furthermore, the conjugation degree of NG-In systems was also estimated using an enzyme-linked immunosorbent assay (ELISA) based human insulin assay kit (Mercodia AB, Uppsala, Sweden).

For selected reaction conditions, two type of control “conjugations” were performed: one without EDC/Sulfo-NHS reactants, and the other without insulin. Characterization of solutions eluted from 100 kDa cut-off centrifuge-filtered NG-In^{FITC} suspensions was performed by both UV-vis absorption and fluorescence spectroscopy (JASCO FP-6500 spectrofluorimeter equipped with a Xenon lamp, λ_{exc}=480 nm, λ_{em}=520 nm).

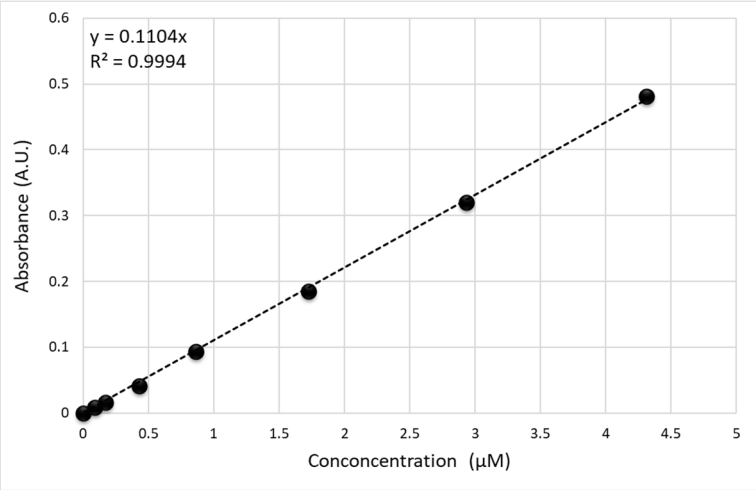

Figure 4.1. Calibration curve of insulin^{FITC}

4.2.3 Physico-chemical characterizations of NG-In systems

Dynamic Light Scattering analysis (DLS)

The hydrodynamic dimension of the conjugated NG-In variants were estimated by DLS measurements (for more details see Appendix A.1). Before the measurement, all the samples were diluted to a concentration of 0.05 wt% to avoid multiple scattering and filtrated with 0.45 μm syringe filters to remove impurities. In consideration of their monomodal size distribution, DLS data were analyzed according to the method of cumulants [26] and represented in terms of average hydrodynamic diameter (D_H) and width of the size distribution.

Measurements were carried out in triplicate on samples from minimum two different production batches with excellent reproducibility.

ζ-potential measurements

Net surface electric charge of NG-In variants was measured by ζ-potential analysis at 25 °C on systems previously dialyzed against Milli-Q water and diluted to a final

concentration of 0.05 wt%. All the systems were characterized by a monomodal ζ-potential distribution. More details are reported in Appendix A.4.

Gel Filtration Chromatografy (GFC)

Gel filtration chromatography measurements were performed on selected batches after purification process. In particular, purification was performed using both 100 and 300 kDa cut-off membranes, both against milliQ water and isotonic PBS. For more details see Appendix A.3.

4.2.4 Stability studies

Naked and NG-In conjugated systems were subjected to stability studies upon storage at 4°C and 25°C over a period of three months. The NG-In conjugated systems were stored both as colloidal dispersions and freeze-dried solids (in the presence of saccharide (6 wt % as cryoprotector). The 3 months-aged dispersions and solids redispersed in PBS buffer at two different concentrations (3.2 and 1.6 mg mL^{-1}) were characterized by DLS and ζ-potential measurements.

The colloidal stability of a selected NG-In system was also investigated in the presence of serum proteins. In particular, NG-In samples, previously filtered with a 0.45 μm cut-off syringe filter, were incubated with fetal bovine serum (FBS, 10% vol) at 37°C for 24 hours. DLS measurements were then performed at 25±0.1 °C and at 90° scattering angle. Because of FBS absorption at the laser wavelength (λ=532 nm), samples were diluted with isotonic PBS to the final concentration of 0.025 wt% and analyzed without filtration.

4.2.5 Morphological analysis of NG-In

The morphology of NG-In conjugated system, previously dialysed in MilliQ water, was investigated by Scanning electron microscopy (SEM) and Transmission electron

microscopy (TEM) techniques. More details are reported in Appendix A.5.

4.2.6 Biological evaluations

Insulin-conjugated NGs variants were subjected to *in vitro* and *in vivo* biological evaluations. In particular, the following aspects have been investigated: (i) assessment of the biological activity of insulin conjugated to the nanogel: ability to bind its receptor and activate the signaling cascade *in vitro*; (ii) NG-In ability to play a neuroprotective role on LAN5 cells (neuroblastoma cells) in the presence of amyloid-β peptide, *in vitro*; (iii) NG-In ability to cross the BBB *in vitro*; (iv) NG capacity to protect insulin by enzymatic degradation *in vitro*; (v) insulin biodistribution in the brain after NG-In intranasal administration; (vi) insulin signaling activation after NG-In intranasal administration. A detailed description of the methods is reported in Appendix B2.

4.3 Results and discussion

4.3.1 Synthesis of insulin-decorated nanogel

Characterization of the nanogel used as substrate

The final aim of this work is to synthetize a nanoscalar substrate that can incorporate, protect and vehicle insulin to the brain to overcome the limits of the intranasal administration of "free" insulin. For this purpose, a carboxyl-functionalized poly(N-vinyl pyrrolidone) nanogel system was identified as possible substrate for the covalent attachment of insulin. The bio-hybrid, insulin-conjugated nanogel is expected to have both colloidal and chemical stability in aqueous solution. Colloidal stability should be ensured by the small hydrodynamic size, high hydrophilic character, and the net surface electric charge. The chemical stability should be granted by the covalent nature of both the polymer network and insulin to nanogel linkage and should avoid any interference by the degradation products. The bond to the soft and dynamic

structure of the nanogel should ensure protection of the hormone from enzymatic degradation in its journey to the site of action, yet enabling its interaction with insulin receptors that, in turn, activate the signalling cascade. Furthermore, the presence of several residual (non used for the conjugation reaction) carboxyl groups in the nanogel may allow the nanocarrier to cross the BBB. [27] Renal clearance of the nanogels is considered a possible mechanism of elimination of NG-In.

After synthesis and purification by dialysis, the aqueous dispersions were characterized for the average hydrodynamic diameter by Dynamic Light Scattering (DLS) and surface electric charge density by ζ-potential measurements. The values of hydrodynamic diameter and zeta potential, are the result of the average of three measurements from samples belonging to three different irradiation batches. The systems are highly reproducible in their characteristics, the errors provided in the table representing the width of size and surface electric charge distributions.

Development of insulin conjugation protocols

The conjugation of insulin variants (In and In^{FITC}) to NG were performed by promoting a covalent attachment through an amide bond between the carboxyl groups of NG and one of the three N-terminal primary amines of insulin. As already described in 4.2.2, several reaction parameters were investigated (Tab 4.1).

With this aim, FITC-labeled insulin-NG conjugated variant (NG-In^{FITC}) was employed and characterized in terms of hydrodynamic diameters and conjugation degree (molecules of $insulin^{FITC}$ per NG). The conjugation degree was estimated on NG-In^{FITC} through UV-vis absorbance measurements exploiting FITC absorbance at 480 nm and taking into account the Mw of NGs and the polymer concentration of the purified conjugated system.

The average hydrodynamic diameters and conjugation degrees of NG-In^{FITC} systems obtained varying selected reaction parameters are shown in Tab 4.2. When the conjugation was performed at pH 5.5 (MES), for all the three investigated NG carboxyl groups/insulin molar ratios an increase of average hydrodynamic diameters

occurred. In particular, for the highest amount of insulin used the hydrodynamic dimensions of the conjugate almost reached the microscale. In fact, the reaction in MES was carried out at a pH close to the protein isoelectric point (pH=5). Probably, at this pH insulin homopolymerizes/aggregates and, when present at higher concentrations, also acts as a "bridge" between NGs.

A second set of conjugations was carried out at pH 7.4 (i.e. above the isoelectric point of insulin), using isotonic PBS and with stoichiometric or understoichiometric amounts of insulin with respect to the NG carboxyl groups. Since at this pH EDC and Sulfo-NHS mediated activation of the carboxyl groups is slower [28], longer reaction times were investigated.

In general, as shown in Tab 4.2, the NG-In^{FITC} systems prepared at pH 7.4 are characterized by hydrodynamic diameters that are only slightly bigger than the "bare" NG one. With reference to the preparations with "NG-COOH/In^{FITC} molar ratio" equal to 1, D_H and conjugation degree increase with the duration of the second step. Conjugation reactions performed with insulin in understoichiometric ratio are characterized by a decreasing number of conjugated insulin per NG.

In general, as shown in Tab 4.2, low yields of reaction were always obtained. The causes can be several: the relative low molar concentration of insulin and nanogels in the system (10 μM and 0.2 μM, respectively); the low reactivity of carboxyl groups at the chosen pH; the difficult accessibility of part of the carboxyl groups; insulin/NG electric charge repulsions (both negative at the reaction pH) and steric restrictions.

Among all the synthesized NG-In^{FITC} systems, the two systems produced in PBS, with CD=4 and CD=8 were selected for a preliminary biological test and, unlabeled-insulin NG conjugated variants (NG-In) were produced under the same reaction conditions.

In particular, the ability of NG-In to interact and bind to its receptor was evaluated through a binding assay (Western Blot, see Appendix B). Between the two variants, the highest biological response was observed for the NG-In^{FITC} with a CD=4. The lower biological activity of the system with CD=8, despite of the higher conjugation degree, may be due to partial insulin denaturation/aggregation, possibly caused by

stirring, as suggested by DLS analysis carried out on pure insulin solutions subjected to the same prolonged stirring treatment (with no NG, EDC and sulfo-NHS) (data not shown). The system NG-In^{FITC} with a CD=4 was further investigated.

Table 4.2. Average hydrodynamic diameter (D_H), conjugation degree (CD) and reaction yield (RY) of NG-In^{FITC} variants on varying the reaction conditions.

	NG-COOH /In^{FITC} ratio	**Buffer-pH**	**Duration step (I-II) h**	**D_H, nm**	**CD**	**RY, %**
NG	/	/	/	67 ± 21	/	/
NG-In conjugated systems	0.1	MES-5.5	0.5 - 4	800 ± 570	n.a	n.a.
	0.5	MES-5.5	0.5 - 4	138 ± 36	20	n.a.
	1	MES-5.5	0.5 - 4	127 ± 35	6	15
	1	PBS-7.4	0.5 - 4	85 ± 26	2	5
	1	PBS-7.4	0.5 - 6	92 ± 25	4*	10
	1	PBS-7.4	0.5 - 24	115 ± 38	8*	20
	2	PBS-7.4	0.5 - 6	82 ± 24	2	10
	10	PBS-7.4	0.5 - 6	79 ± 25	0.5	10

As reported in Chapter 3 (see 3.3.1), the selected NG have both carboxyl groups and primary amino groups. In order to rule out a possible EDC/Sulfo-NHS mediated NG coupling reaction, a "control synthesis" was performed in the same conditions used for insulin conjugation (i.e. in the presence of EDC and Sulfo-NHS) but without insulin. The reactive mixture was analysed by DLS measurements every 3 minutes for 30 minutes. The corresponding autocorrelation function of the scattered light intensity are reported in Fig 4.2. Since all the decay curves overlap, there is no change in the hydrodynamic dimension of the nanogel. Therefore, NG coupling can be excluded, probably thanks to steric hindrance.

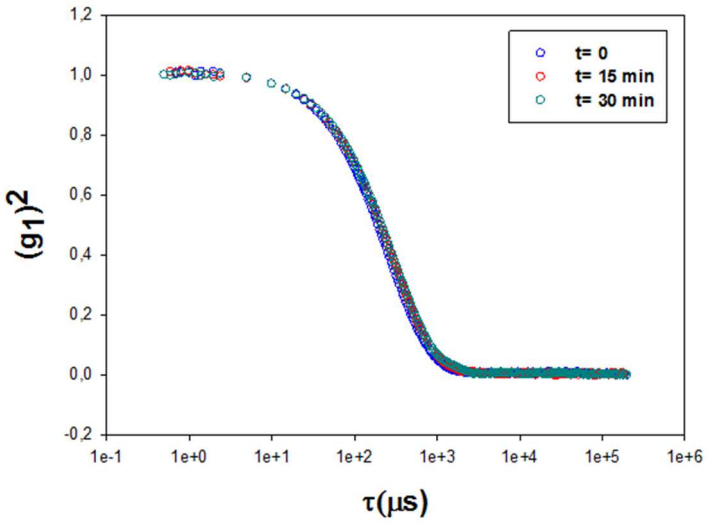

Figure 4.2. Autocorrelation function of the scattered light intensity of NG in the presence of EDC and Sulfo-NHS. The measurements were acquired every 3 minutes for a duration of 4 hours.

In order to exclude the presence of smaller insulin aggregates (not "visible" to the DLS analysis) in the purified NG-In^{FITC} system, the influence of different purification procedures was investigated. In particular, the effect of two dialysis membrane cut-offs (100 and 300 kDa), Milli-Q water and PBS buffer as dialysis media were considered. Recovered samples were subjected to both DLS and GFC analyses.

Expectedly, from DLS measurements no appreciable changes in the hydrodynamic size was detected. In Fig 4.3 the chromatograms of the four differently purified variants are reported. Also this analysis does not evidence significant differences among the systems, therefore the more robust 100 kDa cut-off membranes were selected to be routinely used for the purification of the NG-In^{FITC} systems. Isotonic PBS was generally used as dialysis medium unless otherwise specified.

In conclusion, the system with CD=4 purified 100 kDa cut-off dialysis membranes was selected for further studies and biological evaluations. The same reaction and purification conditions were applied to produce the NG-In variant. The conjugation

degree was estimated with the ELISA assay, resulting to an average number of 4-5 insulin molecules per nanogel, in good agreement with the CD obtained for the nanogel conjugated to the labeled protein. Being ELISA an antibody affinity test, the result also confirms that the conjugated insulin molecules are able to interact with their antibody also if bonded to the NG.

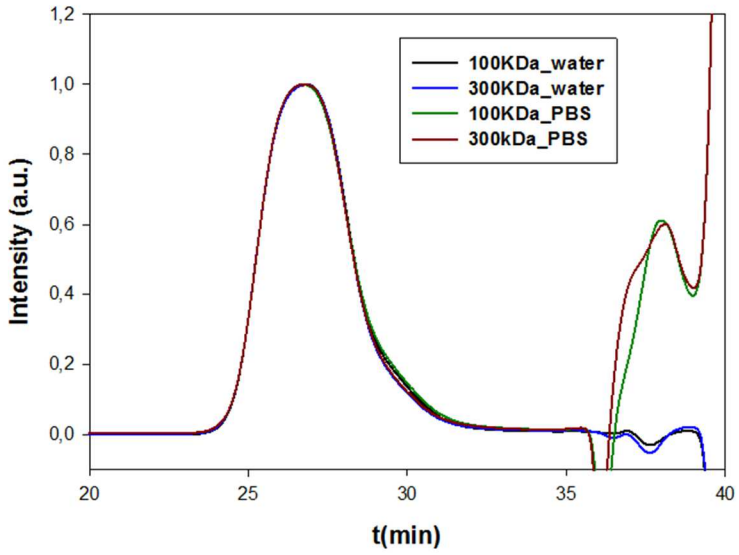

Figure 4.3. Hydrodynamic volumes distributions of NG-In systems dialyzed with 100 and 300 kDa cut-off membrane against Milli-Q water or isotonic PBS.

Morphological characterizations of the insulin-decorated nanogel

In order to investigate the morphology of NG-In system, SEM and TEM analysis on air-dried samples were carried out. In Fig 4.4 the related results are shown. It can be observed that NG-In is characterized by a uniform particle size distribution. It is worth

mentioning that these techniques imply air-drying, probably causing a collapse of the 3D structure of the soft nanogels.

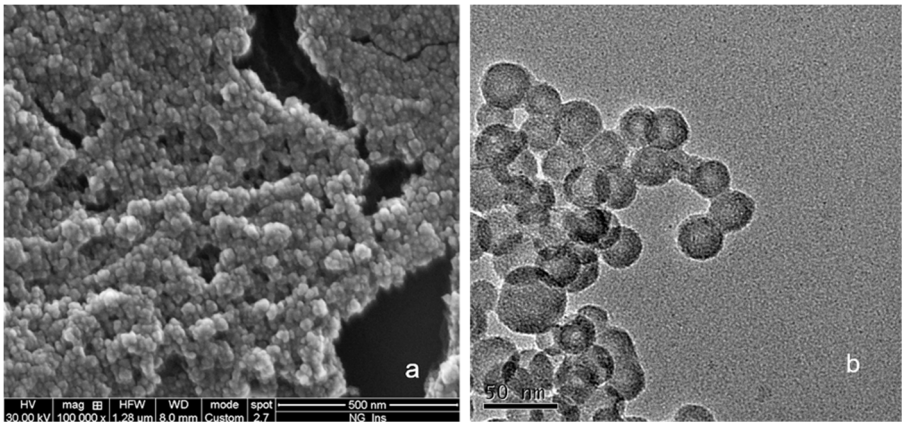

Figure 4.4. SEM (a) and TEM (b) analysis on NG-In [29]

Stability studies

In order to test the strength of the insulin-to-NGs bond and ascertain that the detected insulin was actually chemically attached and not only physically adsorbed, two sets of "conjugations" of In^{FITC} were simultaneously carried out: one with and one without EDC and sulfo-NHS. Dialysis was conducted against isotonic PBS (pH 7.4) for 7 days both at room temperature and at 37°C. Once the purification process was completed, the residual amount of In^{FITC} in the system with no activators resulted lower than 2% of the initial amount. The two "conjugated" systems were then centrifuge-filtered (100 kDa cut-off membrane) and the eluted solutions were subjected to UV-vis absorption and fluorescence analysis. In both cases, no signal referring to In^{FITC} release was detected.

In order to test if a change in the medium composition could trigger insulin release, both systems were incubated with the cell culture medium for 3 h at 37°C (1:1 volume ratio). Then, they were centrifuge-filtered as described above and no In^{FITC} was

detected in either of the eluted systems, by both UV-vis absorption and fluorescence spectroscopy. All together, these findings indicate that no insulin is released by the purified NGs (within the limitations of the detection methods) and that only a minor part of insulin is eventually physically, yet irreversibly, entrapped.

The colloidal stability of the NG-In under different conditions was also investigated. In particular, the storage stability of naked and insulin-decorated nanogels in the physical form of aqueous dispersions and freeze-dried solids in the presence of a cryoprotector was tested over three months storage, both at 25 °C and 4 °C. Data are reported in Table 4.3. The hydrodynamic dimensions of both bare and NG-In aqueous dispersions did not appreciably change at both temperatures. The solids were redispersed in PBS at two concentrations (1.6 mg mL^{-1} and 3.2 mg mL^{-1}). While the naked nanogels showed an increase of hydrodynamic size and slight reduction of surface charge, probably to association of carboxyl groups in the dry state, the insulin-conjugated variants returned to their original size and surface charge density.

In order to rule out aggregation of NG-In conjugated systems in the presence of serum proteins, NG-In was incubated for 24 hours at 37 °C with fetal bovine serum (10 % v/v). The hydrodynamic size and width of size distribution resulted equal to 95 ± 38 nm. Comparing this value with value obtained before NG-In incubation, it can be observed essentially only a slight increase in size distribution. This result suggests that no irreversible aggregation phenomena occur.

Table 4.3. Hydrodynamic diameter (D_H) and ζ-potential values for naked and insulin-conjugated NGs after three months storage at two temperatures as aqueous dispersions or freeze-dried solids (upon redispersion in PBS). [29]

System	Storage Conditions		Polymer Concentration (mg mL^{-1})	D_H (nm)	ζ-potential (mV)
	Temperature(°C)	Physical form			
NG	25	Dispersion	5	65±21	-29±5.6
NG	4	Dispersion	5	63±19	-31±4.2
NG-In	25	Dispersion	1.6	93±24	-27±6.7
NG-In	4	Dispersion	1.6	93±24	-28±6.5
NG	25	Freeze-dried solid	1.6	120±24	-20±10.0
NG	4	Freeze-dried solid	1.6	118±15	-18±7.5
NG-In	25	Freeze-dried solid	1.6	93±24	-26±6.8
NG-In	4	Freeze-dried solid	1.6	93±24	-27±6.4
NG-In	4	Freeze-dried solid	3.2	112±30	-25±6.9

4.3.2 Biological evaluation of insulin-decorated nanogel

NG protection of insulin by protease degradation

One of the obstacles of peptide-based therapies is the degradation by enzymes present in the biological fluids. Indeed, the peptides are often not systemically stable without modification. [30] To evaluate whether NGs are able to shield insulin by protease degradation, an *in vitro* assay was performed. Proteinase K, an enzyme having different cleavage sites in insulin-A and -B chains was utilized. NG-In^{FITC} and free In^{FITC} were incubated with proteinase K. After filtration (3 kDa cut-off), the released fluorescence following insulin degradation was measured (Fig. 4.5). The proteinase K treatment causes a 63% (± 1.6) of degradation of free insulin in contrast to the 12% (±1.3) obtained in the case of NG-In suggesting that NG could provide insulin protection against protease degradative attack, allowing its safe delivery to the target site. The protective effect of the nanogel towards insulin degradation is probably due to the ability of the flexible polymeric structure to rearrange and conform differently in different environments. In particular, it can be speculated that in aqueous solution the nanogel can offer transient hydrophobic pockets where insulin can be hosted and protected, as already observed for similar macrogels. [31,32]

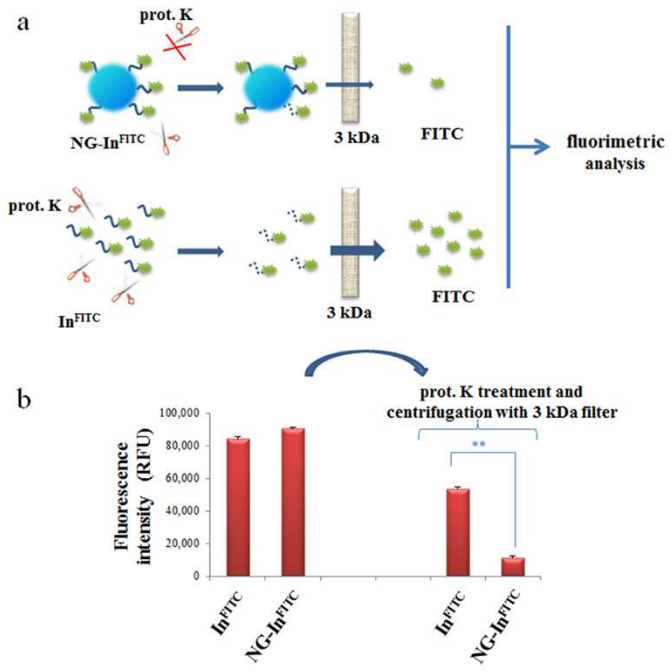

Figure 4.5. NG protects insulin by protease degradation**.** A) Schematic representation of a model of proteinase K (prot.K) resistance in vitro assay. B)NG-In^{FITC} and In^{FITC} were incubated with proteinase Kand, after filtration, the fluorescence intensity (expressed as Relative Fluorescence Units, RFU) of the samples was detected and represented in the histogram. **p< 0.02, vs. indicated groups. [29]

NG-In biological activity

Insulin Receptor (IR) is a transmembrane tyrosine-kinase receptor that is activated by insulin binding. To assess the ability of NG-In to bind to IR a binding assay on LAN5 cell line (neuroblastoma cells) was performed. Total LAN5 proteins and Bovine serum albumin (BSA), as negative control of specificity, were spotted on nitrocellulose membranes and incubated with NG-In^{FITC}, In^{FITC}, and PBS as control (vehicle). A fluorescent signal was detected both for NG-In^{FITC} and In^{FITC} indicating

that a binding was occurred (Figure 4.6-a). Similarly, a Western blot of total LAN5 proteins was incubated with NG-In^{FITC} and In^{FITC} and a fluorescent band of 130 kDa, corresponding to the molecular weight of the IR α subunit, was detected (Figure 4.6-b). However, a clearcut result was obtained by an immunofluorescence experiment. LAN5 cells treated with NG-In^{FITC} were fixed and incubated with anti-phospho-IR. The merged images show a colocalization of NG-In^{FITC} with activated IR, demonstrating that the insulin was correctly delivered to its target (Figure 4.6-c).

Insulin in brain, rapidly binds to IRs, which are highly abundant, but differently distributed throughout CNS especially in olfactory bulb, hypothalamus, cerebral cortex, cerebellum and hippocampus. [33] Further, intracellular IRs are especially expressed in synapses that are impaired in age-related disorders such as AD. [34] To confirm that NG-In activates the downstream signaling by binding to its receptor, both free insulin and NG-In were administered, at different times, in LAN5 cell cultures and the presence of phosphorylated Akt, a key molecule in insulin pathway, was measured. [17]. Free insulin activates Akt, 30 minutes after its addition in the cell culture, and reaches its peak 1 hour after administration, then it begins to decrease. Insulin conjugated to the NG activates Akt 1h after addition to cell culture and it reaches its maximum effect on Akt after 3 h from its addition. Furthermore, the activation level obtained in the case of NG-In is almost twice respect to the free insulin (Figure 4.7).

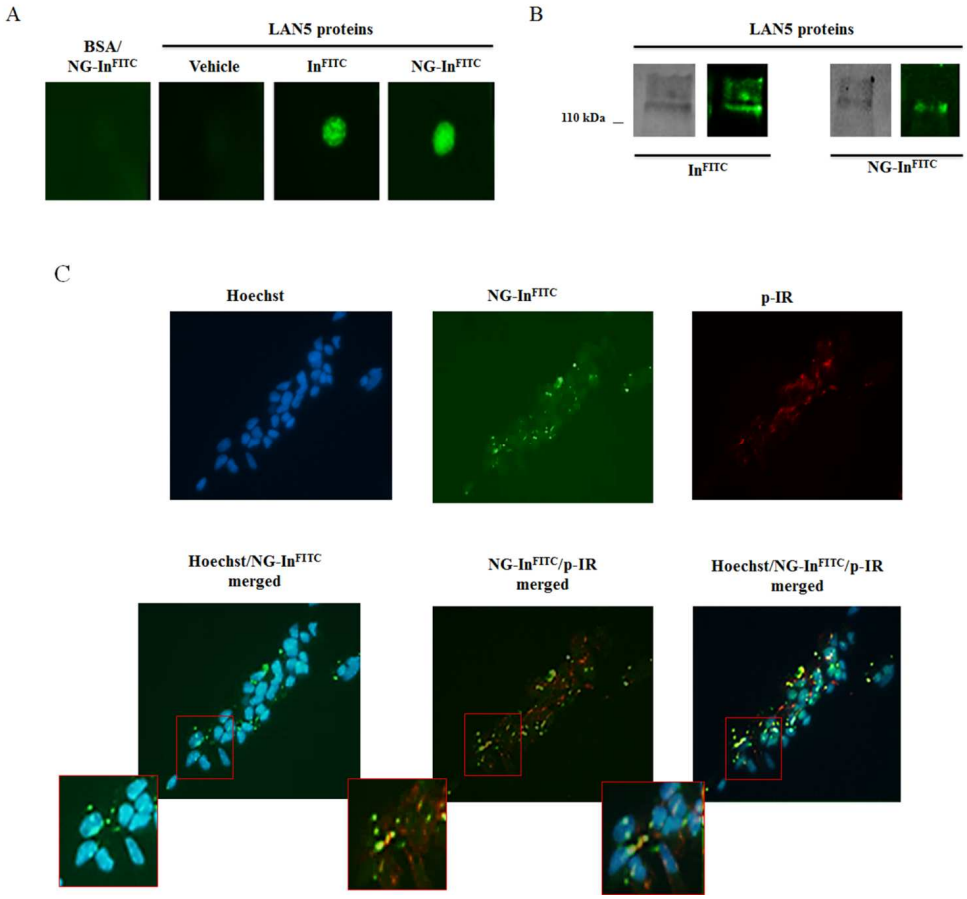

Figure 4.6. NG-Insulin binds and activates the insulin receptor. A) Dot-blot of total LAN5 proteins or BSA stained with and without NG-In^{FITC}and In^{FITC}. B) Western blot of total LAN5 proteins incubated with NG-In^{FITC}and In^{FITC}. C)Immunofluorescence of LAN5 treated with NG-In^{FITC} and incubated with anti-phosphorylated Insulin Receptor (p-IR)(red fluorescence) and Hoechst (blue fluorescence). Splitted, merged and highmagnification images of the same sample are shown. [29]

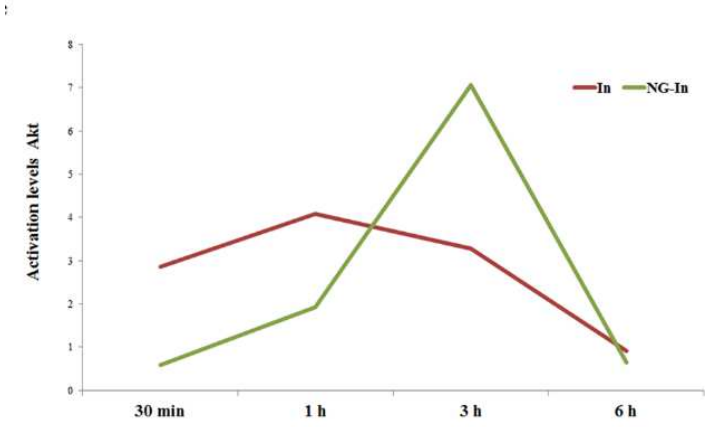

Figure 4.7. Akt activation levels in LAN5 cells treated with In and NG-In at different times. *p< 0.05, **p< 0.02, vs. indicated groups. Adapted from [29]

These results indicate that NG-In needs a longer time to be effective on Akt signaling with respect to the free insulin and this retard in signaling activation could be due to the slower diffusion of the NG-In binding to the receptors. This delay in the effect could have the positive consequence of reducing the occurrence of signaling activation before the insulin reaches brain, thus preventing its undesired effect in other districts. Moreover, it cannot be excluded that the increased signaling activation by NG-In could be due to the larger number of insulin molecules carried simultaneously on the membrane micro-domain where the IRs are present.

NG-In neuroprotective role

The final goal is the transport of insulin to brain where it can play a neuroprotective and probably also a therapeutic role. [35] Indeed, insulin in CNS controls important events related to metabolism, neuronal plasticity and cognition, mechanisms impaired in AD. With this aim, the effect of NG-In in presence of Aβ was tested. LAN5 cells were exposed to Aβ alone, Aβ and NG, Aβ and In, Aβ and NG-In, and submitted to cell viability assay and microscopic morphological inspection. As shown in Fig 4.8, the toxicity caused by Aβ was almost completely recovered when NG-In was supplemented in the cell culture, compared with non-treated cells. No protective role was played by NG alone with respect to Aβ treatment.

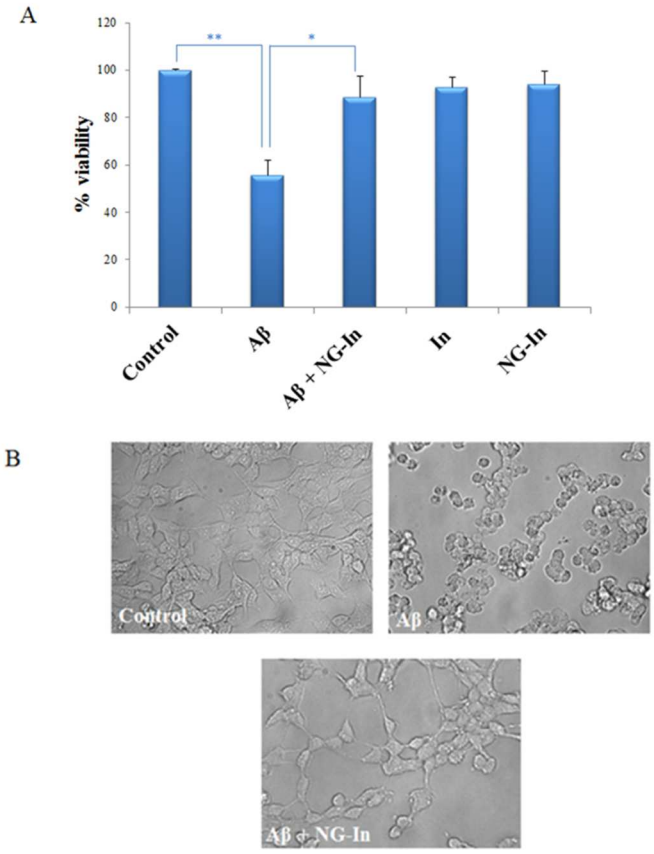

Figure 4.8 A) LAN5 untreated (Control) and treated with Aβ, Aβ+NG-In, Insulin (In) and NG-In, for 24 h and submitted to MTS assay. B) Representative morphological images of LAN5 cells. [29]

NG-In ability to cross the BBB

In order to evaluate the transport efficiency of the NG-In system across the BBB, mouse brain endothelial cells (bEnd3) cultured on transwell inserted within a chamber were used as suitable model for studying solute and particle transport across the BBB. Observed by a confocal microscope, the brain endothelial cells showed a regular-shaped morphology, proving them to be an appropriate model for the purpose of testing the interaction between BBB and NG-In (Figure 4.9-a). Once cell junctions were developed, In^{FITC}, NG-TRITC, NG-In^{FITC} and sodium fluorescein (NaFluo), a molecule that is not able to across the BBB [36], were loaded into the donor chamber of the transwell insert. Small amounts of the sample were removed from the acceptor chamber at different time intervals (30, 60, 90 and 120 minutes) and fluorescence signal was measured (Fig. 4.9-b). The intensity of fluorescence signal increased in In^{FITC}, NG-TRITC, NG-In^{FITC} samples in a time dependent manner. No significant increase of the signal in time was detected for NaFluo, thus confirming the integrity of the barrier. These results indicate that NG-In can be efficiently transported across the BBB, and the number of protein molecules that can be transported is greater for the conjugated insulin than for the free one (Fig 4.9-c).

One possible mechanism for the BBB permeation is through of opening the tight junctions. [27] Anionic nanocarriers and, particularly the carboxylic acid functional groups at the extremity of the grafted arms of our NG system could efficiently chelate calcium ions, thus leading to the opening of the tight junction and hence increasing the permeability to NG-In. [27] NG-In appears to be capable of producing reversible paracellular transport. This could justify why the naked NG and a major number of insulin molecules conjugated to NG are transported across with respect to free insulin. Moreover, it cannot be excluded that the transport of NG-In could be also facilitated by the receptor-mediated endocytosis due to the presence of IRs existent in our *in vitro* and *in vivo* system. To have more information about the internalization pathway used by the nanogel, an experiment in which the insulin receptors of the bEnd3 were saturated by preincubation with an excess (75 μM) of free unlabeled

insulin was performed. After this treatment, NG-In^{FITC} and In^{FITC}, always in presence of free unlabeled insulin, were loaded into the transwell insert and the fluorescence measured at different times. The obtained results denote that In^{FITC} was unable to cross the *in vitro* performed BBB indicating that the receptor-mediated transcytosis mechanism was prevented (Fig. 4.9-d). In contrast, NG-In^{FITC} continued to cross the BBB signifying that it can utilize the paracelluar pathway. Finally, the purpose of this study was to develop a delivery system that could be utilized to administrate insulin utilizing the intranasal route.

The ability of our nanosystem to cross the BBB suggests that it could be efficiently utilized for this purpose.

Brain immunogenic response after NG treatment

Since the thought route of administration of NG-In is the intranasal route (i.n.), a potential inflammatory response 4 and 24 hours after NG intranasal administration was tested. Levels of IL-6, IL-1β, IL-10 and TGFβ (inflammatory markers in the brain) in mouse total brains were evaluated by ELISA assay. Results indicated that their concentrations were comparable to the controls (Fig. 4.10), suggesting that the i.n. administration of NG did not induce any inflammatory response

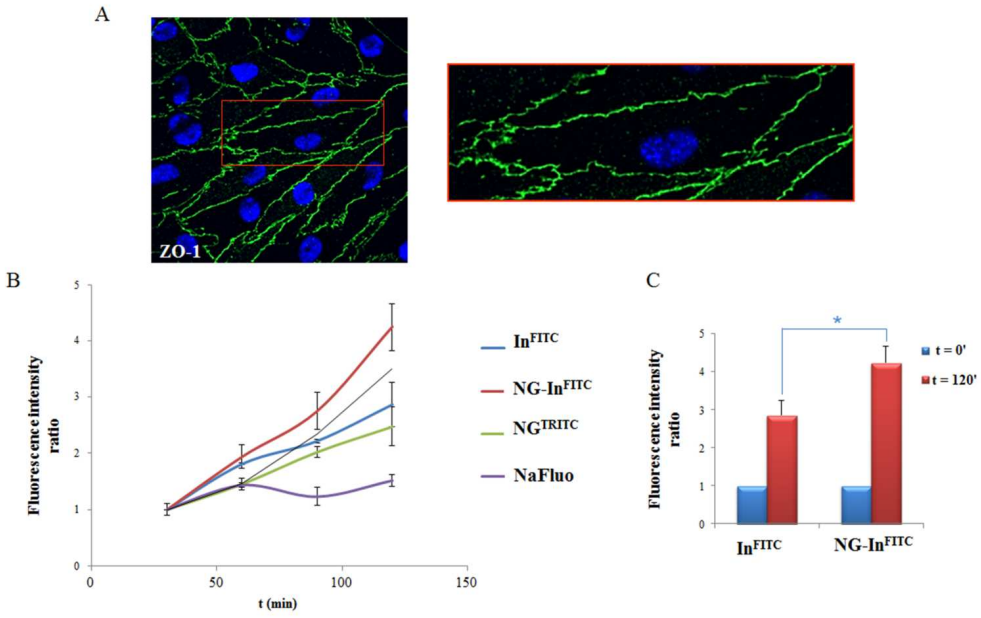

Figure 4.9. Capacity of NG to cross the BBB. a) 1024X1024 representative confocal image of bEnd3 cells immunostained with anti-Zonula Occludens-1 (ZO-1) and anti-rabbit Cy3-conjugate as secondary antibody (green fluorescence channel) and with Hoechst (blue fluorescence channel). b) Intensity fluorescence related to of NG-Ins^{FITC}, In^{FITC}, NG^{TRITC} and NaFluo, detected in the acceptor chamber at different times. c) In the histogram, the intensity fluorescence ratio of In^{FITC} and NG-In^{FITC} detected in the acceptor chamber, expressed as the ratio between fluorescence intensity measured at time t 120 min over the reference value. [5]

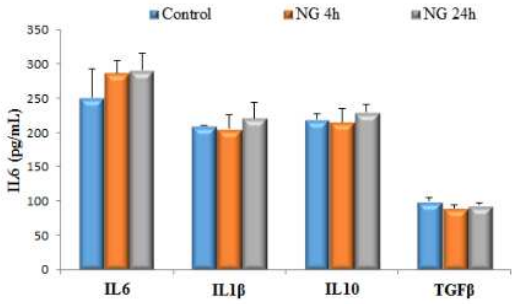

Figure 4.10. Signaling levels of IL-6, IL-1β, IL-10 and TGFβ obtained by ELISA assay after 4 and 24 h from i.n. inoculation of NG. Representative images from 2 animals for condition are shown. Each data point represents the mean ± SD of n = 5. Adapted from [37]

Efficiency of the mouse brain delivery of the NG-In via nasal route

It has been reported that insulin is a powerful drug against Alzheimer's disease and its nasal administration can be a promising treatment for the recovery of the pathological symptoms associated with the illness, such as memory deficit and recognition [20, 21, 38-40]. Thus, a conjugation with a nanogel has been proposed to the purpose of improving the delivery of the protein in the brain through i.n. administration.

In order to track NG-In in the different areas of the brain, the same amount of free FITC-labeled insulin (In^{FITC}) and FITC-labeled insulin conjugated to the nanogel ($NG\text{-}In^{FITC}$) was injected in the nasal cavities of the mice and, 30 minutes after administration, the brain distribution was analyzed [41-43]. As reported by Kamei and coworkers [41], time corresponds to the maximum amount reached in the brain by free insulin. The delivery and distribution in the brain was detected by fluorescence measurement. In Figure 4.11-A, it has been shown that the insulin levels in the whole brain are higher in the case of $NG\text{-}In^{FITC}$. Moreover, the levels of insulin reaching each brain region, 30 min after intranasal injection, were represented (Fig. 4.11-B) as a heat

map generated on the basis of the data obtained from the quantitative fluorimetric measurements. Our results indicate that NG-In has higher concentration in the mouse brain with respect to free insulin suggesting that the nanogel enhances the insulin delivery.

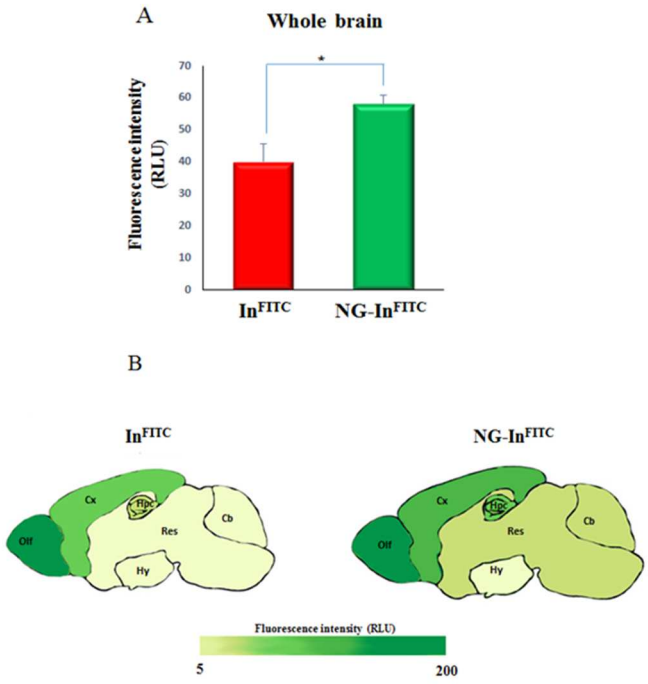

Figure 4.11. Brain biodistribution of In^{FITC} and NG-In^{FITC} after 30 minutes from i.n. administration. A) in the whole brain and B) Map brain indicating the levels of NG-In (right) in the olfactory bulb (Olf), cortex (Cx), hyppocampus (Hpc), hypotalamyus (Hy), cerebellum (Cb) and residual areas (Res) compared with the amount obtained for free Insulin in the same regions (left), 30 minutes after i.n. inoculation. Adapted from [37]

Literature data suggested that intranasal applied drugs could be transported into the brain mainly via both the olfactory and the trigeminal nerve pathways [44-46]. Our analysis has evidenced the presence of a significant amount of NG-In in the anterior

and cerebellar regions of the mouse brain. These results can be explained supposing that the olfactory and trigeminal nerve pathways are also involved when the insulin is conjugated with NG.

Insulin levels and effect of NG-In on the brain regions after intranasal administration

The insulin signaling starts by binding of the hormone to the α subunit of its receptor causing the activation of Akt, by its phosphorylation. The insulin localization in the different brain areas and its biological activity have been analyzed through detection of the levels of insulin and phosphorylated Akt at 30 and 60 minutes after free insulin and NG-In i.n. administration. Olfactory bulb, cortex and hippocampus were homogenized and supernatants and pellets were utilized for ELISA assay and Western blot analysis, respectively. ELISA assay showed that, both at 30 and 60 minutes, in the three investigated regions the insulin levels, in the case of NG-In, were enhanced if compared with those attained by free insulin at the same time (Fig. 4.12-A). These results were also confirmed by insulin (conjugated to NG) biological activity by Western blot analysis (data non shown). It is important to highlight that hippocampus and cerebral cortex are the areas devoted to learning and memory, mostly damaged in AD neurodegeneration. These data indicated that when conjugated to NG, insulin presented a more efficient brain delivery than free insulin and maintained its biological activity.

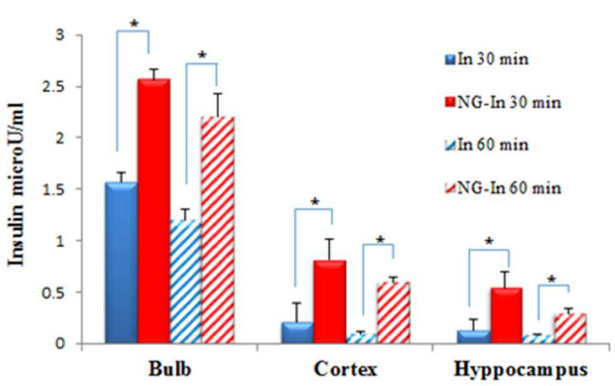

Figure 4.12. Free insulin and NG-In brain biodistribution and signaling activation. A) Level of free Insulin or Insulin conjugated to NG at 30 and 60 minutes from i.n. administration in the olfactory bulb, hippocampus and cerebral cortex obtained by ELISA assay. [37]

These results can be due to several factors. Among these, the already mentioned mucoadhesive property of PVP [47, 48], that constitutes a fundamental prerequisite for i.n. formulations. It cannot be excluded that this property could also be augmented by the addition of other mucopenetrating molecules in the formulation [49]. Moreover, it is known that the nasal cavity contains many different kinds of proteolytic enzymes and as already demonstrated that when linked to NG, insulin is more resistant to the action of proteolytic enzymes. Therefore, it can be supposed that the NG plays a protective role by hosting the insulin molecules in transitory hydrophobic pockets. [31,32]

The crossing of nasal epithelial barrier can occur through intracellular or paracellular pathways. [50] Intracellular pathway includes endocytosis into the olfactory neurons, as demonstrated for several viruses and proteins like peroxidases or albumin [50-52], or transcytosis phenomena across supporting cells to the lamina propria. In addition, the intracellular uptake by endocytosis and transcytosis across the epithelium into trigeminal nerve processes or basal lamina, respectively, have been observed [53,54].

Paracellular pathway, instead, is the main external transport mechanism that occurs through epithelial tight junctions [23], structures that are very similar to those ones present in the BBB. The use of absorption enhancers like the chitosan or lipophilic additives can increase the passage through this route [55]. A further possible reason explaining the increased delivery efficiency is the transient permeation through the tight junctions present in the olfactory and respiratory mucosae [23] due to the presence of negative charges [56]. Indeed, the carboxylic acid functional groups at the end of the grafted arms of our NG system could efficiently chelate calcium ions, thus allowing the passage of NG-In [56]. Furthermore, the negative coat promotes the delivery of the drugs to neurons rather than astrocytes or microglia [57,58] and this can validate the high delivery efficiency of the present formulation. In Fig 4.13-A the schematic representation of the insulin delivery routes is reported. In particular, it can be hypothesized that insulin, once conjugated to nanogel, is able to reach both the anterior and posterior brain areas through the olfactory and trigeminal pathways. Moreover, the capacity of the nanogel to cross the nasal epithelium is probably due to its mucoadesive properties, protease resistance and the ability of weakening the tight junctions and using the paracellular route (Fig. 4.13 B). Additionally, being the brain insulin transport through the nasal epithelium a saturable and carrier-mediated process [56, 59-61], the use of an alternative crossing mechanism like the paracellular route can be strategic, particularly in the case of long-term treatments. However, since the observed differences in insulin levels in the brain could also due to the different kinetics of diffusion, IR interaction and life-time of free and nanogel-delivered insulin, the effects of the treatment at both shorter and longer times will be investigated in the future.

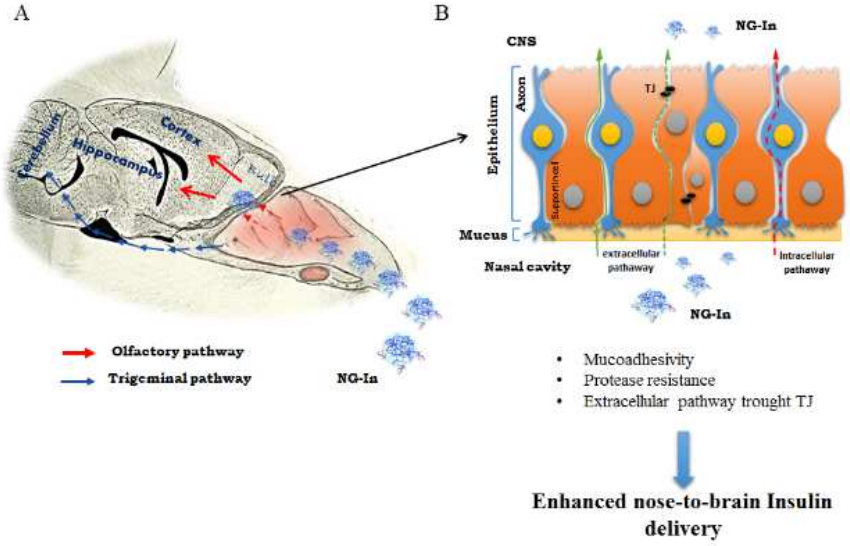

Figure 4.13. Scheme of the different routes leading from the nose to the brain in mouse**.** A) After penetrating the nasal cavity, NG-In can reach the brain through the trigeminal (blue) and olfactory (red) pathways. B) The NG-In is able to reach the CNS by both intracellular (red dashed) and extracellular (green) pathways due to its mucoadhesive and protease-resistance properties and the ability to the opening of the tight junctions (TJ) of the olfactory epithelium. [37]

4.4 Conclusions

The main objective of this work has been to synthetize a suitable nanocarrier that can incorporate, protect and vehicle insulin to the brain, after intranasal administration, for a potential application in the treatment Alzheimer's disease.

The engineered nanogel system shows a controlled hydrodynamic size (ca. 90 nm), high hydrophilicity and a negative surface charge density, which should guarantee good colloidal stability and resistance to opsonisation when entering the systemic circulation. Indeed, it was ascertained that NG-In is stable upon storage both as colloidal dispersion (in water and saline buffer) and freeze-dried solid, and also in the presence of serum proteins.

The biological characteristics of NG-In conjugate include (i) insulin protection against protease degradation; (ii) greater insulin activation signalling in comparison with free insulin; (iii) neuroprotective effect against the toxicity induced by amyloid peptide; (iv) major efficiency in the transport of insulin across the BBB model; (v) higher delivery in all tested brain regions compared with free insulin. These findings, together with the results obtained for “bare” NG, strongly support further evaluation of this nanocarrier as brain-targeted drug delivery system.

Acknowledgements

TEM experimental data were provided by Centro Grandi Apparecchiature e UniNetLab e Universita' di Palermo, funded by P. O. R. Sicilia 2000 e 2006, Misura 3.15, Quota Regionale.

This research was partially supported by a grant from the Italian Ministry of University and Scientific Research (PRIN 2010-2011 NANOMED), by the Università of Palermo "Fondo Finalizzato alla Ricerca (FFR) 2012/2013” and by the Italian Ministry of University and Research in the framework of the Flagship Project NonoMAX (n° B79E13000270005).

Collaborators’ contributions to the Chapter

Dr. Maria Antonietta Sabatino provided support for the design of some experiments and for DLS measurements.

Dr. Pasquale Picone (Istituto di Biomedicina e Immunologia Molecolare (IBIM) of National Research Council (CNR), Palermo, Italy) performed all the biological evaluations.

References

[1] H. Hippius, G. Neundörfer, The discovery of Alzheimer's disease, Dialogues Clin Neurosci. 5(1) (2003) 101–108.

[2] L.E. Hebert, J. Weuve, P.A. Scherr, D.A. Evans, Alzheimer disease in the United States (2010-2050) estimated using the 2010 Census. Neurology 80(19) (2013) 1778-83.

[3] W. A. Banks, Drug delivery to the brain in Alzheimer's desease: Consideration of the blood-brain barrier, Adv. Drug Del. Rev., 64, (2012) 629-639.

[4] B. Fonseca-Santos, M. P. Daflon Gremião, M. Chorilli, Nanotechnology-based drug delivery systems for the treatment of Alzheimer's disease, International Journal of Nanomedicine. (2015)

[5] L. Biddlestone-Thorpe, N. Marchi, K. Guo, C. Ghosh, D. Janigro, K. Valerie, H. Yang, Nanomaterial-mediated CNS delivery of diagnostic and therapeutic agents, Adv. Drug Deliv. Rev. 64 (2012) 605-613.

[6] Y. Chen, L. Liu, Modern methods for delivery of drugs across the blood–brain barrier, Adv. Drug Deliv. Rev. 64 (2012) 640-665.

[7] I. van Rooy, S. Cakir-Tascioglu, W.E. Hennink, G. Storm, R.M. Schiffelers, E. Mastrobattista, In vivo methods to study uptake of nanoparticles into the brain, Pharm. Res. 28 (2011) 456-471.

[8] M. I. Alam, S. Beg, A. Samad, S. Baboota, K. Kohli, J. Ali, A. Ahuja, M. Akbar, «Strategy for effective brain drug delivery» European Journal of Pharmaceutical Sciences, n. 40, pp. 385-403, 2010.

[9] J. Rautio, H. Kumpulainen, T. Heinbach, R. Oliyai, D. Oh, T. Jarvinene, J. Savolainen, Prodrugs: design and clinical applications, Nat. Rev. Drug Discovery 7 (2008) 255-270.

[10] C.-T. Lu, Y.Z. Zhao, H.L. Wong, J. Cai, L. Peng, X.Q. Tian, Current approaches to enhance CNS delivery of drugs across the brain barriers, Int. J. Nanomedicine 9 (2014) 2241-2257.

[11] E.M. Cornford, M.E. Cornford, New systems for delivery of drugs to the brain in neurological disease, Lancet Neurology 1 (2002) 306-315.

[12] S. Fawell, J. Seery, Y. Daikh, C. Moore, L.L. Chen, B. Pepinsky, J.

Barsoum, Tat-mediated delivery of heterologous proteins into cells, Proc. Natl. Acad. Sci. U.S.A. 91 (1994) 664–668.

[13] M. Mae, U. Langel, Cell-penetrating peptides as vectors for peptide, protein and oligonucleotide delivery, Curr. Opin. Pharmacol. 6 (2006) 509-514.

[14] D.M. Copolovici, K. Langel, E. Eriste, U. Langel, Cell-penetrating peptides: Design, synthesis and applications, ACS Nano 8 (2014) 1972-1994.

[15] S.M. De la Monte, J.R. Wands, Alzheimer's disease is type 3 diabetes – Evidence reviewed, J. Diabetes Sci. Technol. 2 (2008) 1101-1113.

[16] M. Di Carlo, G. Giacomazza, P. Picone, D. Nuzzo, S. Vasto, G. Accardi, C. Caruso, PL. San Biagio, A close connection: Alzheimer's disease and type 2 diabetes, Curr. Top. Biochem. Res. 14 (2012) 1-13.

[17] P. Picone, D. Giacomazza, V. Vetri, R. Carrotta, V. Militello, P.L. San Biagio, M. Di Carlo, Insulin-activated Akt rescues Aβ oxidative stress-induced cell death by orchestrating molecular trafficking, Aging Cell 10 (2011) 832-843.

[18] R.G. Thorne, G.J. Pronk, V. Padmanabhan, W.H. 2nd Frey, Delivery of insulin-like growth factor-I to the rat brain and spinal cord along olfactory and trigeminal pathways following intranasal administration, Neuroscience 127, (2004) 481-496.

[19] C. Benedict, M. Hallschmid, A. Hatke, B. Schultes, H.L. Fehm, J. Born, W. Kern, Intranasal insulin improves memory in humans, Psyconeuroendocrinology 29 (2004) 1326-1334.

[20] A. Claxton, L.D. Baker, A. Hanson, E.H. Trittschuh, B. Cholerton, A. Morgan, M. Callaghan, M. Arbuckle, C. Behl, S. Craft, Long-acting intranasal insulin Detemir improves cognition for adults with mild cognitive impairment or early-stage Alzheimer's disease dementia, J. Alzheimer's Dis. 44 (2015) 897-906.

[21] S. Craft, L.D. Baker, T.J. Montine, S. Minoshima, G.S. Watson, A. Claxton, M. Arbuckle, M. Callaghan, E. Tsai, S.R. Plymate, P.S. Green, J. Leverenz,

D. Cross, B. Gerton, Intranasal insulin therapy for Alzheimer disease and amnestic mild cognitive impairment: a pilot clinical trial, Arch. Neurol. 69 (2012) 29-38.

[22] S.V. Dhuria, L.R. Hanson, W.H Frey 2nd, Intranasal delivery to the central nervous system: mechanisms and experimental considerations, J. Pharm. Sci. 99 (2010) 1654–1673.

[23] J.J. Lochhead, R.G. Thorne, Intranasal delivery of biologics to the central nervous system, Adv. Drug. Deliv. Rev. 64 (2012) 614–628.

[24] J.P. Yang, H.J. Liu, S.M. Cheng, Z.L. Wang, X. Cheng, H.X. Yu, X.F. Liu, Direct transport of VEGF from the nasal cavity to brain, Neurosci. Lett. 449 (2009) 108-111.

[25] V. Jogani, K. Jinturkar, T. Vyas, A. Misra, Recent patents review on intranasal administration for CNR drug delivery. Recent patents on Drug Delivery & Formulation 2 (2008) 25-40.

[26] D. E. Koppel, Analysis of macromolecular polydispersity in intensity correlation spectroscopy: the method of cumulants, J. Chem. Phys. 57 (1972) 4814-4820.

[27] J. Mudassir, Y. Darwis, P.K. Khiang, Prerequisite characteristics of nanocarriers favoring oral insulin delivery: nanogels as an opportunity, Int. J. Polym. Mater. Polym. Biomater. 64 (2015) 155-167.

[28] G.T. Hermanson, Bioconjugate Techniques, Elsevier, London, UK, 3rd edition, 2013.

[29] P. Picone, L.A. Ditta, M.A. Sabatino, V. Militello, P.L. San Biagio, M.L. Di Giacinto, L. Cristaldi, D. Nuzzo, C. Dispenza, D. Giacomazza, M. Di Carlo, Ionizing radiation-engineered nanogels as insulin nanocarriers for the development of a new strategy for the treatment of Alzheimer's disease, Biomaterials 80 (2016) 179–194.

[30] B.J. Bruno, G.D. Miller, C.S. Lim, Basics and recent advances in peptide and protein drug delivery, Ther. Delivery 4 (2013) 1443-1467.

[31] M. Ricca, V. Foderà, D. Giacomazza, M. Leone, G. Spadaro, C. Dispenza, Probing the internal environment of PVP networks generated by irradiation with different sources, Colloid Polym. Sci. 288 (2010) 969–980.

[32] C. Lo Presti, V. Vetri, M. Ricca, V. Foderà, G. Tripodo, G. Spadaro, C. Dispenza, Pulsatile protein release and protection using radiation-crosslinked polypeptide hydrogel delivery devices, React. Funct. Polym. 71 (2011) 155–167.

[33] W. Zhao, H. Chen, H. Xu, E. Moore, N. Meiri, M.J. Quon, D.L. Alkon, Brain insulin receptors and spatial memory. Correlated changes in gene expression, tyrosine phosphorylation, and signaling molecules in the hippocampus of water maze trained rats, J. Biol. Chem. 274 (1999) 34893-34902.

[34] H. Sancheti, G. Akopian, F. Yin, R.D. Brinton, J.P. Walsh, E. Cadenas, Age-dependent modulation of synaptic plasticity and insulin mimetic effect of lipoic acid on a mouse model of Alzheimer's disease, PlosOne 8 (2013) e69830.

[35] P.I. Moreira, M.S. Santos, C. Sena, R. Seica, C.R. Oliveira, Insulin protects against amyloid beta-peptide toxicity in brain mitochondria of diabetic rats, Neurobiol. Dis. 18 (2005) 628-637.

[36] T. Watanabe, S. Dohgu, F. Takata, T. Nishioku, A. Nakashima, K. Futagami, A. Yamauchi, Y. Kataoka, Paracellular barrier and tight junction protein expression in the immortalized brain endothelial cell lines bEND.3, bEND.5 and mouse brain endothelial cell 4, Biol. Pharm. Bull. 36 (2013) 492-495.

[37] P. Picone, M.A. Sabatino, L.A. Ditta, A. Amato, P.L. San Biagio, F. Mulè, D. Giacomazza, C. Dispenza, M. Di Carlo, M., Nose-to-brain delivery of insulin enhanced by a nanogel carrier. J Control Release 270 (2017) 23-36.

[38] N. Kamei, M. Tanaka, H. Choi, N. Okada, T. Ikeda, R. Itokazu, M. Takeda-Morishita, Effect of an enhanced nose-to-brain delivery of insulin on mild and progressive memory loss in the senescence-accelerated mouse, Mol. Pharmaceutics 14 (2017) 916-927.

[39] C. Benedict, M. Hallschmid, B. Schultes, J. Born, W. Kern, Intranasal insulin to improve memory function in humans, Neuroendocrinology 86 (2007) 136-142.

[40] H.B. Schioth, S. Craft, S.J. Brooks, W.H. 2nd. Frey, C. Benedict, Brain insulin signaling and Alzheimer's disease: current evidence and future directions, Mol. Neurobiol. 46 (2012) 4-10.

[41] N. Kamei, M. Takeda-Morishita, Brain delivery of insulin boosted by intranasal coadministration with cell-penetrating peptides, J. Control. Release 197 (2015) 105-110.

[42] N. Kamei, T. Shingaki, Y. Kanayama, M. Tanaka, R. Zochi, K. Hasegawa, Y. Watanabe, M. Takeda-Morishita, Visualization and quantitative assessment of the brain distribution of insulin through nose-to-brain delivery based on the cell-penetrating peptide noncovalent strategy, Mol. Pharmaceutics 13 (2016) 1004-1011.

[43] E.M. Rhea, S.R. Humann, S. Nirkhe, S.A. Farr, J.E. Morley, W.A. Banks, Intranasal insulin transport is preserved in aged SAMP8 mice and is altered by albumin and insulin receptor inhibition, J. Alzheimer's Dis. 57 (2017) 241-252.

[44] M. van Woensel, N. Wauthoz, R. Rosiere, K. Amighi, V. Mathieu, F. Lefranc, S.W. van Cool, S. de Vleeschouwer, Formulations for intranasal delivery of pharmacological agents to combat brain disease: A new opportunity to tackle GBM, Cancers 5 (2013) 1020-1048.

[45] N.J. Johnson, L.R. Hanson, W.H. 2nd Frey, Trigeminal pathways deliver a low molecular weight drug from the nose to brain and orofacial structures, Mol. Pharm. 7 (2010) 884-893.

[46] C.V. Pardeshi, V.S. Belgamwar, Direct nose to brain drug delivery via integrated nerve pathways bypassing the blood-brain barrier: an excellent platform for brain targeting, Expert Opin. Drug Delivery 10 (2013) 957-972.

[47] H.A. Ravin, A.M. Seligman, J. Fine, Polyvinyl pyrrolidone as a plasma

expander - Studies on its excretion, distribution and metabolism, N. Eng. J. Med. 247 (1952) 921-929.

[48] I.A. Alsarra, Mucoadhesive polymeric hydrogels for nasal delivery of acyclovir, Drug Dev. Ind. Pharm. 35 (2009) 352-362.

[49] X. Duan, and S. Mao, New strategies to improve the intranasal absorption of insulin, Drug Discovery Today 15 (2010) 416-427.

[50] M. Stützle, J. Flamm, S. Carle, K. Schindowski, Nose-to-Brain delivery of insulin for Alzheimer's disease, Admet & Dmpk 3 (2015) 190-202.

[51] R.G. Thorne, C.R. Emory, T.A. Ala, W.H. Frey II, Quantitative analysis of the olfactory pathway for the drug delivery to the brain, Brain Research 692 (1995) 278-282.

[52] R.L. Doty, The olfactory vector hypothesis of neurodegenerative disease: is it viable?, Ann. Neurol. 63 (2008) 7-15.

[53] K. Kristensson, Microbes' roadmap to neurons, Nat. Rev. Neurosci. 12 (2011) 345-357.

[54] F. Anton, and P. Peppel, Central projections of trigeminal primary afferents innervating the nasal mucosa: a horseradish peroxidase study in the rat, Neuroscience 41 (1991) 617-628.

[55] A.M. Deatly, A.T. Haase, P.H. Fewster, E. Lewis, M.J. Ball, Human herpes virus infections and Alzheimer's disease, Neuropathol. Appl. Neurosci. 16 (1990)213-223.

[56] S.S. Davis, and L. Illum, Absorption enhacers for nasal drug delivery, Clin. Pharmacokinet. 42 (2003) 1107-1128.

[57] R. Walters, R.P. Kraig, I. Medintz, J.B. Delehanty, M.H. Stewart, K. Susumu, A.L. Huston, P.E. Dawson, G. Dawson, Nanoparticle targeting to neurons in a rat hippocampal slice culture, ASN Neuro 4 (2012) 383–392.

[58] R. Walters, I.L. Medintz, J.B. Delehanty, M.H. Stewart, K. Susumu, A.L. Huston, P.E. Dawson, G. Dawson, The role of negative charge in the delivery of quantum dots to neurons, ASN Neuro 7 (2015) 1-12.

[59] J. Mudassir, Y. Darwis, P.K. Khiang, Prerequisite characteristics of nanocarriers favoring oral insulin delivery: nanogels as an opportunity, Int. J. Polym. Mater. Polym. Biomater. 64 (2015) 155-167.

[60] A.A. Akintola, D. van Heemst, Insulin, aging and the brain: mechanisms and implications, Frontiers in Endocrinology 6 (2015) 1-13 art. #13.

[61] W.A. Banks, The source of cerebral insulin, Eur. J. Pharmacol. 490 (2004) 5–12.

5. Synthesis of NG-AntimiR-31 conjugates for the treatment of colorectal cancer

This Chapter is dedicated to the synthesis and characterization of an antimiR-31-nanogel conjugate for the potential treatment of colorectal cancer.

5.1 Introduction

Colorectal cancer (CRC) is the third most commonly diagnosed cancer worldwide, with nearly 1.4 million new cases diagnosed in 2012. [1] Colorectal cancer develops in the colon or in the rectum, also known as the large intestine, that are parts of the digestive system, also called the gastrointestinal (GI) system. In general, CRC is characterized by a slow development, over a period of 10 to 20 years [2] and, for this reason, prevention and on time diagnosis may have a strong impact on its prognosis. Even though FDA has approved several chemotherapeutics for CRC treatment, the research of more efficacious and better tolerated therapeutic agents is still ongoing. With this aim, in the last decade, miRNAs have been intensively investigated. MiRNAs are small, single strand, non-coding RNA molecules with a critical role in several biological functions. The known mechanism of action is through interaction with messenger RNA (mRNA), which results in its degradation/destabilization or translation inhibition. [3-5] Furthermore, since a specific mRNA may interact with many miRNAs, the regulatory effects of miRNAs can be exerted through a combination of concurring mechanisms. Recent studies have demonstrated that the alteration of miRNA expression may cause or be associated with the progression of several neoplastic and degenerative diseases. Therefore, therapies targeting miRNA dysregulation are very promising. The therapeutic strategy can be either to augment the miRNA activity by administering exogenous miRNA, or to silence its activity with inhibitors (antimiRs) (i.e., genetically-engineered, single-strand, oligonucleotides that can either bind to miRNA or to the mRNA sequence that bind to miRNA). [6]

Cancer cells with abnormal miRNA expression may undergo restless proliferation, evade growth suppression, resist cell death, activate invasion and metastasis, and induce angiogenesis. Since miRNAs may function as either oncogenes or tumor suppressors, their specific functions must be clearly identified. Once clarified, the advantage of using miRNA or antimiRs therapeutics is based on their ability to concurrently target multiple pathway effectors involved in tumorigenesis.

As with previous RNA-based therapies, the translation of these approaches to the clinic is subjected to the development of efficacious and affordable delivery strategies that can ensure spatial-temporal control of the therapeutic oligonucleotides at the target cells, overcoming biological barriers. Due to their polyanionic nature, miRNAs and antimiRs display reduced cellular uptake and poor intracellular trafficking, where sequestration in endosomes is one of the major limitations. [7] Another obstacle is the limited stability of RNAs and RNA's inhibitors in body fluids, mainly caused by the ubiquitous presence of nucleases. [8]

This study is testing the delivery platform based on covalent conjugation of antimiRs to soft and flexible PVP-co-acrylic acid based nanogels. In particular, miR-31 in colon rectal cancer model was selected, because of its well-known role in colorectal cancer (CRC) progression.[9] It has been demonstrated that the high-level expression of miR-31 is significantly associated with a poor prognosis and a more aggressive cancer phenotype in patients with CRC ($p < 0.05$). In fact, the stable over-expression of miR-31 in CRC cells has been also demonstrated to be sufficient to promote cell proliferation, invasion, and migration in vitro, and facilitated tumor growth and metastasis in vivo. In addition, recent studies observed that miR-31 is involved in tumor therapy resistance: in fact, the suppression of miR-31 increased the sensitivity of colon cancer cells to 5-fluorouracil and affected cell migration and invasion. [5,10]

Therefore, the administration of antimiR-31 may help in the control of the levels of miR-31 and thus be useful in colon cancer therapies.

To the best of my knowledge, there is only one documented example of antimiR loaded onto a nanogel.[11] As commonly done for other therapeutic genes, the antimiR is incorporated in the nanocarrier by electrostatic complexation, exploiting the mutual attraction between the cationic groups present in the NG and the negatives charges of the antimiR. Complexation causes the network to collapse into a dense nanostructure and entrap the agent with high loading efficiency.[11,12] The main limitation of this approach is that the biological effect is deemed to matrix degradation and antimiR release. This can complicate the temporal control of its action. Besides, it is known that cationic nanoparticles preferentially absorb plasma proteins, which may cause RES activation and relatively fast elimination.[13]

To overcome this problem, a different strategy was pursued, consisting in the conjugation of an amino-modified variant of the antimiR-31 to the nanogel by forming a stable amide bond with one of the carboxyl groups of the nanogel. Preliminary studies using a “non-functional” oligonucleotide have shown that the covalent bond to the nanogel does not prevent the oligonucleotide binding ability to the complementary sequence, probably due to the flexibility of the particle and its link to the oligonucleotide.[14] This result was never demonstrated on a cellular model and provides motivation for the present investigation.

A conjugation protocol was developed and AntimiR-31-nanogel conjugated systems were subjected to several physico-chemical characterizations in order to determine the conjugation degree, the hydrodynamic size, net surface charge and morphology. Another important aspect investigated was the stability upon storage of the formulation (both as aqueous dispersion and as freeze-dried solid) and the possibility of reconstitution of the dispersion from a dry powder.

Thanks to the collaboration with colleagues of Dipartimento di Biopatologia e Biotecnologie Mediche, Sezione di Biologia e Genetica, Università degli Studi di Palermo, Palermo, Italy, antimiR-31 conjugated systems have been biologically evaluated. The ability of NG-AntimiR-31 to permeate cell membrane was investigated by confocal analysis using a metastatic SW620 colon cancer cell line, which express high levels of miR-31.[15] Moreover, the biological activity of NG-AntimiR 31 was by quantification of miR-31 and of its target gene E2F, involved in cancer cell survival.[16]

5.2 Experimental

5.2.1 Materials

Poly(N-vinyl pyrrolidone)-co-acrylic acid (PVP-co-AA) nanogels (NG) (see 3.2.2), antimiR-31 (5'-AGCUAUGCCAGGAUCUUGCCU-3'), labeled with a fluorescent probe and modified to have a primary amino group, was purchased from Biolegio BV (5'-Label-Fluorescein amidite (6-FAM); 3'-Label-amino-modified C6, MW 6689.22 Da). Dimethyl sulfoxide (DMSO), 1-ethyl-3-[3-dimethylaminopropyl] carbodiimide hydrochloride (EDC), N-hydroxysulfosuccinimide sodium salt (Sulfo-NHS), 2-(N-morpholino) ethane sulfonic acid (MES), trishydroxymethylaminomethane hydrochloride (TRIS HCl) and ethylenediaminetetraacetic acid (EDTA) were all purchased from Sigma Aldrich and used as received.

5.2.2 Preparation of NG-AntimiR-31 conjugates

Grafting of antimiR-31 on NGs was carried out following an EDC/Sulfo-NHS protocol (for more details see Appendix A.7). Firstly, a given volume of NG aqueous dispersion was mixed with EDC and Sulfo-NHS aqueous solution (isotonic phosphate buffered saline pH 7.4) for 30 minutes, then given volumes

of antimiR-31 solution (100μM) were added, corresponding to various antimiR-31/NG carboxyl groups ratios (namely, 1:40, 1:20 and 1:10). The reaction was conducted for further 24 hours under gentle stirring at room temperature. As a control, NGs were also subjected to the above-described EDC/Sulfo-NHS protocol with the exception that antimiR was not added to the reactor.

AntimiR-conjugated NG systems were then purified through prolonged dialysis (7 days) against milli-Q water at room temperature, using 12 kDa cut-off membrane to remove unreacted reagents. Both synthesis and purification of NG-AntimiR-31 conjugates were conducted under dark conditions. The final concentration of NG-AntimiR-31 nanogels was 3 mg mL^{-1}. The conjugation degree, defined as the average number of antimiR-31 molecules per NG, was estimated by UV-VIS absorption spectroscopy on the NG-AntimiR-31 variants at λ (Max Abs)= 494 nm (Jasco V 670 spectrophotometer at room temperature, scan-speed 100 nm min^{-1}, band width 1 nm). Samples of NG-AntimiR-31 were also centrifuged at 2500 rpm for 30 min from 100 kDa cut-off centrifuge-filters (Thermo Scientific IEC CL10 Centrifuge) and the eluted fractions were analyzed by UV-vis absorption to ascertain that no antimiR was released. The three variants of antimiR-31 conjugates corresponding to 1:40, 1:20 and 1:10 antimiR-31/NG carboxyl groups ratios were named after NG1(or 2)-AntimiR-31-HC, NG1(or 2)-AntimiR-31-IC and NG1(or 2)-AntimiR-31-LC, respectively.

5.2.3 Physico-chemical characterizations of NG-AntimiR-31 conjugates

The hydrodynamic dimensions of antimiR-conjugated NG variants were measured by dynamic light scattering (DLS) (for more details see Appendix A.2). Measurements were carried out after dilution and filtration with 0.45 μm pore size syringe filters to eliminate impurities introduced with the dialysis. Preliminary tests made on the non-filtrated, “as synthetized” nanogels showed

that 0.45 μm as well as 0.22 μm filtration has no effect neither on the light scattering intensity nor on the particle size distribution.
ζ -potential measurements of antimiR-conjugated NG variants were acquired by a Malvern Zetasizer Nano-ZS. For more details see Appendix A.4.

5.2.4 Morphological analysis

Morphology of NG1(2)-AntimiR-31 dispersions was analysed trough transmission electron microscopy (TEM). More details are reported in Appendix A.5

5.2.5 Stability studies

NG-AntimiR-31 conjugates were incubated at 37°C with (i) isotonic PBF buffer and (ii) PBF buffer at pH 9. Samples were filtered with 100 kDa cut-off centrifuge-filters (Thermo Scientific IEC CL10 Centrifuge) and the eluted fractions were analyzed by UV-vis absorption spectroscopy.
Nanogel conjugates were also incubated with fetal bovine serum (FBS, 10% v/v) at 37°C for 24 hours. DLS measurements were then performed at 25±0.1 °C and at 90° scattering angle, without filtration.
The colloidal stability upon storage at 4°C both in water and in isotonic PBS buffer was investigated by performing DLS analyses. NG-AntimiR-31 conjugates dispersed in water were tested every two weeks for three months, while systems dispersed in isotonic PBS were tested after 20 days of storage.
Nanogel conjugates were also freeze-dried, stored in glass vials up to three months at room temperature, redispersed in PBS buffer, and tested for particle size distribution.

5.2.6 Biological evaluations

Selected antimiR-conjugated NGs variants were subjected to *in vitro* biological evaluations. In particular, the following aspects have been investigated: (i) cell viability in SW cells, (ii) Internalization into colon cancer cells and (iii) biological activity of conjugated antimiR-31 on miR-31 and its target genes expression. A detailed description of the methods is reported in Appendix B3.

5.3 Results and discussion

5.3.1 Synthesis, physico-chemical and morphological characterization of AntimiR-31-conjugated nanogels

Poly(N-vinyl pyrrolidone)-co-acrylic acid nanogel systems were selected as potential nanocarriers of antimiR-31. Two nanogel variants with different average hydrodynamic size and ratio between carboxyl groups and primary amino groups were synthetized. The average molecular weight of the two variants produced was determined by Zimm plot analysis of static light scattering (SLS) data (Appendix A.2), the average numbers of carboxyl groups and primary amino groups per nanoparticle were estimated via colorimetric and fluorimetric methods, (for more details see Appendix A.6). The results are reported in Table 5.1.

Table 5.1. Average weight molecular weight and reactive functional groups present on the bare nanogel systems

System	Mw, (MDa)	-COOH/NG (mol/mol)	-NH_2/NG (mol/mol)
NG1	3.8±0.20	50	38
NG2	4.5±0.12	67	83

NG1 system consists of smaller nanogels (average hydrodynamic size of about 40 nm) with a prevalence of carboxyl groups that grant their surface a slightly negative net electric charge density. NG2 has larger average hydrodynamic size, ca. 60 nm, a prevalence of amino groups and a broader distribution of surface electric charge density, with a larger fraction of nanoparticles that result globally non-charged.

Being the amino groups present at the backbone of the polymeric network and the carboxyl groups on short side branches, it was decided to bind antimiR-31 to the nanogels through the carboxyl groups of the nanogel. For the purpose, the antimiR-31 was synthetized to have a primary amino group at the 3' terminus (Figure 5.1).

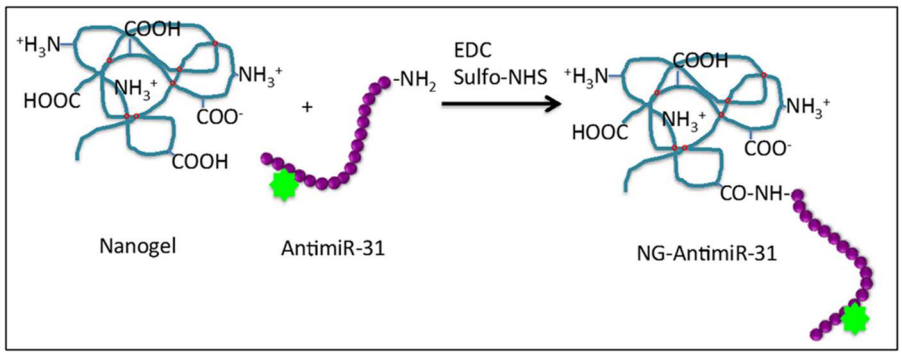

Figure 5.1. Scheme of the conjugation reaction between nanogel and antimiR. The red circles represent crosslinking points on PVP chain.

Since, in principle, the carboxyl groups of the nanogel could react with the amino groups of the same nanogel (intra-molecular crosslinking) or of another nanogel (inter-molecular crosslinking), a preliminary experiment was carried out charging the reactor with the nanogel and with the EDC and sulfo-NHS catalysts used to activate the carboxyl groups, without addition of antimiR-31. After purification by dialysis, the systems were subjected to DLS analysis to check if aggregation or contraction of particle size had occurred.. The particle size distribution of both NG1 and NG2 nanogels after reaction resulted substantially unmodified and, in Fig. 5.2 the autocorrelation function of the scattered light intensity related to the experiment conducted with NG2 system is reported as an example. The lack of mutual reactivity between primary amino groups and carboxyl groups of nanogels is likely due to their sterical hindrance.

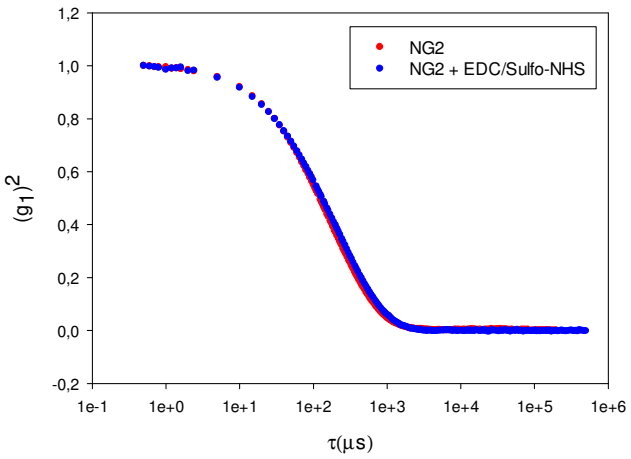

Fig 5.2. the autocorrelation function of the scattered light intensity related to NG2 and in the presence of EDC and Sulfo-NHS.

For the conjugation of antimiR-31 to the nanogel, the molar ratio between antimiR-31 and carboxyl groups was kept lower than the stoichiometric ratio in order to have only a few molecules of antimiR-31 per nanoparticle, leaving most of the carboxyl groups unreacted, thus able to contribute to the colloidal stability of the system and/or to be used for further conjugation reactions. The conjugation reactions were carried out starting from the same weight fraction of nanogels in the reactor feed, varying the concentration of antimiR-31. The reaction yield is higher for NG1 than for NG2 and augments with the increase of antimiR-31 concentration in the reactor, as shown in Table 5.2. Despite the slightly higher number of carboxyl groups per nanogel of the NG2 system (see Table 5.1), they are less densely distributed since the particles are bigger; this results in a lower conjugation efficiency.

Table 5.2. Molar ratio between carboxyl groups on the nanogel and antimiR-31 in the reactor. Average number of antimiR-31 conjugated per nanogel. Reaction yield was measured as percentage of antimiR-31, bound to the nanogel, with respect to the amount loaded in the reactor.

System	AntimiR/COOH	NG1		NG2	
		Average AntimiR-31/NG	Reaction yield %	Average AntimiR-31/NG	Reaction yield %
NG-AntimiR-LC	1:40	0.7	79.7	0.5	45.0
NG-AntimiR-IC	1:20	1.6	80.1	1.0	51.5
NG-AntimiR-HC	1:10	3.5	87.5	2.5	62.5

The estimation of the degree of conjugation was performed by analyzing the various NG-AntimiR-31 conjugates by UV-vis absorption spectroscopy. The molar ratio of antimiR-31 to nanogel increases at the increase of antimiR-31 in the reactor, from one antimiR-31 every two nanogels for the NG1-AntimiR-

system, to three or four antimiR-31 per nanogel for the NG2-AntimiR-HC. The reactions conditions that did not ensure grafting of minimum one antimiR-31 per nanogel (LC-systems) were not further considered.

The four antimiR-NGs systems with degree of conjugation higher than one were further characterized for their hydrodynamic size and surface charge density. Data are reported in Table 5.3. No aggregation can be appreciated; only a slight increase in size and polydispersity, probably due to the increase of the branching degree after conjugation. The surface charge density of the nanogels is only very little modified upon conjugation. NG1 systems, that were initially anionic and fairly monodisperse in terms of surface charge density, kept this feature; likewise, the NG2 systems that were instead more polydisperse.

Table 5.3. Average hydrodynamic diameter (nm) and width of the size distribution from DLS analysis; surface charge density from ζ-potential measurements for bare nanogels and their conjugates.

Sample	**Hydrodynamic diameter, nm**	**ζ-potential**		
		Mean (mV); Area (%); St. Dev. (mV)		
NG1	40.0±15.1	-25.2;100; 5.7		
NG1-AntimiR-IC	58.4 ± 31.7	-22.2; 100; 7.9		
NG1-AntimiR-HC	47.1± 19.2	-38.1; 100; 10.0		
		Peak 1	**Peak 2**	**Peak 3**
NG2	60.1± 16.0	-50; 2.2; 5.59	-3.56; 81.7; 13.2	+30; 14.3; 8.16
NG2-AntimiR-IC	63.2± 25.1	-73.3; 2.5; 3.90	-11.1; 84.5; 13.6	+23.3; 12.9; 6.47
NG2-AntimiR-HC	63.6± 25.3	-40; 19.0; 7.53	-3.89; 71.7; 12.0	+27.6; 9.3; 6.46

The morphological analysis carried out by TEM microscopy did not reveal significant differences among the various samples in good agreement with DLS data. Single particles as well as loose aggregates were visible on the hollow carbon-coated copper stab, the aggregation being the result of the receding water droplet during the drying process. A representative TEM micrograph is shown in Figure 5.3, which refers to the NG1-AntimiR-HC system.

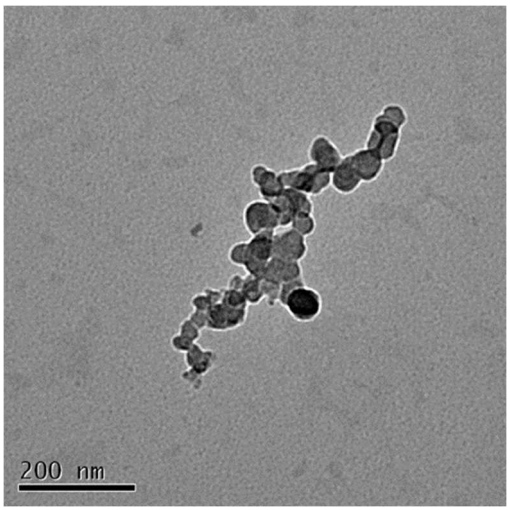

Figure 5.3. TEM micrograph of NG1-AntimiR-HC

5.3.2 Stability studies

To test the strength of the link of antimiR to nanogel and rule out that the bond between the nanogel and the antimiR-31 was purely electrostatic in its nature, samples of the NG1-AntimiR-HC system were incubated at 37°C for 24 h with isotonic PBS and with PBS at pH 9. After incubation, samples were centrifuge filtered and the eluted solutions were analyzed by both UV-vis absorption and emission spectroscopies to check the presence of signals from the FAM emissive label of the antimiR. No signals were detected. Therefore, neither the relatively high salt concentration nor the alkaline pH that would disrupt

eventual electrostatic complexes formed triggered the release of the antimiR-31, thus supporting the covalent attachment of the antimiR to the nanogel through an amide bond.

The colloidal stability of the formulations upon storage at 4°C was investigated, both in water and isotonic PBS buffer, measuring the hydrodynamic diameters as function of the time. Data are reported in Table 5.4. An increase in average hydrodynamic size occurs when the nature of the dispersing medium is changed from water to isotonic buffer, and for the antimiR-conjugated systems only. No aggregation occurs upon storage at 4°C for three months in each of the two media. This quite remarkable colloidal stability is due to the presence of ionizable groups, to the small density mismatch between the water-swollen nanogel and dispersing/swelling medium, and to the presence of loose chains stretching out in the medium. The slight increase of average particle size in the presence of saline solutions of the antimiR conjugates could be due to the displacement of “internal” interactions between the strongly anionic antimiR and the cationic groups present in the nanogels by the small ions of the saline solution. This effect resembles the anti-polyelectrolyte effect of zwitterion polymers.[17]

Table 5.4. Colloidal stability at 4°C of antimiR-31-conjugates dispersed in water and in isotonic PBS evaluated by DLS analysis; average hydrodynamic diameter (nm) and width of the size distribution.

System – dispersing medium	NG1-AntimiR-31		NG2-AntimiR-31	
	t = 0	t = 3 month	t = 0	t = 3 month
NG-AntimiR-IC – water	58 ± 31.7	61.0 ± 31.2	63.2 ± 25.1	63.4 ± 26.5
NG-AntimiR-HC – water	47.1 ± 19.2	49.4 ± 23.1	63.6 ± 25.3	77.0 ± 25.3
	t = 0	**t = 20 days**	**t = 0**	**t = 20 days**
NG-AntimiR-IC – PBS	82.0 ± 21.1	83.2 ± 28.1	79.7 ± 24.8	76.2 ± 23.6
NG-AntimiR-HC – PBS	72.2 ± 22.1	71.4 ± 25.3	79.8 ± 24.8	82.6 ± 26.6

Table 5.5 reports data from DLS analysis of nanogel-conjugates, soon after freeze-drying, after one month and after three months storage at room temperature. Data indicate that no aggregation occurs if the dispersion is reconstituted immediately after freeze-drying or after one-month storage, while some degree of aggregation occurs after three-months, probably because the storage was not carried out in completely moisture-free conditions.

Table 5.5. Hydrodynamic diameter (nm) and width of the size distribution of antimiR-31-conjugates freeze-dried and stored at room temperature as dry powder, then reconstituted as aqueous dispersions.

Sample	Before freeze-drying	Soon after freeze-drying	1 month after freeze-drying	3 month after freeze-drying
NG1 – water	40.0 ± 15.1	40.4 ± 18.1	42.2 ± 20.3	63.3 ± 26.2
NG1-AntimiR-IC– water	58 ± 31.7	73 ± 23.5	80.1± 28.2	123.2 ± 34.3

5.3.3 Biological effects of NG-AntimiR-31

The aim of the biological evaluations performed is a preliminary investigation of in vitro effects of NG-AntimiR-31 on colon cancer cells, in the prospect of developing a new therapeutic approach for colon cancer progression. In particular, the cytotoxicity of antimiR-31 conjugated to NG and its ability to modulate the expression of miR-31 target genes on a suitable colon cancer cell line model have been tested.

In consideration of the higher yields of conjugation reaction of antimiR-31 to NG1 compared to NG2, conjugates of NG1 were selected. To investigate their biocompatibility, a cell viability assay on SW620 cells treated with different concentrations (1nM, 10nM and 30 nM) of bare NG or conjugated with antimiR-31 (both IC and HC) was performed. As shown in Fig 5.4, SW cells viability was evaluated 24 and 48 hours after NG treatments. While NG-AntimiR-31-IC treatments did not reveal any significant toxicity, the higher concentration of NG-AntimiR-31-HC reduced cell viability in SW620 cells.

No toxicity was revealed by transfecting SW620 cells with 10nM or 30nM of "free" AntimiR-31 with attractene (data not shown). Further experiments, aimed to investigate the biological properties of NG-AntimiR-31, were performed using NG-AntimiR-IC.

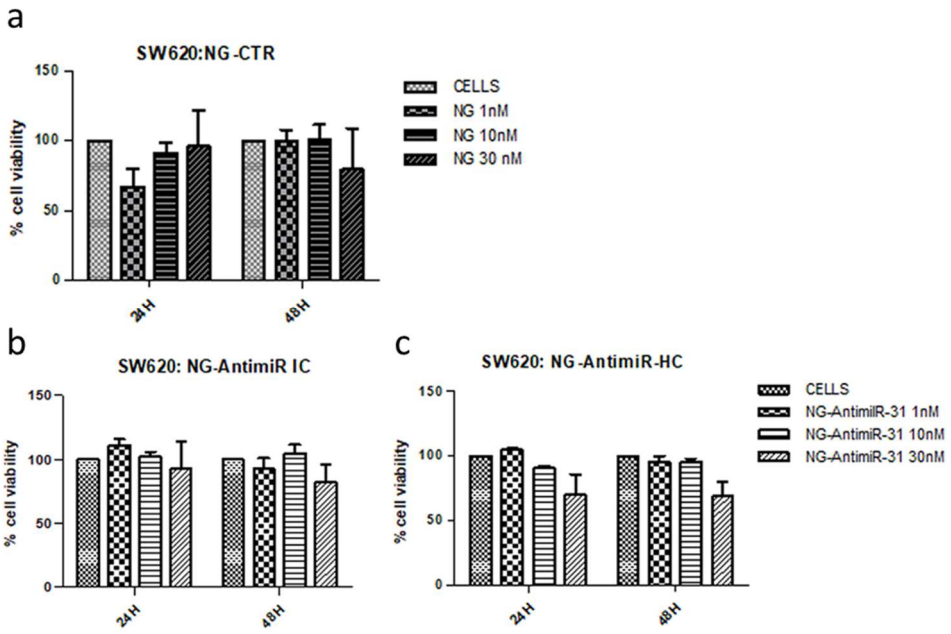

Figure 5.4. Results of cell viability of SW620 cells treated with (a) Bare NG; (b) NG-AntimiR-IC and (c) NG-AntimiR-HC at three different concentrations: 1nM, 10nM and 30nM, for 24hours and 48 hours. Data are expressed as percentage of cells viability compared to untreated cells (100%) (Mean ± SD, n=3 duplicates).

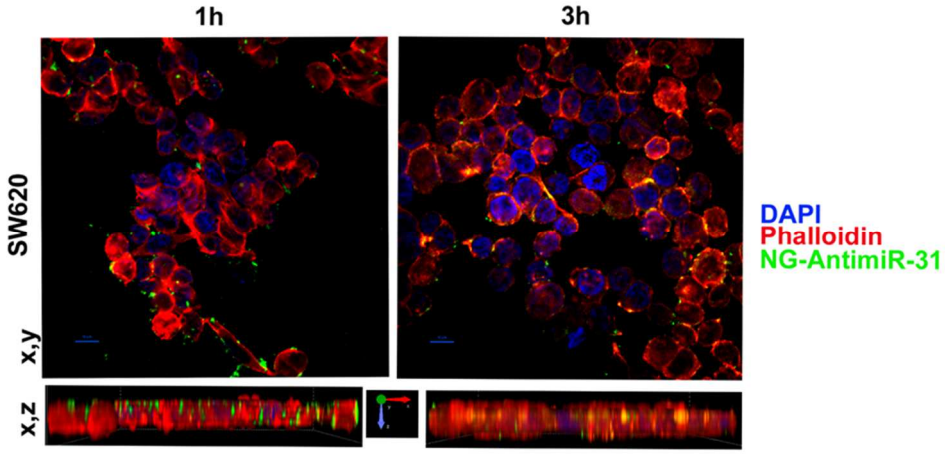

Figure 5.5. Confocal maximum intensity average of SW cells incubated 1 or 3 hours with NG-AntimiR-IC.

Uptake assay followed by confocal analysis allowed to demonstrate the ability of NG-AntimiR-31 to permeate SW cells. As shown in Figure 5.5, NG-AntimiR-31 mainly localized on cell surface one hour after incubation (green dots), penetrated SW-cells after three hours (orange dots). Finally, the biological activity of the transported AntimiR-31was investigated.

As shown in Figure 5.6, the treatment of cell line with 30nM of NG-AntimiR-IC suppressed miR-31 levels with efficiency comparable to that obtained by antimiR-31 transfection with Attractene. This data confirms that the conjugation of the oligonucleotide to our nanogels did not affect the annealing between exogenous antimiR-31 and endogenous miR-31. To further evaluate the biological functions of NG-AntimiR-31, E2F, the transcriptional levels of miR-31 target (obtained by miRTarBase) was analyzed.[18] As shown in Figure 5.5 the effects induced by NG-AntimiR-31 treatment are in line with those obtained after transfection of antimiR-31. These data demonstrated that NG conjugation did not affect antimiR-31 activity.

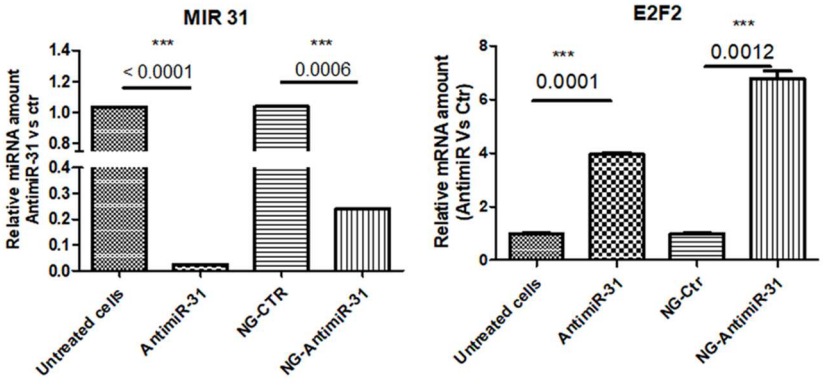

Figure 5.6. Real time-PCR for miR-31 in SW620 cells, treated with 30nM of NG-AntimiR-IC. Data were normalized for U6, which was used for miRNA normalization. ΔΔct is expressed as Fold Of Induction (FOI) respect to expression in control samples. Data are the mean ± SD of three independent experiments.

Conclusions

Two polyvinyl pyrrolidone-based nanogel systems, with different average hydrodynamic size and concentration of carboxyl and primary amino groups, were synthetized by e-beam irradiation and covalently conjugated to antimiR-31. The interest on antimiR-31 comes from the many evidences about the role of miR-31 in cancer progression and tumor therapy resistance. The NG-AntimiR-31 conjugates showed good colloidal stability and full redisperdibility soon after freeze-drying and also after one month storage at 4°C. The biological effects of NG-AntimiR-31 conjugates were investigated in syngenic in vitro models. Cell viability evaluation in SW cells, treated with increasing concentrations of NG-AntimiR conjugates (up to 30 nM), showed that no concentration-dependent toxicity is induced 24h and 48h after the treatment. Internalization into colon cancer cells of the designed NG-AntimiR nanoconstruct was appreciable already after 3 hours of treatment. Moreover, NG-AntimiR-31 conjugates showed ability to vehicle antimiR-31 in SW cells

regulating the expression of miR-31 and its target genes, thus demonstrating that the covalent link of antimiR-31 to these soft nanogels did not affect the its functionality in vitro. Future work will focus on further understanding the in vivo performance of clinically relevant NG-AntimiR-31 formulations, with the prospect of overcoming some of the limits of the current pharmacological therapies for aggressive colon cancers.

Acknowledgments

Some parts and some figures of this Chapter were reproduced from Ref. "Dispenza, C.; Sabatino, M.A; Ajovalasit, A.; Ditta, L.A.; Ragusa, M.; Purrello, M.; Costa, V.; Conigliaro, A.; Alessandro, R.; Nanogel-AntimiR-31 conjugates affects colon cancer cells behaviour. RSC Adv., 2017, 7, 52039" with permission from the Royal Society of Chemistry.

This research was supported by HIPPOCRATES - PON02_00355_2964193 and IAEA CRP F22064 Nanosized delivery systems for radiopharmaceuticals.

TEM experimental data were provided by Centro Grandi Apparecchiature e UniNetLab e Universita' di Palermo, funded by P. O. R. Sicilia 2000 e 2006, Misura 3.15, Quota Regionale.

Collaborators' contributions to the Chapter

Dr. Maria Antonietta Sabatino supported in synthesis and characterization of the non targeted NGs and developed the conjugation protocols.
Ms. Alessia Ajovalasit supported in synthesis and characterization of the AntimiR-NG conjugates.
Dr. Viviana Costa (Piattaforma Tecnologica per l'Ingegneria Tissutale, Teranostica ed Oncologia, Istituto Ortopedico Rizzoli, Palermo, Italy), Dr. Alice Conigliaro and Prof. Riccardo Alessandro (Dipartimento di Biopatologia e Biotecnologie Mediche,

Sezione di Biologia e Genetica, Università degli Studi di Palermo, Palermo, Italy) performed the biological evaluations. Dr. M. Ragusa and Dr. M Purrello chose the target (miR-31) and designed the targeting agent.

References

[1] American Cancer Society. Colorectal Cancer Facts & Figures 2014-2016. Atlanta: American Cancer Society, 2014.

[2] Winawer SJ, Zauber AG. The advanced adenoma as the primary target of screening. Gastrointest Endosc Clin N Am. 2002;12: 1-9.

[3] M. Wery, M. Kwapisz and A. Morillon, Wiley Interdiscip Rev Syst Biol Med., 2011, 3(6), 728-738.

[4] B. Yan, Z.H. Wang and J.T. Guo, Genomics, 2012, 99(2), 76-80.

[5] M.D Jansson and A.H. Lund, Mol. Oncol., 2012, 6(6), 590-610.

[6] J. Krutzfeldt, N. Rajewsky, R. Braich, K.G. Rajeev, T. Tuschl, M. Manoharan and M. Stoffel, Nature, 2005, 438(7068),685-689.

[7] G. Tiram, A. Scomparin, P. Ofek and R. Satchi-Fainaro, J. Biomed. Nanotechnol., 2014, 10(1), 50-66.

[8] Y. Zhang, Z. Wang, R.A. Gemeinhart, J. Controlled Release, 2013, 172(3), 962-974.

[9] T. Mitamura, H. Watari, L. Wang, H. Kanno, M.K. Hassan, M. Miyazaki, Y. Katoh, T. Kimura, M. Tanino, H. Nishihara, S. Tanaka and N. Sakuragi, Oncogenesis, 2013,25, 2:e40.

[10] C.M. Croce, Nat. Rev. Genet., 2009, 10(10), 704-714.

[11] H. Zou, Z. Wang and M. Feng, J. Controlled Release, 2015, 214, 121-133.

[12] J. Yu, H. Zhao, L. Ye, H. Yang, S. Ku, N. Yang and N. Xiao, J. Mater. Chem., 2009, 19, 1265-1270.

[13] F. Alexis, E. Pridgen, L.K. Molnar and O.C. Farokhzad, Mol. Pharm., 2008, 5, 505-515.

[14] C. Dispenza, G. Adamo, N. Grimaldi, D. Bulone, M.L. Bondì, S. Rigogliuso and G. Ghersi, J. Appl. Polym. Sci., 2014, 131, 239774–239780.

[15] M. H. Yang, J. Yu, N. Chen, X. Y. Wang, X. Y. Liu, S. Wangand Y. Q. Ding,PLoS ONE, 2013,8(12), e85353

[16] A. Lo Dico, V. Costa, C. Martelli, C. Diceglie, F. Rajata, A. Rizzo, C. Mancone, M. Tripodi, L. Ottobrini, R. Alessandro and A. Conigliaro, Theranostics, 2016, 6, 1105-1118.

[17] F. Wang, J.F. Yang and J. Zhao, Polymer International, 2015, 64 (8), 999-1005.

[18] T. Li, W. Luo, K. Liu, X. Lv and T. Xi, Biotechnol Lett., 2015, 37(3), 523-32.

6. Synthesis of NG-Bombesin-DOTA conjugates for targeted radiopharmaceutical delivery to tumours

In the present Chapter the synthesis and characterization of Bombesin-DOTA-nanogel system for the potential diagnosis and/or treatment of oncological diseases is presented.

6.1 Introduction

Despite the numerous progresses in the knowledge, diagnosis and treatment of cancer, still today cancer is a main public health issue worldwide and the second cause of death in the United States. According to the American Cancer Society in 2018 there will be 1.7 million of new cancer cases diagnosed and 0.6 million cancer deaths in the United States. [1] These numbers may be explained by the current limitation in on time and reliable diagnostic methods and inefficacious therapy approaches.

Currently, diagnoses may be performed by several imaging methods that can be classified in anatomical and molecular imaging techniques. Among the anatomical imaging approaches, computer tomography (CT), magnetic resonance imaging (MRI), ultrasound (US) can be counted. Single-photon emission computed tomography (SPECT) and positron emission tomography (PET) are the most sensitive molecular imaging techniques that allow to identify changes caused by the tumour at molecular and cellular levels before tissue modification become appreciable. [2]

Even though more than 90 chemotherapeutics have been approved by FDA, [3] they are generally characterized by low efficacy and numerous side effects. The reason why is essentially due to a lack in specifically targeting of tumour tissues. To overcome the limits related to diagnosis and therapy of cancerous pathologies, in recent years an emerging class of compounds have been proposed. They are known as peptide radiopharmaceuticals and they are made by a peptide and by a chelating agent. The peptide acts as active targeting agent, and they are chosen in order to bind specific receptors that are over-expressed in tumour cells/tissues. Several peptides

have been found to target specific tumours and, among them can be counted (i) bombesin for colorectal, prostate, breast, pancreas, gastric, small cell lung cancer; (ii) somatostatin for neuroendocrine tumors, lymphoma, paraganglioma, carcinoids, breast, brain, renal, small cell lung cancer, medullary thyroid cancer; and (iii) vasoactive intestinal peptide for breast, prostate, stomach, liver and neuroendocrine tumors.[4] The chelating agent, based on the nature of the entrapped radioisotope, may allow the radiopharmaceutical to be either a therapeutic or a diagnostic device.

The chelators entrap radioisotopes through coordinative bonds and, depending on size, charge, and electron configuration of the radiometals, the coordination number varies from 2 to 8. [2]

Generally, for this purpose macrocyclic chelators are used, such as NOTA (1,4,7-triazacyclononane-1,4-7-triacetic acid) and DOTA (1,4,7,10-tetraazacyclododecane-1,4,7,10-tetraacetic acid) and an acyclic analog, known as DTPA (diethylenetriamine-*N,N,N′,N″,N″*-pentaacetic acid). [2]

The clinically relevant radioisotopes employed for diagnostic imaging purposes are ^{99m}Tc, ^{111}In, $^{68/66}$Ga, ^{18}F, ^{123}I, ^{64}Cu, while for therapy purposes (endoradiotherapy), are ^{111}In, $^{64/67}$Cu, ^{90}Y, ^{177}Lu, ^{213}Bi.[4]

Generally, peptides are characterized by rapid pharmacokinetics, a high receptor binding affinity and by an efficiently ability to penetrate into tumours. [5-7] Among the limitations their fast removal from the blood by rapid renal clearance, due to their small dimension (< 5 nm) may be counted [8-9] and, above all for natural peptides, their short plasma half-life due to enzymatic degradation. [9] As an example, natural somatostatin peptide is characterized by a plasma half-life of 2-3 minutes. Several strategies have been proposed to improve the stability and efficacy of the radiopeptides. Often, in order to improve their half-life, peptide sequence could be modified introducing for example a D-amino acid, still preserving the biological activity. How it has been done for the ^{111}In-labeled somatostatin analogue octreotide (OctreoScan™) that was the first radiopharmaceutical approved by FDA for diagnostic use.[4]

Another possible strategy is the employment of a nanocarrier as substrate, thanks to by several potential advantages with respect to conventional small molecule-based therapy. [10] In fact, for their bigger dimension (40-200 nm) in general nanocarriers cannot be rapidly eliminated through the kidneys, they present a high payload capacity, and, if properly designed, they can protect the peptide from enzymatic degradation.

In this work, Bombesin-DOTA was covalently attached to PVP-co-AA nanogels and subjected to several physico-chemical characterizations, to determine the conjugation degree, the hydrodynamic size and size distribution. Colloidal stability tests were also conducted investigating storage time and high temperature treatment. Finally, in collaboration with the Centre for Nuclear Research, Radioisotope Centre POLATOM, Otwock, Poland, NG-Bombesin-DOTA conjugated systems were biologically evaluated both *in vivo* and *in vitro.*

6.2 Experimental

6.2.1 Materials

Poly(N-vinyl pyrrolidone)-co-acrylic acid nanogels (NG) (see par 3.2.2), 1-ethyl-3-(3-dimethylaminopropyl)carbodiimide (EDC), N-Hydroxysulfosuccinimide (Sulfo-NHs) and Bombesin (BBN) were supplied by Sigma Aldrich; Bombesin-DOTA (BBN-DOTA) was obtained via IAEA. All the chemicals were used without further purification.

6.2.2 Conjugation of PVP-co-AA nanogels with Bombesin and Bombesin-DOTA

Grafting of BBN or BBN(-DOTA) on NGs (NG-BBN and NG-BBN(-DOTA) was carried out following a two steps protocol that promotes the formation of an amide bond between carboxyl group of the NG and a primary amino group of the peptide (for more details see Appendix A.7). In particular, a given volume of NG aqueous

dispersion was mixed with EDC and Sulfo-NHS aqueous solution (isotonic phosphate buffered saline, pH 7.4) for 30 minutes, then a given volume of BBN or BBN(-DOTA) water solution was added, corresponding to 1:6 ratio with respect to the available carboxyl groups in the nanogel. The reaction was conducted for six hours under gentle stirring at room temperature. The BBN or BBN-DOTA conjugated systems were then purified through prolonged dialysis against isotonic PBS, using 12 kDa cut-off membrane to remove unreacted reagents. In order to increase the yield of conjugation, the influence of a pre-dialysis step on the NG (12 kDa cut-off membrane in milliQ water for 48 hours), before the conjugation with BBN-DOTA, to remove low molecular weight by-products (probably acrylic acid oligomers smaller than 12 kDa), was investigated. The conjugation degree, that is given by the number of molecules of BBN or BBN(-DOTA) per nanoparticle, was estimated by UV-vis fluorescence spectroscopy at λ_{exc}= 280 nm and λ_{em}= 350 nm. In Fig 6.1 a calibration curve, built plotting the emission at peak (related to the tryptophan in the bombesin amino-acids sequence) as a function of BBN-(DOTA) concentration, is reported.

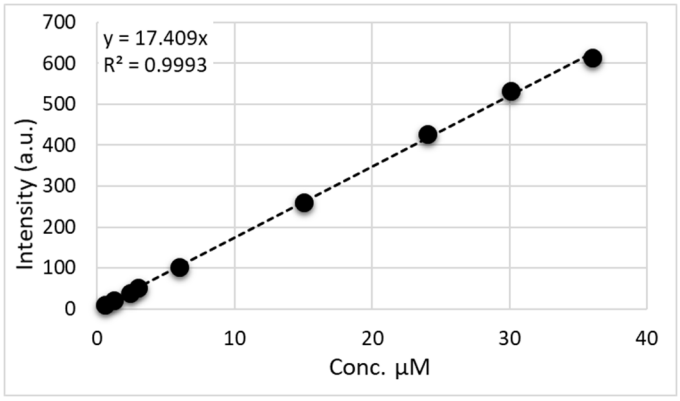

Fig 6.1. Calibration curve of Bombesin-DOTA water solution

6.2.3 Physico-chemical characterizations of NG-BBN variants

Dynamic Light Scattering analysis

The hydrodynamic diameter of BBN-DOTA conjugated systems, dialyzed against milliQ water and isotonic PBS, were analyzed by DLS measurements (for more details see Appendix A.1). Before the measurement, all the samples were diluted to a concentration of 0.05 wt% to avoid multiple scattering and filtrated with 0.45 µm syringe filters to remove impurities.

Gel Filtration Chromatografy (GFC)

Gel filtration chromatography analyses were performed on BBN-(DOTA) conjugated systems, both in milliQ water and in PBS. All samples were diluted to 0.1 wt% and filtered with 0.45 µm cut-off syringe filters. (for more details see Appendix A.3)

6.2.4 Colloidal stability studies

The colloidal stability of NG-BBN-DOTA stored at 4°C as dispersion was tested performing DLS measurements after three and six months. The hydrodynamic diameters of BBN-DOTA conjugated systems were also investigated after a thermal treatment applied for their radiolabelling (50 minutes at 80° C).

6.3 Results and discussion

6.3.1 Decoration of nanogels with bombesin

The PVP-co-AA nanogels was used as substrate for the covalent attachment of Bombesin-DOTA. As reported in par. 3.2.2, nanogels were subjected to dialysis (12 kDa cut-off) before the conjugation reactions. Here the conjugation with Bombesin-DOTA was performed also starting from NG as synthesized. The conjugation degree was determined by UV-vis fluorescence spectroscopy, measuring the fluorescence signal related to tryptophan present in the bombesin amino-acids sequence. As shown

in Tab 6.1, the pre-dialysis step had a strong impact in terms of conjugation yield. We believe that the low molecular weight fragments, present in the system after irradiation, interact easily with the peptide (probably due to their carboxyl groups functionalization), and a decrease of the conjugation degree occurs. Indeed, the concentration of BBN-DOTA was estimated to be 1.5 μmol per gram of NG, corresponding to about 7 BBN-DOTA per NG (with a final concentration – after purification - of 2.85 mg/mL of NG in PBS). When NGs were dialyzed before the conjugation, the conjugation degree was estimated to be about 35 BBN-DOTA per NG equals (5.7 μmol BBN-DOTA per g of NG), with a yield of about 28 %. A good reproducibility of the conjugation degree and reaction yield was obtained. No appreciable changes of the hydrodynamic diameters with respect to the corresponding bare nanogel system was observed.

Table 6.1. DOTA-BBN-NG systems and their parent substrates: weight average molecular weight from SLS, hydrodynamic diameters (D_H) by DLS, concentration of NG in the system after purification, measured concentration of DOTA-BBN in the system after purification by UV-vis florescence spectroscopy, estimated number of DOTA-BBN molecules per nanogel.

Sample	M_W (MDa)	D_H (nm)	Conc. Pol (mg/mL)	BBN-DOTA/NG (μmol/g)	BBN-DOTA/NG (mol/mol)
NG(α)	4.5	65±20	5	/	/
NG(α)-BBN-DOTA/PBS	4.5	69±21	2.85	1.5	7
NG(β)	6.2	76±24	5	/	/
NG(β)*-BBN-DOTA/PBS	6.2	78±21	2.6	5.7	35
NG(β)*-BBN-DOTA/water	6.2	=	1.6	=	=

NG(α) and NG(β) belongs to different irradiation batches; * NG dialysis step before conjugation.

Even though for these conjugations experiments were used NG from two different irradiation syntheses, in both cases the hydrodynamic diameters of NG-BBN-DOTA systems did not change in comparison with their parent NG

The influence of the nature of the suspending medium either water or isotonic PBS, on the hydrodynamic dimension and on the hydrodynamic volume distributions was investigated by DLS and GFC measurements. No modifications in terms of hydrodynamic dimensions were detected (see Tab 6.1), result also confirmed by GFC measurements (Fig 6.1). The conjugated system dialyzed against isotonic PBS is characterized by marked peaks at higher times of elution. These peaks are certainly related to the presence of ions from the salts present in isotonic PBS.

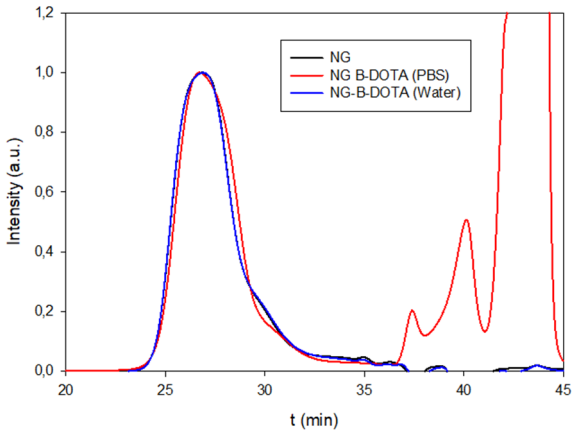

Fig 6.1 Chromatographic profiles related to NG(β) and NG(β)-BBN-DOTA dialyzed against water and against isotonic PBS.

6.3.2 Colloidal stability studies on NG-BBN-DOTA systems

The storage stability of the NG(β)-BBN-DOTA system stored at 4°C as dispersion in isotonic PBS was tested up to 6 months through DLS measurements and, no appreciably change in hydrodynamic diameter occurred.

Since the radiolabelling process required a temperature of 80° C for a duration of 50 minutes, both "bare" and BBN-DOTA conjugated systems were measured by DLS measurements in order to evaluate possible temperature-triggered aggregation phenomena. In Tab 6.2 the hydrodynamic diameters and width of size distribution for NG and NG-BBN-DOTA before and after the thermal treatment are shown.

Table 6.2 Hydrodynamic diameter (D_H) and width of size distribution for NG(β) and NG(β)-BBN-DOTA before and after the thermal treatment (t=50 min at 80° C).

System	**D_H (nm)**	
	t=0	t=50 min @ 80° C
NG(β)	76±24	79±25
NG(β)-BBN-DOTA/PBS	78±21	81±20

Selected NG-BBN-DOTA conjugated systems were radiolabeled with two radioisotops: ^{177}Lu and ^{90}Y.

The radiolabeled NG-BBN-DOTA systems were biologically tested *in vitro* and *in vivo*. In particular, binding and internalization studies were performed on rat pancreatic AR42J cells. *In vivo* biodistribution studies and tumor uptake studies were performed on an immunodeficient mice model. The preliminary biological evaluations are promising. In fact, higher total binding and comparable internalization percentage were obtained for NG-BBN-DOTA(^{177}Lu) systems compared to BBN-DOTA(^{177}Lu) and the tumour uptake of NG-BBN-DOTA(^{90}Y) was relatively high. In fact, after one hour from the administration, it was ten times higher than the free BBN-DOTA(^{90}Y). [11]

6.4 Conclusions

The main objective of this work was to synthesize NG-Bombesin-DOTA conjugated system for targeted radiopharmaceutical delivery to tumours with diagnostic and therapeutic purposes. The Bombesin-DOTA conjugated systems display relatively narrow hydrodynamic size of ca. 90 nm and they are stable upon storage as a colloidal dispersion and under conditions used for radiolabelling (T= 80 °C, 50 min). *In vitro* and *in vivo* biological evaluations on Bombesin-DOTA conjugated system are promising and strongly support further evaluations of NG-Bombesin-DOTA conjugated system for the envisaged application.

Acknowledgments

I wish to thank IAEA Coordinate Research project (F22064): "Nanosized delivery systems for radiopharmaceuticals" for Bombesin-DOTA supply and the National Centre for Nuclear Research, Radioisotope Centre POLATOM, Otwock, Poland for radiolabelling and biological evaluations.

References

[1] American Cancer Society. Cancer Facts & Figures 2018. Atlanta: American Cancer Society; 2018.

[2] D. Sarko, M. Eisenhut, U. Haberkorn1, W. Mier, Bifunctional Chelators in the Design and Application of Radiopharmaceuticals for Oncological Diseases. Current Medicinal Chemistry, 2012, 19, 2667-2688.

[3] A. Accardo, D. Tesauro, G. Morelli, Peptide-based targeting strategies for simultaneous imaging and therapy with nanovectors. Polymer Journal, 2013, 45, 481–493.

[4] M. Fani, H. R. Maecke, S. M. Okarvi, Radiolabeled Peptides: Valuable Tools for the Detection and Treatment of Cancer. Theranostics, 2012, 2(5).

[5] S.M. Okarvi, Peptide-based radiopharmaceuticals: future tools for diagnostic imaging of cancers and other diseases. Med Res Rev., 2004, 24, 357-97.

[6] J.C. Reubi, Peptide receptors as molecular targets for cancer diagnosis and therapy. Endocr Rev. 2003, 24, 389-427.

[7] M. Langer, A. G. Beck-Sickinger, Peptides as carrier for tumor diagnosis and treatment. Curr Med Chem Anticancer Agents. 2001, 1, 71-93.

[8] K. Greish, Enhanced permeability and retention (EPR) effect for anticancer nanomedicine drug targeting. Cancer Nanotechnology Methods in Molecular Biology. eds. Stephen R. Grobmyer, B. M. M.), Springer, Univ Florida, 2010). 624, 25–37

[9] A.Tornesello, L. Buonaguro, M. Tornesello, F. Buonaguro, New Insights in the Design of Bioactive Peptides and Chelating Agents for Imaging and Therapy in Oncology, Molecules 2017, 22, 1282.

[10] K. Park, S. Lee, E. Kang, K. Kim, K. Choi, I. C. Kwon, New generation of multifunctional nanoparticles for cancer imaging and therapy. Adv. Funct. Mater., 2009, 19, 1553–1566.

[11] M. Maurin, U. Karczmarczyk, E. Laszuk, P. Garnuszek, P. Ochniewicz, R. Mikolajczak , 3rd Research Coordination Meeting of the CRP on "Nanosized Delivery Systems of Radiopharmaceuticals, Vienna, Austria 2017,165-175.

Final remarks

PVP-based nanogels were synthesized starting from polymer aqueous solutions through high-energy radiation processing and modified with proper ligands to potentially address the specific diagnostic/therapeutic challenges of two pathologies: Alzheimer's disease and colorectal cancer.

The PhD project was aimed to elucidate some aspects of the process selected to produce the nanogels and to explore the versatility of this nanomaterial platform by performing several different conjugations using the same base nanogel.

It was confirmed that nanogel hydrodynamic size and size distribution is controlled by the reactions occurring when the material is absorbing the first few kiloGrays of irradiation dose. These reactions are mainly crosslinking and disproportionation for N_2O-saturated polymer solutions, and also chain scission for air-saturated systems. Irradiating the polymer solutions at higher doses does not affect the hydrodynamic size but does change the functional groups present in the network and produce some low molecular weight fragments (for N_2O-saturated systems), opening up the network.

For the first time, hydrogen peroxide was quantified in N_2O-saturated irradiated systems in a wide range of doses (0 – 80 kGy). Numerical simulations of the reactions occurring in irradiated water in the presence of a hydroxyl radical scavenger and for the specific conditions used in the experiments, provided comparable hydrogen peroxide concentrations to those experimentally measured. The numerical simulations also provided a quantitative estimation of molecular oxygen produced in N_2O-saturated systems. The presence of molecular oxygen at a stage when the network is already formed is expected to have an important role in the observed nanogel functionalization.

Furthermore, for the first time, double bonds were quantitatively measured. We can expect that these groups also react under irradiation. Nonetheless, for systems irradiated at low doses, the double bonds may be considered the fingerprints of

disproportionation reactions and thus, for their fixed ratio with crosslinking reactions for a given radical, may provide an indirect measurement of the extent of crosslinking.

A PVP-co-AA based nanogel system was selected for the development of biomedical delivery devices based on its physico-chemical properties (hydrodynamic size of 60-80 nm, slightly negative surface charge density, useful functional groups) and encouraging *in vitro* and *in vivo* biological responses (biocompatibility and clearance from bloodstream and urines within 24 h). This system was then covalently conjugated with ligands of different nature (a protein, a peptide, an oligonucleotide, several fluorescent probes) and characterised, as produced but also upon incubation in different media (e.g. saline buffer or serum) and storage in various conditions.

In general, the biological response of the various NG-conjugated systems was positive. In fact, tests *in vitro* demonstrated that (i) the nanogel was able to protect the biomolecule (insulin) from enzymatic degradation; (ii) the nanogel conjugates (with insulin, antimiR-31, and bombesin-DOTA) were able to interact with the target receptor or the complementary biomolecule; (iii) the NG coniugated to insulin (NG-In) was able to cross the blood-brain-barrier, one of the most challenging biological barriers, and with higher efficiency with the respect to “free” insulin.

In vivo biological evaluations of NG-In and NG-Bombesin-DOTA conducted on mice models demonstrated that these systems, administered through the intranasal and intravenous routes, respectively, were able to reach their target (brain for NG-In and tumour for NG-Bombesin-DOTA).

These findings show that radiation engineered PVP-based nanogels are a versatile and promising material platform for the development of biomedical delivery nanodevices and encourage to progress further in the development of predictive models that can support their design and manufacture, and in their biological evaluation with relevant *in vivo* disease models that can support their therapeutic or diagnostic efficacy.

APPENDIX A

Methods and procedures used in Chapter 2,3,4,5,6.

A.1 Dynamic Light Scattering (DLS)

The hydrodynamic dimension evaluations were performed by dynamic light scattering (DLS) measurements. In particular, a Brookhaven Instruments BI200-SM goniometer equipped with a 50 mW He-Ne laser tuned at λ= 632.8 nm and a Brookhaven BI-9000 correlator and a 100 mW solid-state laser (Quantum- Ventus MPC6000) tuned at λ=532 nm, were used. Before the measurement, all the samples were diluted to a concentration of 0.05 wt% to avoid multiple scattering and filtrated with 0.45 μm syringe filters to remove impurities. Measurements were carried out placing samples in a quartz cell within the thermostated cell compartment of the instrument at 25±0.1 °C and at 90° scattering angle. In consideration of their monomodal size distribution, DLS data were analyzed according to the method of cumulants [1] and represented in terms of average hydrodynamic diameter (D_H) and width of the size distribution. In fact, according to this method, it is possible to calculate the mean value and the standard deviation (index of the width of size distribution) from the polynomial expression in the delay time τ of the logarithm of the field-correlation function.

A.2 Static light Scattering (SLS)

Multiangle static light scattering measurements were performed in order to estimate the weight average molecular weight (Mw) of NG in aqueous solution. The measurements were performed at 25°C ± 0.1°C using a Brookhaven Instruments BI200-SM goniometer equipped with a 50 mW He-Ne laser tuned at λ= 632.8 nm. It has been measured a refractive index increments (*dn/dc*) of PVP k60 in aqueous solution equal to 0.185 mL/g using a Brookhaven Instruments differential refractometer at λ = 620 nm. The SLS data have been analyzed according to the Zimm plot method using the *dn/dc* value obtained for the linear PVP.

A.3 Gel Filtration Chromatografy (GFC)

Hydrodynamic volume distributions were determined by Gel Filtration Chromatography with a Shodex column thermostated at 20 °C with an Knauer oven, connected to a HPLC device (LC-2010 AT Prominence, Shimadzu, Kyoto, Japan) equipped with a 50 µl sample loop. All samples were eluted at 0.6 ml min^{-1} and the refractive index was recorded with Smartline RI detector 2300 Knaur. The measurements were performed at 0.05 wt% polymer concentration with addition of 0.02 wt% of sodium azide after 0.45 µm cut-off syringe filtration.

A.4 ζ-potential measurements

A Malvern Zetasizer Nano-ZS (Malvern instrument Ltd., Malvern, UK) equipped with a He–Ne laser at a power of 4.0 mW was used to estimate the net surface charge of NG based systems. ζ-potential measurements were acquired at 25 °C on systems previously dialyzed against Milli-Q water and diluted to a final concentration of 0.05 wt%. For systems characterized by a monomodal ζ-potential distribution, the mean ζ-potential and the relative distribution width are reported. Conversely, for systems that show a more heterogeneous surface charge density (i.e., multimodal ζ-potential distribution), mean ζ-potential values (Mean), relative widths (Std. Dev.) and relative abundance (Area %) of the different modes are reported.

A.5 Morphological analysis

The morphology evaluations of nanogel-based systems, previously dialysed in MilliQ water, was investigated by Scanning electron microscopy (SEM) and Transmission electron microscopy (TEM) techniques.

In particular, SEM measurements were performed by JEOL on NG-based dispersion

deposited on aluminum stubs, after being air-dried for 48 h and gold sputtered.
TEM measurements were performed by JEOL, JEM-2100 LaB_6 on as prepared of nanogel-based dispersion deposited in carbon-coated cupper grids after being air-dried for 48 h.

A.6 Functional groups characterisations

FTIR analysis

The chemical structure modification of the polymer was investigated by FTIR analysis and colorimetric titrations. FTIR analysis was carried out with Perkin Elmer-Spectrum 400 apparatus by dispersing the solids in potassium bromide and compressing them into pellets. Spectra were recorded at 30 scans per spectrum and 1 cm^{-1} resolution in the 4000-400 cm^{-1} range.

Colorimetric titrations

The concentration of carboxyl groups present was estimated by a colorimetric titration method based on the carboxyl groups ability to extract Ni^{2+} from water solutions [2]. In particular, known volumes of irradiated samples were mixed with Ni^{2+}/Hepes solution (concentration of Ni^{2+} in the final volume equals to 40μM) at pH of 7.5 and incubated for two minutes. This mixture was then centrifuged for 30 minutes at 3000 rpm, using a 100 KDa-cut off centrifuge filter. The eluted volumes were then twofold diluted with PV/Hepes solution (concentration of PV in the final volume equals to 40μM). Absorption spectra were recorded just after the PV addition, using a Jasco V 670 spectrophotometer. The PV/ Ni^{2+} complex is characterized by λ_{abs} = 650 nm, and the amount of sequestered Ni^{2+} by irradiated samples was calculated as the difference between the initial amount of Ni^{2+} and the complexed amount of Ni^{2+} bound to PVP irradiated sample. The non-irradiated PVP sample was used as control.

The quantification of primary amino groups produced in the irradiated systems was performed by colorimetric titration with fluorescamine. [3] In particular, when primary amino groups react with fluorescamine fluorescent adducts (λ_{exc}=391 nm, λ_{em}=481 nm) are formed. Equal volumes of fluorescamine/acetonitrile (1 mg/ml) solutions were added to given volumes of irradiated polymer samples and then twofold diluted with PBS (pH 7.4). Fluorescence spectra were recorded after 15 minutes of incubation at room temperature, using a (Jasco FP-6500 Spectrofluorometer). A calibration curve was built by reacting different concentrations of Boc-capped 1,5-pentanediamine (Cad-Boc) with fluorescamine.

A.7 (Bio)conjugation reactions procedure

(Bio)conjugation reactions between NG and the molecule of interest were carried out promoting the formation of an amide bond between the carboxyl group of NG and the primary amino group of the ligand. In particular, a two steps EDC/Sulfo-NHS protocol was adapted.[4] In the first step, EDC reacts with the carboxyl group of NG forming a highly reactive o-acylisoyrea intermediate. Since this intermediate may be quickly hydrolyzed by water, Sulfo-NHS is also used. In fact, when Sulfo-NHS ester reacts with the EDC-intermediate a more soluble and stable in water active intermediate is formed. Then, in the second step, the amine-carrying molecule is added and the reaction with the Sulfo-NHS ester intermediate occurs with the formation of the amide bond between NG and. (see Fig A.1).

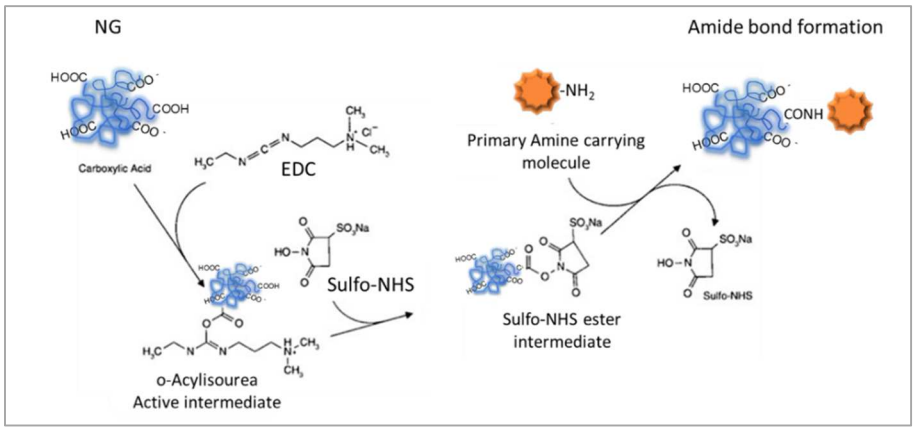

Figure A.1 (Bio)conjugation reaction scheme.

References

[1] D.E. Koppel, Analysis of macromolecular polydispersity in intensity correlation spectroscopy: the method of cumulants, J. Chem. Phys. 57 (1972) 4814-4820.

[2] A. Hennig, A. Hoffmann, H. Borcherding, T. Thiele, U. Schedler, U. Resch-Genger, Simple colorimetric method for quantification of surface carboxy groups on polymer particles, Anal. Chem. 83 (2011) 4970-4974.

[3] Y. Chen and Y. Zhang, Anal. Bioanal. Chem., 2011, 399, 2503–2509.

[4] G. T. Hermanson, Bioconjugate Techniques, 2nd , Elsevier, 2008.

APPENDIX B1

Experimental section of the biological evaluations related to Chapter 3

Cell cultures and treatments

LAN5 neuroblastoma cells were cultured with RPMI 1640 medium (Celbio srl, Milan, Italy) supplemented with 10% fetal bovine serum (FBS) (Gibco-Invitrogen, Milan, Italy), 2mM glutamine and 1% penicillin, 1% streptomycin (50 mg mL^{-1}). Both cellular cultures were maintained in a humidified 37°C incubator with 5% CO_2. LAN5 cells were treated with NG, at different concentrations (0.08, 0.16, 0.31, 0.45, 0.65, 1.25, 2.5 mg mL^{-1}) in serum free medium and, depending on the experiment, for 0.5, 1, 3, 6 or 24 hours.

The peripheral blood mononuclear cells (PBMCs) were isolated from 5 mL of venous blood collected early in the morning from healthy donors (age range: 20–30 years old). PBMCs were isolated from heparinized blood by Ficoll-Paque Plus (GE Healthcare Bio-Sciences AB) and cultured at a concentration of $1x10^5$ cells per well, in a 96-well flat-bottom plate, in complete RPMI 1640 medium supplemented with 10% FBS, 2 mM glutamine, and 100 U mL^{-1} penicillin/streptomycin at 37 °C. PBMCs were treated with NG alone at different concentrations (0.45, 0.65 mg mL^{-1}) or lipopolysaccharide (LPS) (0.1 µg mL^{-1}) and Aβ (40 µM) for 24 h. An enzyme-linked immunosorbent sandwich assay (ELISA) (Invitrogen) was performed for quantitative detection of interleukin 6 (IL-6) in cell culture supernatants. [1]

Determination of cell viability

Cell viability was measured by MTS assay (Promega). MTS [3-(4,5-dimethylthiazol-2-yl)-5-(3carboxymethoxyphenyl)-2-(4-sulphophenyl)-2H-tetrazolium] was utilized according to the manufacturer's instructions. LAN5 cells ($6x10^5$ cell mL^{-1}) or PBMCs ($1x10^6$ cell mL^{-1}) were plated in a 96-well plate. 20 µL of the MTS solution was added

to each well, and incubated for 4 h at 37°C, 5% CO_2. The absorbance was read at 490 nm on the Microplate reader WallacVictor (PerkinElmer). Results were expressed as the percentage of MTS reduction relative to the control. The treated cultured cells and the controls were morphologically analyzed by microscopy inspection on a Axio Scope 2 microscope (Zeiss). [1]

Hemolysis and coagulation assay

5 mL of blood from a human donor were drawn directly into K 2-EDTA-coated Vacutainer tubes to prevent coagulation. For the hemolysis assay the blood was centrifuged at 500 *g* for 5 min, and hematocrit and plasma levels were marked on the tube. The plasma was aspirated; the hematocrit tube was filled to marked line (original level of plasma) with 150 mM NaCl solution and gently inverted a few times to mix and then centrifuged at 500 *g* for 5 min. This step was then repeated to wash blood cells again. The supernatant was then aspirated and replaced with PBS at pH 7.4 and inverted to mix. 1 mL of erythrocytes was added into the corresponding tube at a 1:50 dilution ratio in PBS and 200 µL of erythrocytes were pipetted into a V-bottom 96-well plate. Thereafter we added to each well, NGs 0.65, 0.45 mg mL^{-1}, vehicle (distilled water), 10 µL of 20% Triton X-100 as positive control. The plate was incubated at 37°C for 1 hour. The samples were submitted to morphological analysis by microscopy inspection on a Axio Scope 2 microscope (Zeiss). The plate was centrifuged for 5 min at 500 *g* to pellet intact erythrocytes. Thereafter 100 µL of supernatant were transferred from each well into a clear, flat-bottomed 96-well plate. Absorbance of supernatants was then measured with a plate reader (wavelength 490 nm). After background subtraction, the average absorbance of the positive control was determined. Then all experimental data points were normalized with this mean absorbance value, which represents 100% hemolysis. To measure the *in vitro* plasma coagulation time and other coagulation factors, 2.5 mL of whole blood, from a human donor, was collected using citrated blood collection tubes (3.8% sodium citrate) and

the samples were exposed to NG (0.65 mg mL^{-1}) for 30 min at room temperature. After the incubation, the samples were centrifuged at 4000 rpm for 5 min. The plasma was collected and analyzed by prothrombin time (PT) assay, International Normalized Ratio (INR), activated partial thromboplastin time assay (aPTT) and by fibrinogen concentration using the ACL Instrumentation laboratory instrument. [1]

Animals

The experimental procedures employed in the present study were in accordance with the Italian D.L. no. 116 of 27 January 1992 and subsequent variations and the recommendations of the European Economic Community (86/609/ECC). The studies were approved by Ministero della Sanità (Rome, Italy). Male C57BL/6J (B6) mice, purchased from Harlan Laboratories (San Pietro al Natisone Udine, Italy) at 4 weeks of age, were housed under standard conditions of light (12h light: 12h darkness cycle) and temperature (22–24°C), with free access to food and water. They were habituated to handling for 14 days prior to the experiment (n=5 animals for group were used). [2]

Biodistribution and clearance in whole body of NG-Atto633

A 50 µl NG-Atto633 solution at a concentration of 2.87 µM Atto633 and 1.77 mg/ml NG was intraperitoneally administered. At different times (0, 4, 8 12 and 24 hours) the urine was taken. Deeply anesthetized mice were weighed and transcardially perfused with ice-cold phosphate-buffered saline (PBS). At 4 and 24 hours, the mice were quickly decapitated and organs and blood collected. The intraperitoneal space was inspected and no alteration was observed. The fluorescence intensity of Atto633 in the whole organs, blood and urine was analyzed by scanner fluorescence Typhoon FLA 9500 (GE Healthcare Life Sciences) at a resolution of 20 µm. The quantification of intensity was analyzed with the public-domain ImageJ software (US National Institutes of Health, Bethesda, MD), and 3D reconstruction of the fluorescence

intensity in the samples was performed by ImageMaster 2D Platinum 7.0 - GE Healthcare Life Sciences. Data are reported as the average channel fluorescence of the organs, given as relative units after background autofluorescence subtraction (not injected mouse organs). For intranasal administration, overnight-fasting mice from 4 and 24 h were anesthetized by intraperitoneal injection of tiletamine-zolazepam hydrochloride (50 mg/ml + 50 mg/ml; Zoletil®, Virbac s.r.l. Milano, Italy) 1 mg/Kg b.w. Then, the mice were placed in a head-back supine position and 10 µl of NG-Atto633, per nostril, was intranasally administered to mice using a micropipette (Pipetman P-10, Gilson). At different times (0, 10 and 30 minutes) the fluorescence intensity was monitored *in vivo* by Typhoon FLA 9500 (GE Healthcare Life Sciences). [2]

Histological analysis

For histochemical studies, the organs (liver, kidneys and nasal mucosa) were harvested, and fixed in 10% neutral buffered formalin (SIGMA). Then, they were embedded in paraffin, and 10 µm thick sections were cut and stained with hematoxylin and eosin (H&E). The histological sections were observed under an optical microscope with different combinations of magnification and objective lens. [2]

Blood analysis

After 24-hour treatment with NG-Atto633 the blood of C57BL/6J (B6) mice were taken by cardiac puncture and the *blood* was collected in *EDTA*-coated Eppendorf tubes. Cell count analysis was performed on a Beckman Z1 Coulter Particle Counter. Total WBC number, WBC composition, RBC number and parameters were collected. [2]

Fluorescence Dry Blood Spot

Presence of NG-Atto633 in blood and urine was measured by using the Dry Blood Spot **(BDS)** experimental procedure technique, and the fluorescent analysis was performed similarly to Lee et al. (2010) [56]. Blood was collected, by terminal heart puncture, after 4 and 24 hours of NG-Atto633 intraperitoneal injection. Blood drops (5 µl) were spotted on PVDF membrane placed on a non-absorbent surface and left to dry for 30 minutes at room temperature. Urines were collected at different times (4, 8, 12 and 24 hours) after NG-Atto633 intranasal injection, by using a micropipette. Urine drops (5 µl) were spotted on PVDF membrane and left to dry for 30 minutes at room temperature. In both cases fluorescence intensity was measured using Typhoon FLA 9500 (GE Healthcare Life Sciences) fluorescence scanner at a resolution of 20 µm. For both the samples the spots intensity was measured by building a NG-Atto633 standard curve. [2]

Immunohistochemistry and nuclear staining

Liver, kidneys and nasal sections were mounted on slides and deparaffinized in xylene solution. Then, the slides were hydrated in a series of graded ethanol (96%, 85%, 70%, 50%) for 5 minutes each. After washing in water and PBS the slides were incubated with 3% BSA/PBS for 1 hour. Next, the sections were incubated with anti-$CD4^+$ (1:40) (Dako) at 4 °C overnight. After washing in PBS, LSAB2 Dako kit (Dako, Glostrup, Denmark) and Fuchsin Substrate-Chromogen System Dako were used for the staining. The slides were mounted with cover slips and images were visualized by using a Leica DM5000 upright microscope (Leica Microsystems, Heidelberg, Germany) at 20X magnification. For nuclear staining, the sections were incubated with Hoechst 33258 (5 µg/ml) for 20 minutes and images were visualized by using a Leica DM5000 upright microscope (Leica Microsystems, Heidelberg, Germany) at 20X magnification, Ex 460 nm/Em 490 nm. [2]

Statistical analysis

Each value is expressed as mean ± SD. The significance of the differences in the mean values of multiple groups was evaluated using analysis of variance (ANOVA), followed by Bonferroni method for analysis of significance. Differences were considered significant when the *p-value* was ≤ 0.05.

References

[1] P. Picone, L.A. Ditta, M.A. Sabatino, V. Militello, P.L. San Biagio, M.L. Di Giacinto, L. Cristaldi, D. Nuzzo, C. Dispenza, D. Giacomazza, M. Di Carlo, Ionizing radiation-engineered nanogels as insulin nanocarriers for the development of a new strategy for the treatment of Alzheimer's disease, Biomaterials 80 (2016) 179–194.

[2] P. Picone, M.A. Sabatino, L.A. Ditta, A. Amato, P.L. San Biagio, F. Mulè, D. Giacomazza, C. Dispenza, M. Di Carlo, M., Nose-to-brain delivery of insulin enhanced by a nanogel carrier. J Control Release 270 (2017) 23-36.

APPENDIX B2

Experimental section of the biological evaluations related to Chapter 4

Cell cultures and treatments

LAN5 neuroblastoma cells were cultured with RPMI 1640 medium (Celbio srl, Milan, Italy) supplemented with 10% fetal bovine serum (FBS) (Gibco-Invitrogen, Milan, Italy), 2mM glutamine and 1% penicillin, 1% streptomycin (50 mg mL^{-1}). Immortalized mouse cerebral endothelial cells, bEnd3 cells (American Type Culture Collection, Manassas, VA) were grown in DMEM with 4.5 g L^{-1} glucose, 10% FBS (Gibco-Invitrogen, Milan, Italy), 3.7 g L^{-1} sodium bicarbonate, 4 mM glutamine, 1% penicillin and 1% streptomycin (50 mg mL^{-1}). Both cellular cultures were maintained in a humidified 37°C incubator with 5% CO_2. LAN5 cells were treated with NG, at different concentrations (0.08, 0.16, 0.31, 0.45, 0.65, 1.25, 2.5 mg mL^{-1}) or with NG-In, or with In, or with 40 μM of recombinant $A\beta_{42}$ (Aβ) [36, 37] alone or with NG, In and NG-In, in serum free medium and, depending on the experiment, for 0.5, 1, 3, 6 or 24 hours. In the NG-In and In samples the insulin concentration was always 0.05μM. Permeability assay were assessed using bEnd3 cells. The cells were seeded at a density of 25,000 cells per well in transwell permeable inserts (12 mm diameter, 0.4μm pore size; Corning Inc., NY). The experiments were performed on the monolayer, 9 days after cell seeding, allowing sufficient time for the cells junctions to develop. Inserts were incubated at different times (for 0.5, 1, 1.5 and 2 hours) with In^{FITC}, NG-In^{FITC}, NG^{TRITC} , sodium fluorescein (NaFluo) (1 μM). In the NG-In^{FITC} and In^{FITC} samples the insulin concentration was always 0.75 μM. The peripheral blood mononuclear cells (PBMCs) were isolated from 5 mL of venous blood collected early in the morning from healthy donors (age range: 20–30 years old). PBMCs were isolated from heparinized blood by Ficoll-Paque Plus (GE Healthcare Bio-Sciences AB) and cultured at a concentration of $1x10^5$ cells per well, in a 96-well flat-bottom plate, in complete RPMI 1640 medium supplemented with 10% FBS, 2 mM

glutamine, and 100 U mL^{-1} penicillin/streptomycin at 37 °C. PBMCs were treated with NG alone at different concentrations (0.45, 0.65 mg mL^{-1}) or lipopolysaccharide (LPS) (0.1 μg mL^{-1}) and Aβ (40 μM) for 24 h. An enzyme-linked immunosorbent sandwich assay (ELISA) (Invitrogen) was performed for quantitative detection of interleukin 6 (IL-6) in cell culture supernatants. [1]

Animals

The experimental procedures employed in the present study were in accordance with the Italian D.L. no. 116 of 27 January 1992 and subsequent variations and the recommendations of the European Economic Community (86/609/ECC). The studies were approved by Ministero della Sanità (Rome, Italy). Male C57BL/6J (B6) mice, purchased from Harlan Laboratories (San Pietro al Natisone Udine, Italy) at 4 weeks of age, were housed under standard conditions of light (12h light: 12h darkness cycle) and temperature (22–24°C), with free access to food and water. They were habituated to handling for 14 days prior to the experiment (n=5 animals for group were used). [2]

Resistance proteinase assay

NG-In^{FITC} and In^{FITC} were incubated with or without in PBS containing proteinase K (16 μg mL^{-1}). After 1 h of incubation, 500 μL of the samples were centrifuged with a centrifugal filter with a pore size of 3 kDa MWCO. In the solutions obtained after centrifugation, the FITC fluorescence, released following insulin degradation by proteinase K, was measured by fluorimeter (Microplate reader Wallac Victor2 1420 Multilabel Counter; PerkinElmer, Inc.) at the excitation/emission wavelengths of 350/450 nm, respectively. [1]

Assessment of NG-In binding to the LAN5 proteins

LAN5 proteins (20 μg) were either spotted on nitrocellulose membrane, and left to dry (dot-blot), or separated by 10% SDS PAGE and transferred onto nitrocellulose membrane. As a control, 20 μg of bovine serum albumin (BSA) were spotted on nitrocellulose membrane. The membranes were then incubated overnight in 3% BSA in PBS solution with and without NG-In^{FITC} and In^{FITC} (0.2 μM insulin concentration). After washing with PBS, the fluorescence present in the membranes was determined by Typhoon FLA 9500 (GE Healthcare Life Sciences), excitation 488 nm and emission 529 nm. [1]

Immunofluorescence analysis

LAN5 cells (180,000 cm^{-2}) were seeded in serum free medium, on Lab-Tek chambers and treated with NG-In^{FITC} for 3 hours. After treatment the cells were fixed in 4% paraformaldehyde in PBS for 30 min at room temperature. After three washes in PBS, the samples were incubated with PBS 0.2% Triton X-100 for 10 min and then with 3% BSA in PBS solution for 1 hour. The cells were then immunostained with anti-phospho-Insulin Receptor (p-IR) (1:500; Calbiochem Italia, Milan, Italy) antibody at 4°C overnight. After three washes in PBS, the samples were incubated with anti-rabbit TRITC-conjugate secondary antibody (1:300; Sigma Aldrich, Milan, Italy). For nuclear staining, the cells were incubated in Hoechst 33258 (5 mg mL^{-1}) for 20 min. Fluorescent images were observed with Axio Scope 2 microscope (Zeiss). [1]

bEnd3 cells (53,000 cm^{-2}) were cultured on Lab-Tek chambers for 9 days. After this time the cells were fixed in 4% paraformaldehyde in PBS for 30 min and kept at R.T.. After three washes in PBS they were incubated with 3% BSA in PBS solution for one hour. The cells were then incubated with anti Zonula Occludens-1 (ZO-1) (1:500; Santa Cruz) antibody at 4°C overnight. After three washes in PBS, the samples were incubated with anti-rabbit Cy3-conjugate secondary antibody (1:300; Sigma Aldrich,

Milan, Italy). For nuclear staining, the cells were incubated in Hoechst 33258 (5 mg mL^{-1}) for 20 min. 1024x1024 images were sequentially acquired in 2 channels on a Leica TCS SP5 inverted confocal scanning microscope with a 63x oil objective (Leica Microsystems, CMS, Mannheim, Germany) at a scanning frequency of 200 Hz. Hoechst fluorescence (pseudo scale blue) was measured under two-photo excitation at 780 nm (Spectra-Physics Mai-Tai Ti:Sa ultra-fast laser) emission range was 400-480 nm. Cy3 fluorescence (pseudoscale green) was excited at 543 nm using *supercontinuum white* laser (Leica Microsystems CMS, Mannheim, Germany). [1]

Total protein extraction and Western blotting on cell model

Total proteins were prepared by dissolving in solubilizing buffer (50 mM Tris–HCl pH 7.4, 150 mM NaCl, 0.5% Triton X-100, 2 mM phenylmethylsulfonyl fluoride PMSF), 1 mM DTT, 0.1% SDS, protease inhibitor (Amersham Biosciences, Milan, Italy) and phosphatase inhibitor (cocktail II and III; Sigma-Aldrich, Milan, Italy). Protein samples (30 μg) were submitted to 10% SDS–PAGE and transferred onto nitrocellulose filters. The Western blot was incubated with anti-phospho-Akt (S473) (1:1000; Cell Signaling, Boston, USA) and β-Actin (1:1000; SIGMA) antibodies. Primary antibody was detected using the Odyssey scanner (L-Licor) according to the manufacturer's instructions using secondary antibody labelled with IR 790, (1:10000; Life Technology). Band intensities were analyzed with ImageJ and expression was adjusted to β-Actin expression. The protein levels were expressed as intensity relative to control. [1]

Endothelial permeability assay

bEnd3 monolayer was formed on transwell insert with 0.4 μm pores as described above. Measuring the endothelial permeability of NaFluo, between 0 and 2 hours, assessed the quality of the monolayer and its capacity form junctions. The donor

chamber was filled with 0.3 mL of In^{FITC}, NG-In^{FITC}, NG^{TRITC} and NaFluo. The acceptor chamber was filled with 0.5 mL of medium. 0.2 mL were drawn every 30 min for 2 hours from the acceptor chamber, and replaced with an equal amount of medium. For saturation experiment bEnd3 cells were preincubated with an excess of free unlabeled insulin (75 μM) for 30 minutes. After washing in PBS, In^{FITC} or NG-In^{FITC} together with free unlabeled insulin (75 μM) were added in the donor chamber. The samples were drawn every 30 min for 120 minutes from the acceptor chamber. The fluorescence of the tracers in the samples was determined by Microplate reader WallacVictor 2 1420 Multilabel Counter (PerkinElmer, Inc.). The excitation and emission wavelengths were set to 485 and 530 nm, respectively, for FITC and NaFluo, 540 and 660 nm, for TRITC. For each sample the fluorescence intensity recorded after 30 min from the beginning of the experiment, is considered the reference value. Results are expressed as the ratio between fluorescence intensity measured at time *t* over the reference value. [1]

Total protein extraction, Western blotting and ELISA assay on mice brain.

The pellet of the brains or the different regions of brain obtained after homogenation (description above) were solubilized in RIPA buffer (20 mM Tris, pH 7.4, 150 mM NaCl, 1 mM Na_3VO_4, 10 mM NaF, 1 mM EDTA, 1 mM EGTA, 0.2 mM phenylmethylsulfonyl fluoride, 1% Triton, 0.1% SDS, and 0.5% deoxycholate) with protease (Amersham) and phosphatase inhibitor cocktails II and III (SIGMA). To remove insoluble material, cell lysates were sonicated and centrifuged at 11,500 ×g, for 10 min. Total proteins in the lysates was quantified by Bradford method (Bio-Rad). Proteins (20 μg) were resolved with NuPAGE 12% Bis-Tris gels (Life Technologies) and transferred onto nitrocellulose filters for immunoblotting with anti-p-Akt (1:500, Cell Signaling), GFAP (1:1000, Cell Signaling) and anti β-Actin (1:10000, SIGMA). Primary antibodies were detected by using the ECL chemiluminescence kit (Amersham) according to the manufacturer's instructions and secondary antibodies conjugated to horseradish peroxidase (1:2000) (Cell Signaling).

In some instances, antibodies were stripped from blots with Restore Western Blot Stripping Buffer (Thermo Scientific) for 15 min at room temperature, for antibody reprobing. Band intensities were analyzed with a gel documentation system (Bio-Rad). Expression was normalized with β-actin. The IL6, IL-1β, IL-10 and TGFβ concentrations in the total brain were determined using the enzyme-linked immunosorbent assays (IL6, IL-1β, IL-10 and TGFβ ELISA Cloud-Clone Corp, Wuhan, Hubei). [2]

Brain distribution after intranasal administration

For intranasal administration 20 µl (10 µl/nostril) of insulin in PBS solution (0.63 UI/ml) without or with FITC (In or In^{FITC}) or insulin-Nanogel without or with FITC (NG-In or NG-In^{FITC}) solution were injected into mice using a micropipette (Pipetman P-10, Gilson) after anesthesia. At 30 and 60 minutes the mice were quickly decapitated, and the whole brains were carefully isolated and washed with ice-cold PBS (pH 7.4). The brain samples were analyzed as a whole or separated into different regions (olfactory bulbs, hypothalamus, hippocampus, cerebral cortex, cerebellum) and these fragments were weighted. The equal weights of tissue samples were homogenized with 4 times the volume of ice-cold PBS (pH 7.4) with protease (Amersham) and phosphatase inhibitors (SIGMA) by using a dounce glass [36]. The brain homogenate was centrifuged at 4 °C and 5,400 ×g for 15 min. Total protein was quantified by Bradford method (Bio-Rad), and a volume corresponding to the same µg of total proteins of the resulting supernatant were used to determine the concentration of In or In^{FITC}. The insulin concentrations in the homogenate supernatants were determined by using an enzyme-linked immunosorbent assay (ELISA) based human insulin assay kit (Mercodia AB, Uppsala, Sweden). The In^{FITC} fluorescence intensity was measured by ImageMaster 2D Platinum 7.0 - GE Healthcare Life Sciences or by measuring the fluorescence intensity on a Typhoon Instrument. [2]

Statistical analysis

The experiments were repeated at least three times. Each experiment was performed in triplicate. The results are presented as mean ± SD. Statistical evaluation was conducted by ANOVA, followed by Student's t-test for analysis of significance. Results with a p-value <0.05 were considered statistically significant.

References

[1] P. Picone, L.A. Ditta, M.A. Sabatino, V. Militello, P.L. San Biagio, M.L. Di Giacinto, L. Cristaldi, D. Nuzzo, C. Dispenza, D. Giacomazza, M. Di Carlo, Ionizing radiation-engineered nanogels as insulin nanocarriers for the development of a new strategy for the treatment of Alzheimer's disease, Biomaterials 80 (2016) 179–194.

[2] P. Picone, M.A. Sabatino, L.A. Ditta, A. Amato, P.L. San Biagio, F. Mulè, D. Giacomazza, C. Dispenza, M. Di Carlo, M., Nose-to-brain delivery of insulin enhanced by a nanogel carrier. J Control Release 270 (2017) 23-36.

APPENDIX B3

Experimental section of the biological evaluations related to Chapter 5

Cell culture and reagents. SW480 and SW620 cells were routinely maintained in RPMI supplemented with 10% heat-inactivated fetal bovine serum, penicillin and streptomycin (50 IU/ml), 2 mM glutamine (Euroclone, UK). Cells were maintainned in a humidified atmosphere of 5 % of CO_2 at 37 °C.

hMSC viability (WST-1 test). WST-l colorimetric reagent (Roche Diagnostics GmbH, Manheim, Germany) was used to evaluate cell viability. Briefly, WST-1 reagent (10% vol/vol) was added to the cell monolayers, untreated and treated with 1nM, 10nM and 30nM of NG- control, NG-AntimiR-31-IC or NG-AntimiR-31-HC. After 4 hours of incubation, the formazan dye produced by viable cells was quantified spectrophotometrically at 450 nm by Bio-Rad Microplate Reader (Bio-Rad Laboratories, Hercules, CA, USA): results are reported as percentage of viable cells compared to control group.

miR-31 silencing. For miR-31 silencing, cells were transfected with Attractene Transfection Reagent (cat. number: 1051531, Qiagen) used following manufactory's indication. Briefly, SW480 and SW620 cells were seeded at 10,000 cells/cm^2 and transfected with 15pmoles/ml of miR-31 inhibitor (Biolegio BV) or scrambled negative control (cat. number: 4464058, Life Technologies), 24 hours after transfection the medium was collected and the cells processed for following assays.

RNA extraction and Real-time PCR. Total RNA was extracted using the commercially available illustraRNAspin Mini Isolation Kit (GE Healthcare, Italy), according to manufacturer's instructions. RNA was reverse-transcribed

to cDNA using the High Capacity cDNA Reverse Transcription Kit (Applied Biosystem, USA). Real-time PCR was performed in duplicates for each data point, and the oligonucleotides used are described in Table 1. Changes in the target mRNA content relative to housekeeping were determined with the ΔΔct Method.

Changes in the target mRNA content relative to housekeeping gene (β-actin) were determined with the ΔΔct Method. For miRNA expression, 250 ng of RNA was reverse transcripted according to manufacturer's instructions (cat. number: 4366596, TaqManMicroRNA Reverse Transcription, Applied Biosystem). TaqMan probes were used to analyse: miR-31 5p (cat. number: 4427975, Applied Biosystem) and U6 (cat. number: 4427975 Applied Biosystem). Changes in the target miRNA content relative to housekeeping U6 were determined with the ΔΔct Method.

Table 1. Gene primers used to study gene expression profiling

Gene	Primer forward	Primer reverse
E2F	CGCCATCCAGGAAAAGGTGT	ACATCGATCGGGCCTTGTTT
RHO A	GAAAACCGGTGAATCTGCGC	AGAACACATCTGTTTGCGGA
B-ACTIN	ATCAAGATCATTGCTCCTCCTGA	CTGCTTGCTGATCCACATCTG

Confocal analysis. Immunocytochemistry was done on PFA 4% fixed cells and stained with Alexa Fluor® 488 Phalloidin (A12379, ThermoFisher Scientific). The nuclei were stained with NucRed® Live 647 (cat. number: R37106, Life Technologies) and preparations were analysed by confocal microscopy (Nikon A1).

Statistics Analysis. *In vitro* experiments were repeated three times, giving reproducible results. Data are presented as mean values ± standard deviation (SD) of three independent experiments. For statistical analysis t-test or one- or two-way analysis of variance (ANOVA), followed by Dunnett's or Bonferroni's multiple comparison test, were performed using Prism 4 (GraphPadSoftwareInc., CA, USA).

Acknowledgment

This part was reproduced from Ref. "Dispenza, C.; Sabatino, M.A; Ajovalasit, A.; Ditta, L.A.; Ragusa, M.; Purrello, M.; Costa, V.; Conigliaro, A.; Alessandro, R.; Nanogel-AntimiR-31 conjugates affects colon cancer cells behaviour. RSC Adv., 2017, 7, 52039" with permission from the Royal Society of Chemistry.